Applications of Sterically Protected Hydrogen Bond Donors in the Secondary Coordination Sphere

by

Eric Wesley Dahl

A dissertation submitted in partial fulfillment
of the requirements for the degree of
Doctor of Philosophy
(Chemistry)
in the University of Michigan
2018

Doctoral Committee:

Associate Professor Nathaniel K. Szymczak, Chair
Professor Emeritus David P. Ballou
Professor Bart M. Bartlett
Professor Nicolai Lehnert

Eric W. Dahl

ewdahl@umich.edu

ORCID iD: 0000-0002-2407-2100

Dedication

To my family and friends

Acknowledgements

First, I'd like to thank my advisor Nate Szymczak for giving me the opportunity to work in his lab and transforming me into a competent scientist. He challenged me to be a better researcher, teacher, mentor, writer, and thinker, and provided me the skills to succeed at them all. He also encouraged me to pursue my own scientific interests and prepared me for the future as an independent scientist. I could not have asked for a better advisor for my PhD.

I'd like to thank my committee members Bart Bartlett, Nicolai Lehnert and Dave Ballou for their assistance and encouragement. Nicolai was gracious to allow me to rotate in his lab and provide me with the opportunity to be successful early in my graduate career. He let me make mistakes and I learned a lot in those three months as a result. Bart has allowed me to use equipment from his lab on multiple occasions and provided guidance in electrochemical experiments. Dave has been a great cognate member on my committee. His insight and perspective on my chemistry helped craft this thesis. Finally, you will all never know how much I appreciate how easy it was to schedule meetings with you.

I'd like to thank Dr. Cameron Moore for being my mentor and friend. Early in my graduate career he would patiently spend hours teaching me techniques in lab. His work is also the foundation for the chemistry presented in this thesis and I am so grateful for his guidance. I'd also like to thank all the other members of my lab for being generally awesome people to hang out with every day for five years. In particular, Jacob Geri was always willing to talk endlessly about chemistry and helped guide many of my research directions.

I'd like to thank my undergraduate advisor Linda Doerrer for first inspiring me to pursue graduate school and being hard on me when I needed it. I also want to thank our crystallographer Jeff Kampf for all his assistance over five years including helping me learn crystallography. I'd also like to thank the University of Michigan chemistry department and the Rackham graduate school for their support.

Finally, I need to thank my parents Pete and Fran and my sisters Allison and Melanie. Their unrelenting support over the last five years has helped me through the hardest times of graduate school. I am forever grateful.

Table of Contents

List of Figures

Abstract

Hydrogen bonding interactions found within the secondary coordination sphere of metalloenzyme active sites are involved in regulating substrate binding, stabilizing reactive intermediates and facilitating proton and electron transfer reactions. Synthetic systems that mimic these interactions can be used to gain further insight into metalloenzyme mechanism and expand their utility. In this thesis, metal-ligand complexes incorporating secondary sphere hydrogen bond donors were prepared to study their influence on metal structure and reactivity in systems derived from metalloenzymes. The pincer ligand 6,6"-bis(2,4,6-trimethylphenylamino)terpyridine (H_2Tpy^{NMes}) was prepared and incorporates sterically bulky H-bond donor groups in the secondary sphere. Inspired by [Fe]-hydrogenase, homogeneous ruthenium catalysts supported by H_2Tpy^{NMes} show enhanced reactivity for transfer hydrogenation reactions and enhanced stability for the dehydrogenative oxidation of primary alcohols compared to unsubstituted catalysts. The planar binding and secondary hydrogen bond donors in H_2Tpy^{NMes} were also used enforce an usual square planar geometry on copper(I). The geometric stabilization of complex $Cu(H_2Tpy^{NMes})Cl$ by hydrogen bonding to the chloride ligand allows for fast electron transfer self-exchange rates reminiscent of blue copper proteins. In separate studies, a series of copper and zinc complexes bearing 6-substituted tris(2-pyridylmethyl)amine (L^R) ligands appended with NH(*p*-R-C_6H_4) groups (R=H, CF_3, OMe, NMe_2) were prepared. The L^R ligands are electronically tunable in addition to providing sterically protected H-bond donors in the secondary sphere. Hydrogen bonding to the chloride ligand affords C_3-symmetric $Cu(L^R)Cl$ complexes that exhibit a reversible $Cu^{I/II}$ redox event based on electronic character ($\Delta E_{1/2}$ = 160

mV) and $Cu^{I}(L^{R})^{+}$ complexes react with oxygen to form hydrogen bonded (*trans*-1,2-peroxo)dicopper complexes. The additional stabilization provided by the H-bond donors allows for the stabilization of the first (*trans*-1,2-peroxo)dizinc complexes. Collectively, these studies demonstrate the role of secondary sphere hydrogen bonding interactions in the manipulation of metal complex structure, stability, and reactivity.

Chapter 1: Introduction

Portions of this chapter have been published:

Moore, C. M.; Dahl, E. W.; Szymczak, N. K.; Beyond H_2: exploiting 2-hydroxypyridine as a design element from [Fe]-hydrogenase for energy-relevant catalysis. *Current Opinion in Chemical Biology* **2015**, *25*, 9-17.

1.1 Secondary sphere interactions in metalloenzymes

In metalloenzymes, the primary coordination sphere consists of amino acid residues like histidine and cysteine that directly bind the active site metal. The coordination number and geometry of the metal center is controlled by the primary sphere residues. In contrast, the secondary coordination sphere consists of the amino acid residues that do not directly coordinate the metal but often play a critical role in regulating the metal's reactivity. Non-covalent interactions like hydrogen bonding (H-bonding) in the secondary sphere are responsible for orienting substrates for selective activation, regulating the metal's redox potential, stabilizing reactive intermediates along the reaction pathway, and facilitating proton transfer reactions.[1] These functions can be seen in copper nitrite reductase where an aspartate residue in the secondary sphere is responsible for proton transfer to the Cu-bound nitrite (Figure 1-1, left).[2] Additionally, in blue copper proteins like plastocyanin, two secondary sphere H-bonds to the Cu-bound cysteine residue help regulate the redox potential of the enzyme (Figure 1-1, right).[3] Virtually every metalloenzyme requires secondary sphere interactions for activity.

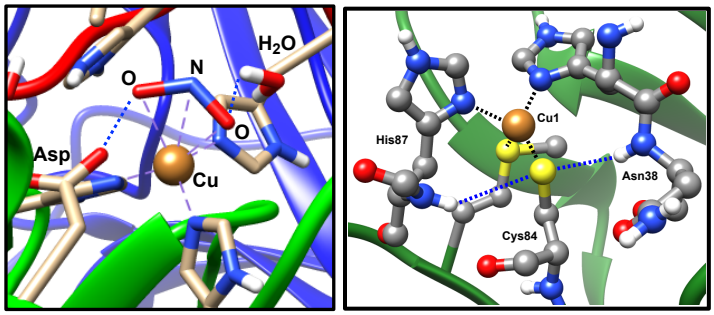

Figure 1-1: Crystal structures of copper nitrite reductase (left) and plastocyanin (right) showing critical secondary sphere H-bonding.

The study of secondary sphere interactions within synthetic metal complexes provides a means to further understand metalloenzyme mechanism.[4] Synthetic systems allow for precise control over a metals primary sphere through choice of ligand denticity and donors atoms as well as its secondary sphere through selected appended groups. The impact of secondary sphere interactions on primary sphere structure and reactivity can be determined more easily than in biological systems. This approach is the synthetic counterpart to mutagenesis studies, which probe the role of specific residues within a metalloenzyme. A fundamental understanding of how secondary interactions affect substrate binding and metal reactivity is desired for biological and homogenous catalysis applications.

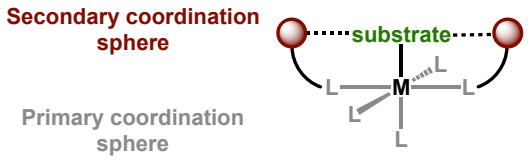

Figure 1-2: Design of ligands with secondary coordination sphere interactions for substrate binding and activation.

In biological and synthetic systems, primary sphere reactivity can be entirely dependent on the presence of secondary sphere interactions. To mimic the secondary sphere H-bond donor residues found in peroxidases and cyctochrome P450 monoxygenase, Nocera showed that the positioning of a carboxylic acid in the secondary sphere of a synthetic metalloporphyrin facilitated proton-coupled electron transfer pathways for the catalytic homolysis of peroxides (Figure 1-3, left).[5] In another example, Mareque-Rivas prepared a dizinc complex with multiple secondary sphere H-bond donor amines to successfully mimic the reactivity of phosphodiesterase, the enzyme responsible for RNA cleavage (Figure 1-3, right).[6] Cytochrome P450 monoxygenase and phosphodiesterase are only two examples of metalloenzymes that require secondary sphere H-bonding for activity. In the case of [Fe]-hydrogenase, the secondary H-bonding interaction is uniquely associated with the primary sphere reactivity providing a model framework for synthetic systems.

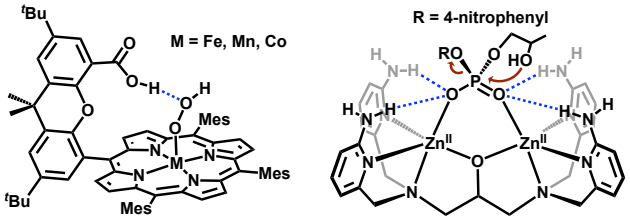

Figure 1-3: Structures of Nocera's hangman porphyrin (left) and Mareque-Rivas's model complex for phosphodiesterase (right).

1.2 [Fe]-hydrogenase and 2-hydroxypyridine

1.2.1 [Fe]-hydrogenase structure and mechanism

Unlike the other two hydrogenases ([FeFe] and [NiFe]), which catalyze the interconversion of H^+/e^- and H_2, [Fe]-hydrogenase catalyzes the reversible heterolytic cleavage

of H_2 into H^+/H^- with methenyltetrahydromethanopterin (MPT^+) acting as a H^- acceptor to form methylenetetrahydromethanopterin (HMPT, Figure 1-4).[7] The catalytically-active iron center in [Fe]-hydrogenase is an unusual iron guanylyl-pyridinol cofactor (FeGP cofactor), which has been crystallographically characterized by Shima and co-workers from *Methanocaldococcus jannashii* and at a higher resolution later from a mutant protein.[8] Combined, these studies revealed a square-pyramidal iron center ligated by a cysteine, two carbon monoxide (CO) ligands and the guanylyl-pyridinol moiety coordinated as a bidentate ligand through an acyl linkage and the pyridinol nitrogen. The water coordination site, *trans* to the iron-acyl ligand (L in Figure 1-4), serves as the site of H_2 coordination during catalysis.

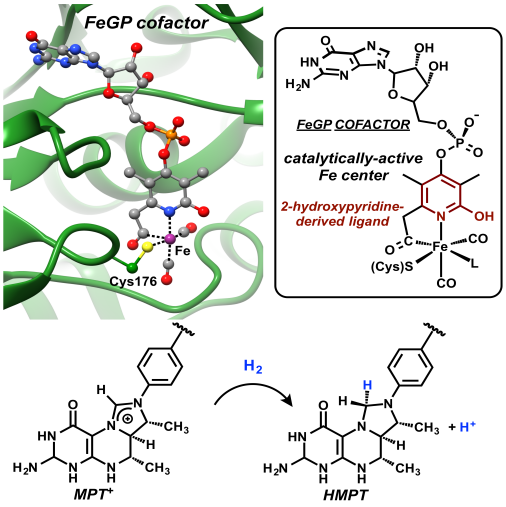

Figure 1-4: Crystal structure of the [Fe]-hydrogenase cofactor containing a 2-hydroxypyridine and hydride transfer to MPT^+.

Computational investigations into the mechanism of H_2 splitting and H^- delivery to MPT^+ have helped to further clarify the role of the pyridinol ligand at the active site. Yang and Hall described a resting state model of [Fe]-hydrogenase containing a strong Fe–H···H–O dihydrogen bond calculated by density functional theory (DFT) methods.[9] Two competing pathways for H_2

heterolysis were calculated: heterolysis involving H_2 deprotonation by (a) coordinated cysteine sulfur and (b) the pyridinoate oxygen. The barriers for H_2 heterolysis involving the pyridinoate oxygen and cysteine sulfur were both found to be minimal (3.3 and 6.6 kcal/mol, respectively) and calculations reported that H^- transfer to MPT^+ is rate limiting during catalysis. Yang and Hall further proposed that the role of the unique pyridinol ligand on iron is twofold: (1) to aid in H_2 heterolysis and (2) to stabilize the Fe–H through the formation of a dihydrogen bond.

1.2.2 H_2 activation and hydrogenation by 2-hydroxypyridine ligands

Germane to the aforementioned chemistry of [Fe]-hydrogenase, transition metal-catalyzed hydrogenation reactions are highly governed by the stability, and reactivity, of M-(H_2) and M-H intermediates. Given the strong H–H bond enthalpy of H_2 (104 kcal/mol), rapid formation of M-H species from H_2 is often a rate-limiting step for hydrogenation catalysis. The heterolysis of H_2 is a facile reaction at transition metal complexes supported by 2-hydroxypyridine ligands. Rauchfuss and co-workers demonstrated that the iridium complex Cp*Ir(κ^2-2-pyridinoate)Cl (**1**, Cp* = Me_5C_5) readily reacts with H_2 at -30 °C to form the iridium hydride species Cp*IrH(2-hydroxypyridine)Cl (**2**, Figure 1-5).[10] Complex **2** is transiently observable by NMR spectroscopy but is unstable with respect to dissociation of the 2-hydroxypyridine ligand.

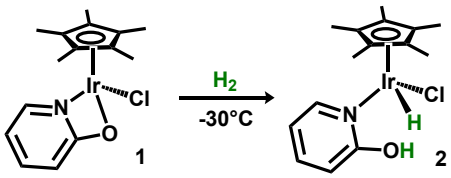

Figure 1-5: Heterolytic H_2 cleavage across iridium and 2-pyridone.

To impart greater stability to M-H species featuring 2-hydroxypyridine motifs, and subsequently broaden their application in catalysis, multidentate versions of this ligand have been designed and implemented. Specifically, iridium complexes supported by multidentate 2-hydroxypyridine ligands have been studied extensively for the hydrogenation of CO_2 in aqueous and non-aqueous media. The premier example of a 2-hydroxypyridine-derived system for CO_2 hydrogenation is the tetrahydroxybipyrimidine-iridium complex **3** studied by Hull, Himeda, Fujita and co-workers, which catalyzes the hydrogenation of CO_2 to formate (HCO_2^-) at ambient temperatures and low pressure of CO_2 under basic conditions.[11] The impressive reactivity of **3** was attributed to (1) the ability of the 2-pyridinoate complex **4** under basic conditions to lower the barrier to H_2 heterolysis and (2) the strong π-donating ability of the deprotonated ligand framework (Figure 1-6).

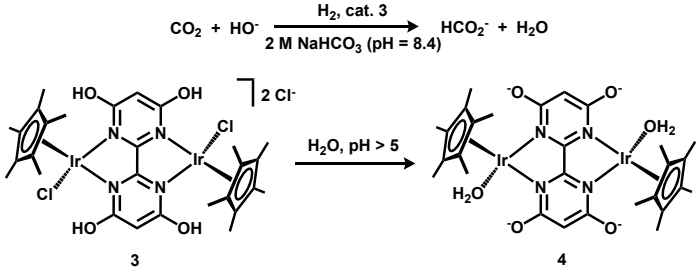

Figure 1-6: CO_2 hydrogenation to formate by an iridium catalyst bearing 2-hydroxypyridine-based ligands.

1.2.3 Dehyrogenation and H_2 storage by 2-hydroxypyridine ligands

The reversible nature of H_2 heterolysis and transfer by [Fe]-hydrogenase suggests that synthetic catalysts incorporating the 2-hydroxypyridine motif should likewise catalyze both reductive and oxidative transformations. Accordingly, Yamaguchi, Fujita and co-workers, as well as Rauchfuss and coworkers, have studied various Cp*Ir complexes bearing 2-

hydroxypyridine-derived ligands for the dehydrogenation of primary and secondary alcohols (Figure 1-7).[10, 12] Complex **5** containing monodentate 2-hydroxypyridine exhibits only modest activity for the dehydrogenation of secondary alcohols, and poor activity for primary alcohols. These low catalytic efficiencies, however, can be increased by utilizing complex **6** featuring a bidentate 2-hydroxypyridine ligand (albeit in the presence of added base under catalytic conditions). High catalytic efficiency was realized with the fully deprotonated complex **7**: TON's as high as 275,000 were observed for the oxidation of secondary alcohols and as high as 47,500 in the oxidation of primary alcohols (Figure 1-7).

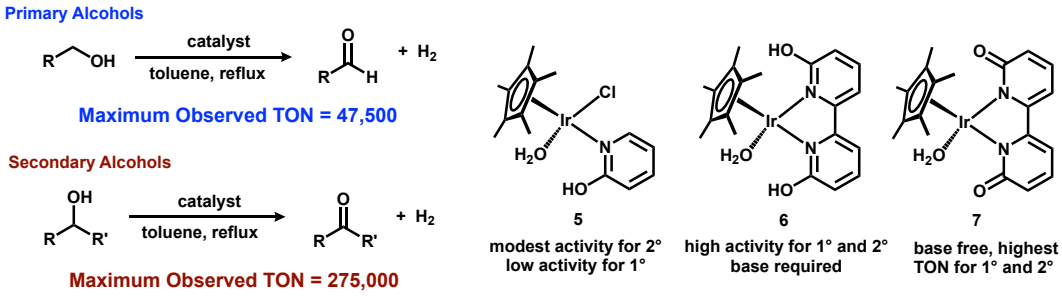

Figure 1-7: Primary (1°) and secondary (2°) alcohol dehydrogenation by iridium catalysts.

Hydrogen storage using N-heterocycles has grown in popularity due to their inherent capacity for storing multiple equivalents of H_2, thermodynamic feasibility, simplicity and safety.[13] Recently, Fujita, Yamaguchi and coworkers have shown reversible H_2 storage using complex **10** with N-heterocyclic compounds (Figure 1-8).[14] The complete hydrogenation/dehydrogenation of 2,6-dimethyl-1,5-naphthyridine (**8**) to **9** was performed in 92% yield under forcing conditions (130°C, 70 atm H_2 for hydrogenation) with five equivalents of H_2 stored in the N-heterocycle and a gravimetric density of 6.6 wt% H_2. 2-Hydroxypyridine-based catalysts have shown exceptional activity in current reversible H_2 storage systems due to

their unique ability to lower kinetic barriers for H_2 delivery during hydrogenation and H_2 release during dehydrogenation. As the development of new H_2 storage schemes continues to grow, the ease in which catalysts incorporating the 2-hydroxypyridine motif manipulate H_2 makes them obvious contenders for future work in the field.

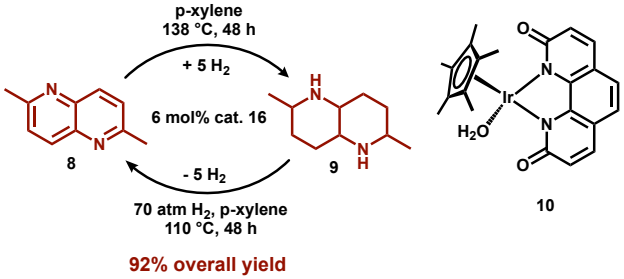

Figure 1-8: Reversible H_2 storage scheme using a single iridium 2-pyridone catalyst.

1.3 6,6"-dihydroxyterpyridine for (de)hydrogenation catalysis

The Szymczak lab developed the ligand 6,6"-dihydroxyterpyridine (dhtp) in order to adapt key design features from [Fe]-hydrogenase within a tridentate pincer framework more suited for homogeneous catalysis (Figure 1-9).[15] The terpyridine (tpy) scaffold, although redox non-innocent, was chosen for its oxidative stability and rigid meridonal binding to metals. Similar to the dihydroxybipyridine systems described above, dhtp is able to serve as both a neutral donor ligand with pendent H-bond donors *or* a doubly anionic ligand with H-bond acceptors upon deprotonation. However, unlike dihydroxybipyridine, dhtp places both pendent H-bonding groups within the same equatorial coordination site allowing cooperative activation of substrates by both pendent groups. Inspired by [Fe]-hydrogenase, ruthenium complexes bearing the dhtp and parent tpy ligands were used as catalysts for transfer hydrogen in order to

determine whether the addition of 2-hydroxypyridine groups played a beneficial role in hydrogenation catalysis.

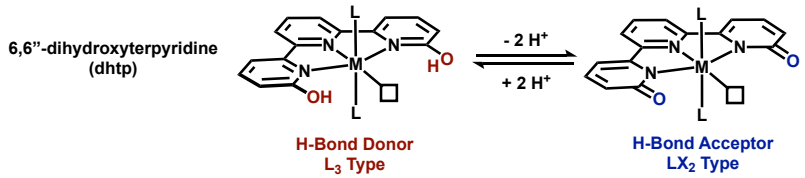

Figure 1-9: 6,6"-dihydroxyterpyrdine (dhtp) as a proton-responsive ligand.

1.3.1 Transfer hydrogenation reactivity

Initial studies by our lab reported the catalyst $[Ru(dhtp)(PPh_3)_2]PF_6$ for the regioselective transfer hydrogenation to ketones over olefins.[15] The analogous catalyst $[Ru(tpy)(PPh_3)_2]PF_6$ showed diminished reactivity toward transfer hydrogenation only producing 21 turnovers of 1-phenylethanol from acetophenone in 1 hr compared to 141 turnovers for $[Ru(dhtp)(PPh_3)_2]PF_6$.[16] While the two catalysts maintained similar primary sphere environments, the dhtp-based catalyst was able to use 2-hydroxypyridine groups for cooperative substrate activation. The role of the 2-hydroxypyridines was further supported by the synthesis of the 4-hydroxypyridine analogue to dhtp (4,4"-dihydroxyterpyridine). This ligand was electronically similar to dhtp in its proton-responsive behavior; however, the hydroxyl groups were positioned away from the remaining equatorial binding site on ruthenium. When compared to both parent tpy and 4,4"-dihydroxyterpyridine-based ruthenium-carbonyl catalysts, the dhtp-based catalyst showed the highest regioselectivity for ketone hydrogenation over olefins (Figure 1-10). These observations coupled with other mechanistic studies and a notable cation-dependent reaction rate suggested that the interaction of the pendent pyridone (formed from deprotonation during catalysis) with a

cation and ketone substrate likely formed a favorable transition state for hydride transfer. Although in this system the pendent pyridone groups were not directly activating ketone substrates, the ability to alter reaction rate and selectivity by purely secondary sphere substitutions provides a framework for future work in this area.

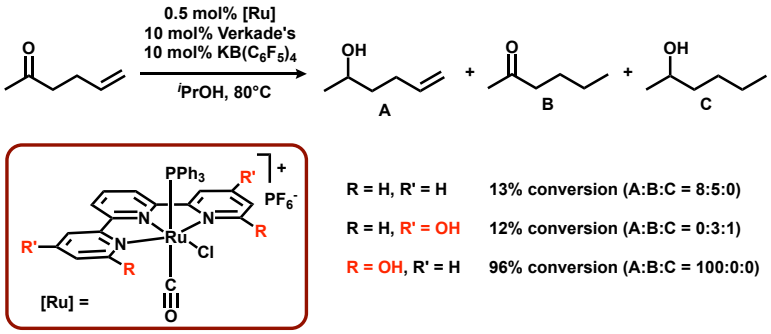

Figure 1-10: Regioselective transfer hydrogenation reactivity of a R-dhtp catalyst compared to 4-hydroxypyridine-based and terpyridine ligands.

1.3.2 Decomposition pathways

Although a promising ligand for (de)hydrogenation reactions, Ru-dhtp catalysts suffered from poor stability toward water. Even with rigorously dried isopropanol as a solvent our lab observed the formation of an aquo-bridged dimer during transfer hydrogenation reactions (Figure 1-11).[16] The pendent pyridonates contribute to the stability of this dimer through H-bonding interactions from the water molecule. The formation of multinuclear clusters with dhtp were also observed when first-row metals were employed. In addition to the obvious transition from Ru to Fe in order to make the system more biomimetic, other first row metals like Ni, Co and Cu were used to access new coordination chemistry and reactivity. Metallation strategies that produced mononuclear complexes of Fe, Ni, and Co without forming the homoleptic complex, $[M(dhtp)_2]X$ (M = Fe, Ni and Co; X = Cl and Br) were synthesized but were still extremely

sensitive to weak bases and water.[17] Upon the addition of even mild bases, the formation of μ-oxo or μ-hydroxo-bridged trimer complexes were observed for Fe, Ni and Co (Figure 1-12). Formation of the μ-oxo trimer was also observed in anhydrous solvents in a N_2-filled glovebox and when strong donor ligands like trimethylphosphine were employed. In addition to the affinity of water for the equatorial binding site, the oxophilicity of the first-row transition metals enhanced the stability of the trimer complexes by pendent pyridinoate binding to the adjacent metal center. The dhtp ligand draws key design features from [Fe]-hydrogenase to achieve enhanced hydrogenation reactivity; however, its inherent capacity to form undesired aggregates required the development of new ligands.

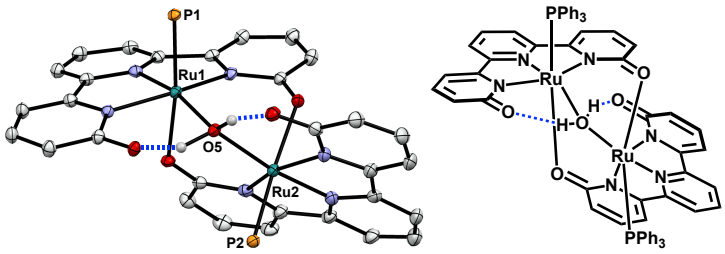

Figure 1-11: Crystal structure of the aquo-briged dimer $Ru_2(dhtp)_2(PPh_3)_2(OH_2)$ decomposition product. (30% ellipsoids, H atoms not involved in H-bonding, and phenyl groups on PPh_3 omitted for clarity).

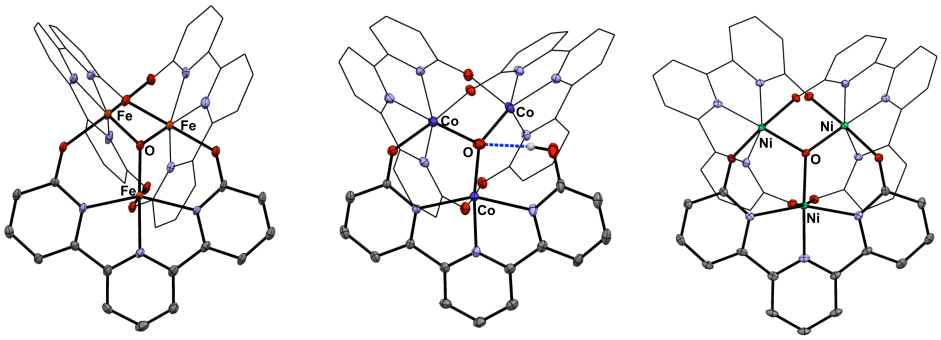

Figure 1-12: Crystal structures of Fe, Co, and Ni μ_3-oxo clusters of dhtp.

1.4 A tripodal ligand with 2-hydroxypyridine

The ligand tris(6-hydroxyl-2-pyridylmethyl)amine (H_3thpa) was developed as the C_3-symmetric tetradentate analogue of dhtp (Figure 1-13).[18] Based on the tris(2-pyridylmethyl)amine (tpa) ligand scaffold, H_3tpa replaces all three pyridine arms with 2-hydroxypyridines. It was hypothesized that a tripodal ligand may prevent multinuclear complexes by only providing a single open coordination site for substrate binding. Additionally, the tpa ligand has seen extensive use in the study of metalloenzyme active sites, specifically copper-containing metalloenzymes.[19] In biomimetic systems, pyridine is considered a synthetically robust and easily tunable substitute for histidine-containing active sites like those found in copper-containing oxygenase/oxidase and copper nitrite reductase.[19a] Tpa has, therefore, been used to model the *primary* sphere of those enzymes. However, secondary sphere H-bonding interactions play a critical role in the activity of many of these enzymes (*vida supra*). The H_3thpa ligand provided a suitable framework to probe the role of secondary H-bond donors in a biomimetic system.

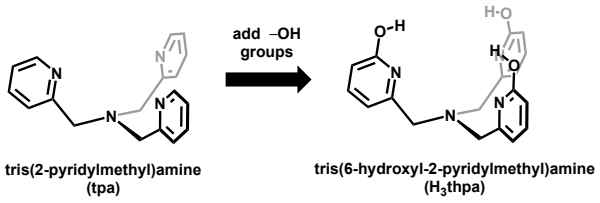

Figure 1-13: A 2-hydroxypyridine ligand based on the tetradentate ligand tris(2-pyridylmethyl)amine (tpa).

Early work by Szymczak and coworkers explored the coordination chemistry of copper(I) chloride and fluoride complexes with the H_3thpa ligand. In both cases the Cu(I) complexes were C_3-symmetric with three directed H-bonds to the respective halide and showed highly reversible

$Cu^{I/II}$ redox behavior.[18, 20] The Cu(H_3thpa)F complex (**11**) was particularly intriguing due to its unusual stability – a result of the strong –OH···F hydrogen bonds. Reagents containing the triphenylsilyl (Ph_3Si) group were used to abstract the fluoride from Cu(H_3thpa)F by formation of a strong Si-F bond, which allowed the substitution of the axial coordination site for more bio-relevant substrates. In particular, Ph_3Si-NO_2 was used to generate a Cu(I)-NO_2^- species that immediately decomposed to Cu^{II}(H_2thpa)OH (**12**) and nitric oxide gas via reduction and protonation of the Cu-bound nitrite (Figure 1-14).[21] DFT studies supported a mechanism where electron transfer from Cu(I) to the NO_2^- was concurrent with intramolecular proton transfer from a pendent –OH group leading to N–O bond scission. While not specifically designed to mimic the Cu-nitrite reductase active site, the Cu-H_3thpa system had mechanistic implications on the individual steps along the NO_2^- reduction pathway.

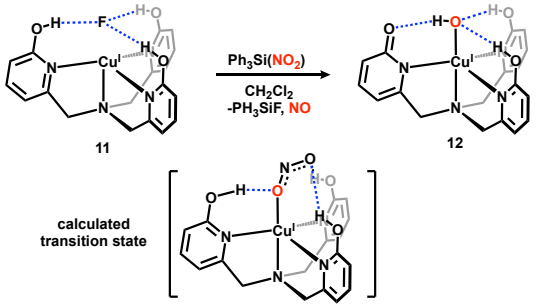

Figure 1-14: Reaction of **11** with $Ph_3Si(NO_2)$ to form **12** and the DFT calculated intermediate prior to proton-coupled electron transfer.

Although the H_3thpa ligand allowed for the study of bio-relevant first-row metal reactivity, it still suffered from the many issues associated with 2-hydroxypyridine-based ligands. The lability of the pyridine arms on H_3thpa led to facile formation of dinuclear Cu(I) and

Cu(II) complexes in the presence of weak bases (Figure 1-15).[22] These dimer complexes are further stabilized by H-bonds from the protonated 2-hydroxypyridine arms.

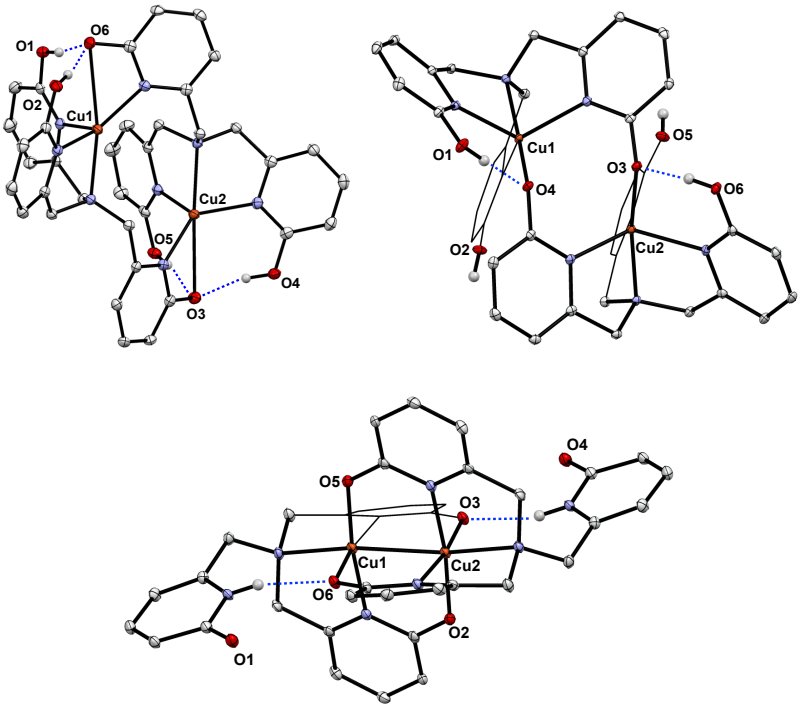

Figure 1-15: Crystal structures of the Cu(I) dimer $Cu_2(H_2thpa)_2$ (left) and Cu(II) dimer complexes (right and bottom) (30% ellipsoids, H atoms not involved in H-bonding omitted for clarity).

1.5 Limitations of 2-hydroxypyridine-based ligands

Overall, increasing denticity did not inhibit common deactivation pathways for 2-hydroxypyridine-based ligands. Based on the problems observed for the dhtp and H_3thpa ligands, three properties of this ligand family were identified for continued progress in this field:

1) The pKa of 2-hydroxypyridine is too low

While facile deprotonation was not an issue with heavier metals such as ruthenium, the oxophilicity of first-row metals leads to formation multinuclear clusters upon deprotonation.

2) The unfavorable tautomerization of 2-hydroxypyridine

Although we refer to these ligands as bearing '2-hydroxypyridines', the 2-pyridone tautomer is preferred, meaning metal binding to the pyridine must overcome the energy of tautomerization. Increased ligand lability due to this tautomerization could enhance formation of multinuclear complexes.

3) No steric protection for the H-bond donors

Perhaps the most important factor limiting the utility of 2-hydroxypyridine ligands is the lack of steric protection near the –OH donors. Additional steric bulk on dhtp and H_3thpa would likely have prevented formation of multinuclear complexes.

The classic strategies to address these problems include addition of electronic donating and withdrawing groups to the pyridine backbone and addition of sterically bulky groups, like *tert*-butyl, *ortho* to the –OH. Unfortunately, these modifications are exceedingly synthetically challenging (multi-step syntheses for a single ligand). Therefore, we sought to develop similar frameworks that resemble the 2-hydroxypyridine ligands but allow for easily tunable secondary H-bond donor groups.

1.6 Motivation for sterically protected H-bond donors

In Nature, the extended metalloenzyme structure is designed to protect the active site from deactivation. The primary amino acid residues hold the metal in the precise orientation while the secondary residues direct selective substrate binding. In contrast to [Fe]-hydrogenase

and other metalloenzymes containing first-row transition metals, synthetic complexes must address deactivation pathways through other means. The synthesis of sterically bulky ligands is perhaps the most common way to prevent unwanted multinuclear complexes.[23] When sterically protected secondary sphere H-bond donors are desired, secondary amine and amido groups have found the greatest utility. Specifically, the pivalamido and related groups have been appended to tripodal ligand frameworks for a variety of purposes. Borovik reported the stabilization of M-X (M= Fe and Mn; X = O, OH) complexes, some derived from O_2 using a tris(2-aminoethyl)amine (tren) ligand bearing three *tert*-butylureayl groups (Figure 1-16, left).[24] Masuda demonstrated the stabilization of a Cu-OOH species with H-bonds from a tpa ligand appended with two pivalamido groups (Figure 1-16, middle).[25] Berreau also used the tpa backbone with pivalamido and reduced neopentyl groups for the study of Zn-X (X = OH, OR) species (Figure 1-16, right).[26] The secondary sphere sterically protected H-bond donors, common among all these examples, was critical for stabilization of these complexes. Although early work discovered an easy electronic modification to the pivalamido group was simply reduction to the neopentyl group, examples of more modular secondary H-bond donors that allow precise tuning of the steric and electronic character are lacking in the literature.

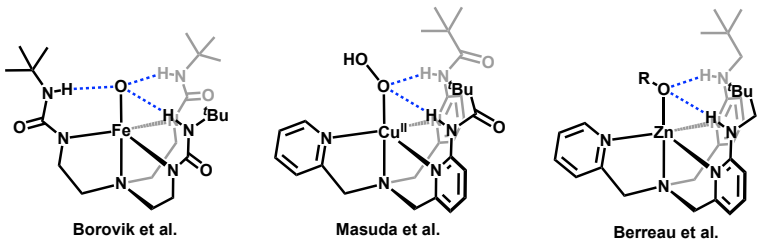

Figure 1-16: Representative structures of ligands appended with sterically bulky H-bond donors.

The phenylamino group is the ideal substitute for both 2-hydroxypyridine and pivalamido-based ligands. The phenyl group maintains a planar steric profile that can be expanded through *ortho*, *meta* and *para* substitutions and the widely available pKa values for substituted anilines allows for electronic tuning of the H-bond donor strength and ligand electronic character. Together these features provide highly tunable, sterically protected, H-bond donors. To the best of our knowledge there are only two examples of mononuclear metal complexes utilizing secondary sphere phenylamino groups for H-bonding. Fout recently demonstrated steric and electronic differences in Fe-OH complexes of the tris-(pyrrolylmethyl)amine ligand bearing phenylamino and 2,6-diisopropylphenylamino groups (Figure 1-17, left).[27] Chang and coworkers showed O_2 reduction at a pentadentate Fe complex with pendent 2-phenylaminopyridine ligands (Figure 1-17, right).[28] The lack of 2-phenylaminopyridine ligands in the literature is surprising given their ease of synthesis. A variety of 2-phenylaminopyridine ligands can be obtained in a single step via Buchwald-Hartwig coupling or SN_{Ar} reactions from cheap aniline derivatives and 2-bromopyridine-containing ligands. In addition, they are capable of addressing all the outlined issues of 2-hyrdoxypyridine-based ligands (Figure 1-18).

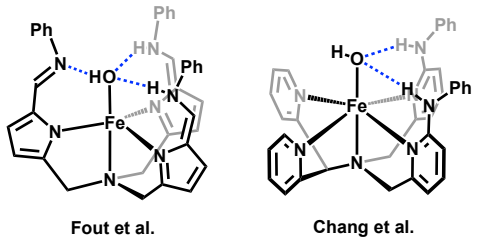

Figure 1-17: Representative structures of ligands appended with –NHPh groups for H-bonding.

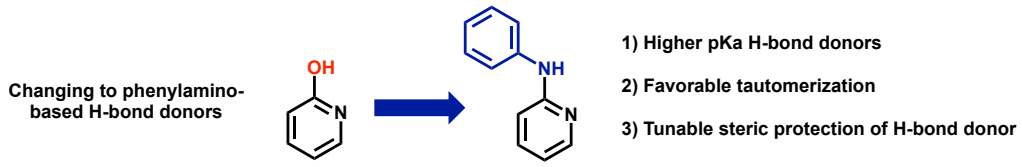

Figure 1-18: 2-Phenylaminopyridine groups address all the issues observed for 2-hydroxypyridine-based ligands.

Density functional theory (DFT) calculations also support 2-phenylaminopyridine as an ideal substitute for 2-hydroxypyridine. The structures of 2-phenylaminopyridine and 2-hydroxypyridine were optimized at the ωB97XD/6-31G level of theory within a CH_2Cl_2 polarizable continuum model to obtain the energies of tautomerization and pKa for each species. One noted problem with the 2-hydroxypyridine ligands was the tautomerization from 2-pyridone required for metal binding. The 2-pyridone form was found to be 5.9 kcal/mol more favored than 2-hydroxypyridine whereas 2-phenylaminopyridine is strongly favored by 11.0 kcal/mol over the imine form (Figure 1-19). This result means the 2-phenylaminopyridine ligands will remain as neutral pyridine donors preventing unwanted metal binding to the pendent phenylamine. The pKa of the 2-hydroxypyridine unit was also a major problem resulting in multinuclear clusters even under mildly basic conditions. The pKa of the 2-phenylaminopyridine unit was calculated to be 7 pKa units higher than 2-pyridone and 11 pKa units higher than 2-hydroxypyridine (the form upon metal binding) providing a stable H-bond donor under mildly acidic and mildly basic conditions. These DFT results further support that ligands bearing 2-phenylaminopyridine derivatives are ideal systems for studying a multitude of bio-relevant and first-row metal chemistry.

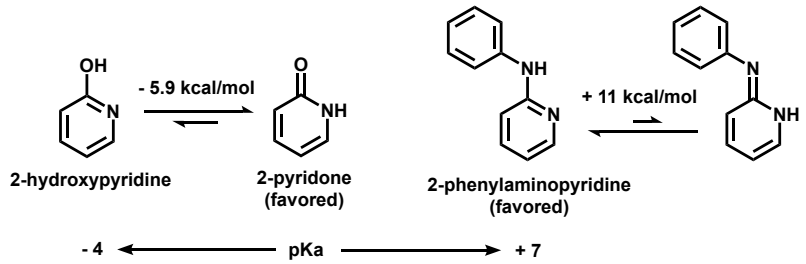

Figure 1-19: DFT calculated energies of tautomerization for 2-hydroxypyridine and 2-phenylaminopyridine and the relative pKa differences between structures.

1.7 Outline and scope of thesis

This thesis describes various applications of sterically protected secondary coordination sphere H-bonding in transition metal complexes. While many of the initial hypotheses were derived from the secondary sphere interactions found in metalloenzyme active sites, the synthetic ease and highly tunable nature of ligands bearing 2-phenylaminopyridine groups provided a framework for exploring applications beyond the natural systems. In chapter 2, the critical role of 2-hydroxypyridine in [Fe]-hydrogenase inspired the synthesis of a ruthenium pincer catalyst for hydrogenation and dehydrogenation reactions. Sterically bulky pendent phenylamino groups (2,4,6-trimethylphenylamino) are used to shut down decomposition pathways from adventitious water and enhance the recyclability of the catalyst in dehydrogenative oxidation reactions. In chapter 3, the network of H-bonds responsible for maintaining the coordination geometry of blue copper protein active sites inspires the stabilization of Cu(I) geometries in an unusual square planar geometry through secondary H-bonding. The ability to maintain geometry between the Cu(I) and Cu(II) states allows for electron transfer self-exchange on the order of blue copper proteins. In chapter 4, the Cu-O_2 intermediates involved in copper oxygenase and oxidase enzymes inspire the stabilization of a Cu-O_2 adduct by H-bonding. The oxygen to copper charge transfer band in the Cu-O_2 adduct is tuned by electronic substitutions on the 2-

phenylaminopyridine moiety and the utility of the secondary H-bonds is demonstrated by the synthesis of an unusual series of electronically distinct Zn-O_2 adducts stabilized by H-bonds. The failure of 2-hydroxypridine-based ligands to achieve the desired chemistry is also demonstrated in each chapter.

1.8 Notes and references

1. R. H. Holm, P. Kennepohl and E. I. Solomon, *Chem. Rev.*, 1996, 96, 2239-2314.
2. (a) A. C. Merkle and N. Lehnert, *Dalton Trans.*, 2012, 41, 3355-3368; (b) S. Suzuki, K. Kataoka and K. Yamaguchi, *Acc. Chem. Res.*, 2000, 33, 728-735.
3. M. C. Machczynski, H. B. Gray and J. H. Richards, *J. Inorg. Biochem.*, 2002, 88, 375-380.
4. (a) D. Natale and J. C. Mareque-Rivas, *Chem. Commun.*, 2008, 425-437; (b) M. Zhao, H.-B. Wang, L.-N. Ji and Z.-W. Mao, *Chem. Soc. Rev.*, 2013, 42, 8360-8375; (c) S. A. Cook, E. A. Hill and A. S. Borovik, *Biochemistry*, 2015, 54, 4167-4180.
5. (a) C. J. Chang, L. L. Chng and D. G. Nocera, *J. Am. Chem. Soc.*, 2003, 125, 1866-1876; (b) C.-Y. Yeh, C. J. Chang and D. G. Nocera, *J. Am. Chem. Soc.*, 2001, 123, 1513-1514.
6. G. Feng, D. Natale, R. Prabaharan, J. C. Mareque-Rivas and N. H. Williams, *Angew. Chem. Int. Ed.*, 2006, 45, 7056-7059.
7. W. Lubitz, H. Ogata, O. Rüdiger and E. Reijerse, *Chem. Rev.*, 2014, 114, 4081-4148.
8. (a) T. Hiromoto, K. Ataka, O. Pilak, S. Vogt, M. S. Stagni, W. Meyer-Klaucke, E. Warkentin, R. K. Thauer, S. Shima and U. Ermler, *FEBS Lett.*, 2009, 583, 585-590; (b) S. Shima, O. Pilak, S. Vogt, M. Schick, M. S. Stagni, W. Meyer-Klaucke, E. Warkentin, R. K. Thauer and U. Ermler, *Science*, 2008, 321, 572-575.

9. X. Yang and M. B. Hall, *J. Am. Chem. Soc.*, 2009, 131, 10901-10908.

10. A. M. Royer, T. B. Rauchfuss and D. L. Gray, *Organometallics*, 2010, 29, 6763-6768.

11. J. F. Hull, Y. Himeda, W.-H. Wang, B. Hashiguchi, R. Periana, D. J. Szalda, J. T. Muckerman and E. Fujita, *Nature Chemistry*, 2012, 4, 383.

12. (a) R. Kawahara, K.-i. Fujita and R. Yamaguchi, *Angew. Chem. Int. Ed.*, 2012, 51, 12790-12794; (b) F. Ken-ichi, U. Takehisa and Y. Ryohei, *Chem. Lett.*, 2013, 42, 1496-1498; (c) R. Kawahara, K.-i. Fujita and R. Yamaguchi, *J. Am. Chem. Soc.*, 2012, 134, 3643-3646; (d) K.-i. Fujita, N. Tanino and R. Yamaguchi, *Org. Lett.*, 2007, 9, 109-111; (e) K.-i. Fujita, T. Yoshida, Y. Imori and R. Yamaguchi, *Org. Lett.*, 2011, 13, 2278-2281.

13. R. H. Crabtree, *Energy & Environmental Science*, 2008, 1, 134-138.

14. K.-i. Fujita, Y. Tanaka, M. Kobayashi and R. Yamaguchi, *J. Am. Chem. Soc.*, 2014, 136, 4829-4832.

15. C. M. Moore and N. K. Szymczak, *Chem. Commun.*, 2013, 49, 400-402.

16. C. M. Moore, B. Bark and N. K. Szymczak, *ACS Catalysis*, 2016, 6, 1981-1990.

17. Unpublished results: Fe(dhtp) crystal - Grayson Rich; Ni(dhtp) crystal - Charles Lerhmitte; Co(dhtp) crystal - Eric Dahl.

18. C. M. Moore, D. A. Quist, J. W. Kampf and N. K. Szymczak, *Inorg. Chem.*, 2014, 53, 3278-3280.

19. (a) L. Q. Hatcher and K. D. Karlin, in *Adv. Inorg. Chem.*, eds. R. van Eldik and J. Reedijk, Academic Press, 2006, vol. 58, pp. 131-184; (b) C. E. Elwell, N. L. Gagnon, B. D. Neisen, D. Dhar, A. D. Spaeth, G. M. Yee and W. B. Tolman, *Chem. Rev.*, 2017, 117, 2059-2107; (c) L. M. Mirica, X. Ottenwaelder and T. D. P. Stack, *Chem. Rev.*, 2004, 104, 1013-1046.

20. C. M. Moore and N. K. Szymczak, *Chem. Commun.*, 2015, 51, 5490-5492.

21. C. M. Moore and N. K. Szymczak, *Chem. Sci.*, 2015, 6, 3373-3377.

22. Unpublished results: Cameron Moore and Nathaniel Szymczak.

23. (a) S. K. Russell, J. M. Darmon, E. Lobkovsky and P. J. Chirik, *Inorg. Chem.*, 2010, 49, 2782-2792; (b) D. V. Yandulov and R. R. Schrock, *J. Am. Chem. Soc.*, 2002, 124, 6252-6253.

24. (a) A. S. Borovik, *Acc. Chem. Res.*, 2005, 38, 54-61; (b) R. L. Shook and A. S. Borovik, *Chem. Commun.*, 2008, 6095-6107.

25. (a) A. Wada, M. Harata, K. Hasegawa, K. Jitsukawa, H. Masuda, M. Mukai, T. Kitagawa and H. Einaga, *Angew. Chem. Int. Ed.*, 1998, 37, 798-799; (b) T. Fujii, S. Yamaguchi, Y. Funahashi, T. Ozawa, T. Tosha, T. Kitagawa and H. Masuda, *Chem. Commun.*, 2006, 4428-4430.

26. L. M. Berreau, *Eur. J. Inorg. Chem.*, 2006, 2006, 273-283.

27. Z. Gordon, M. J. Drummond, E. M. Matson, J. A. Bogart, E. J. Schelter, R. L. Lord and A. R. Fout, *Inorg. Chem.*, 2017, 56, 4852-4863.

28. H. S. Soo, A. C. Komor, A. T. Iavarone and C. J. Chang, *Inorg. Chem.*, 2009, 48, 10024-10035.

Chapter 2: Ruthenium (de)hydrogenation catalysis

Portions of this chapter have been published:

Dahl, E. W.; Louis-Goff, T.; Szymczak, N. K.; Second sphere ligand modifications enable a recyclable catalyst for oxidant-free alcohol oxidation to carboxylates *Chem. Commun.* **2017**, *53*, 2287-2289.

2.1 Introduction to dehydrogenative oxidation of alcohols

Although the (re)development of homogeneous catalysts most commonly relies on steric/electronic changes to ligands that are directly coordinated to the metal, modifications that extend beyond the metal's primary sphere can provide additional opportunities for reaction tuning. Changes to a ligand's secondary environment can promote enhanced substrate activation, or alternatively be used to stabilize high-energy intermediates.[1] These principles are widely used in hydrogenase and dehydrogenase enzymes,[2] yet are underutilized in synthetic systems. Our group[3] and others[4] are working to uncover how these key design features can be rationally adapted to enhance synthetic hydrogenation and dehydrogenation catalysis.

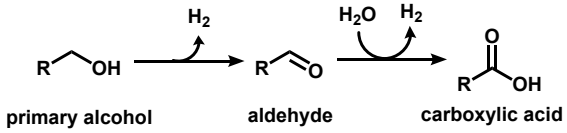

Figure 2-1: General reaction scheme for dehydrogenative alcohol oxidation.

Dehydrogenative alcohol oxidation has recently emerged as a new synthetic strategy to access carboxylates that avoids the use of stoichiometric oxidants and generates H_2 as a reduced byproduct (Figure 2-1).[5] A challenge for this reaction is catalyst stability toward water, a common catalyst poison,[6] that is the source of one of the oxygen atoms in the product. Of the few reported examples of this reaction, most incorporate ligands known to facilitate 'metal-ligand cooperative' pathways;[5a-d,5i] however, general metal-ligand properties needed for this transformation have not been elucidated.

2.2 Motivation for ligand modifications

We previously introduced Ru complexes based on 6,6"-dihydroxyterpyridine (dhtp) as transfer hydrogenation catalysts, which contain design elements reminiscent of the active site of [Fe]-hydrogenase.[2b,3a,3b] We found that although addition of pendent *–OH* groups increased catalyst activity compared to unsubstituted terpyridine (tpy), it also imparted new decomposition pathways. During catalysis, a kinetically *inert* aquo-bridged dimer formed that assembled through hydrogen bonds (H–bonds) between the appended hydroxyl groups and adventitious H_2O (Figure 2-2).[3a] This decomposition route highlights one of the challenges in the field of ligand (re)design: targeted ligand modifications can impact unforeseen and sometimes deleterious characteristics of a metal complex, even from a deceptively simple arrangement in the precatalyst.

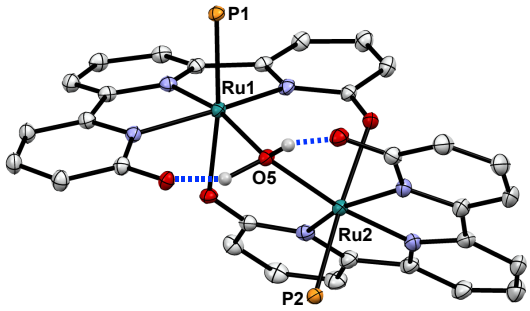

Figure 2-2: Decomposition product of catalyst **2** from adventitious H_2O. CIF file from ref 3a.

We hypothesized that increasing the steric profile of the ligand's secondary sphere would prevent the formation of higher nuclearity aggregates and thus impart greater catalyst stability for hydrogenation and dehydrogenation reactions, particularly in the presence of water or hydroxide. Herein we introduce a new ruthenium complex based on the 6,6"-bis(mesitylamino)-terpyridine (H_2Tpy^{NMes}) ligand,[7] and show that sterically-encumbering mesityl amino groups impart unique stabilization of previously inaccessible Ru-H species (Figure 2-3). This new catalyst overcomes the decomposition pathway of related complexes and provides enhanced catalyst activity and stability in hydrogen transfer reactions containing water, including the oxidant-free dehydrogenative oxidation of primary alcohols to carboxylates.

Figure 2-3: Catalyst **1** features steric protection in the form of 2,4,6-trimethylphenyl (Mes) groups compared to catalyst **2**.

2.3 Synthesis of $Ru(H_2Tpy^{NMes})PPh_3Cl_2$

The ruthenium complex $Ru(H_2Tpy^{NMes})(PPh_3)Cl_2$ (**1**) features an identical primary coordination environment to the –H and –OH variants, yet provides an increased steric profile. Complex **1** was isolated as a purple powder from the reaction of $Ru(PPh_3)_3Cl_2$ with H_2Tpy^{NMes} in refluxing toluene for 18 h. Analogous *cis*-$Ru(L)(PPh_3)Cl_2$ complexes where L = dhtp (**2**)[3a] and tpy (**3**)[8] were similarly prepared for comparative studies. The ^{31}P NMR spectra of **1**-**3** contain resonances at δ = 44.2, 45.9, and 43.1 respectively, consistent with similar ligand fields imposed on Ru by all tpy variants. The solid-state structure of **1** (Figure 2-4) contains an equatorially-bound chloride engaged in H-bonding interactions with the pendent *–NH* groups (average N–Cl distance = 3.07 Å). H–bonding interactions were further evaluated by ^1H NMR spectroscopy. The ^1H NMR spectrum of **1** contains a resonance for the *–NH* groups at δ = 10.56 in $CDCl_3$, significantly downfield of the free ligand *–NH* (δ = 6.08), consistent with an H–bonding interaction with the chloride ligand. These data indicate that the *–NH* groups in **1** provide sterically-protected H–bond donor groups in the secondary sphere that may be used to stabilize reactive intermediates.

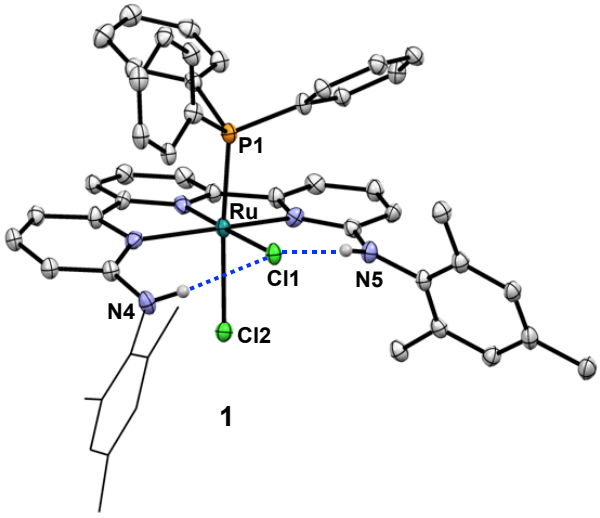

Figure 2-4: ORTEP X-ray crystal structure of **1**. (Ellipsoids at 30% probability. Some mesityl carbon atoms displayed in wireframe for clarity.)

2.4 Isolation of a Ru-hydride using the H_2Tpy^{NMes} ligand

The pendent amine groups in the H_2Tpy^{NMes} ligand provide unique stabilization of a Ru-hydride. The reaction of **1** with PPh_3 and $[NH_4][PF_6]$ followed by $NaBH_4$ in CH_3OH afforded $[Ru(H_2Tpy^{NMes})(PPh_3)_2H]PF_6$ (**1-H)** after 48 h at room temperature (Figure 2-5). This complex contains a Ru-H moiety that engages the pendent mesityl amino *–NH* groups in H–bonding interactions. Under identical reaction conditions, no Ru-H species were obtained when the H_2Tpy^{NMes} ligand was replaced with dhtp. Complex **1-H** contains a rare example of a bifurcated dihydrogen bond[3c,9] and was characterized in the solid- and solution-state. Within the crystal structure, H-atoms involved in dihydrogen bonding were located in the difference map and exhibited asymmetric dihydrogen bond lengths of 1.99 Å and 1.86 Å (average 1.92 Å). Due to the uncertainty of H–H distances obtained from X-ray diffraction, an ^1H NMR experiment was used to augment the XRD data. The ^1H NMR spectrum of **1-H** contains a Ru-H resonance at δ = -6.76 (t, J_{HP} = 21 Hz) in CD_2Cl_2. Evaluation of through-space dipole–dipole induced nuclear spin

relaxation contributions[10] of the Ru-H afforded a dihydrogen bond distance of 1.78 Å at 283 K, consistent with persistent H–bonding interactions in solution.

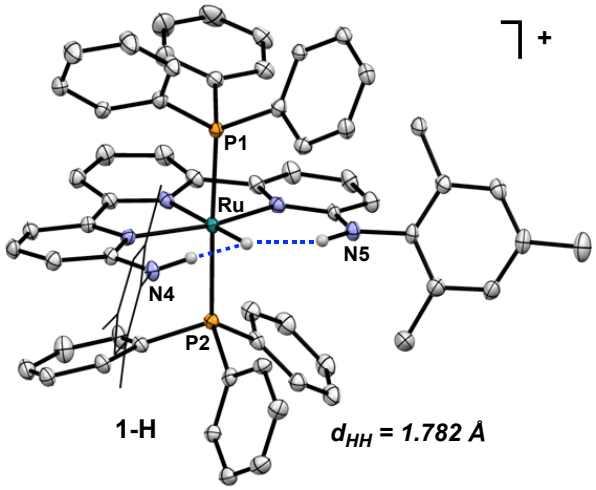

Figure 2-5: ORTEP X-ray crystal structure of **1-H**. (Ellipsoids at 30% probability. Some mesityl carbon atoms displayed in wireframe for clarity.)

One manifestation of the sustained H–H interactions in **1-H** is the lack of H/D exchange for *either* the Ru-H or the pendent *–NH* groups in the presence 100 equiv D_2O after 24 h at 25 °C (Figure 2-6). For comparison, the free ligand (H_2Tpy^{NMes}) underwent complete H/D exchange of the –NH within three minutes under the same conditions. To the best of our knowledge, this is the first example of a dihydrogen bonded metal-hydride resistant to H/D exchange. The isolation of an H_2O stable Ru-H species with H_2Tpy^{NMes} highlights the stabilization imparted by incorporating bulky amine groups. We hypothesized that such stabilization could be exploited for enhanced stability in hydrogen transfer catalysis.

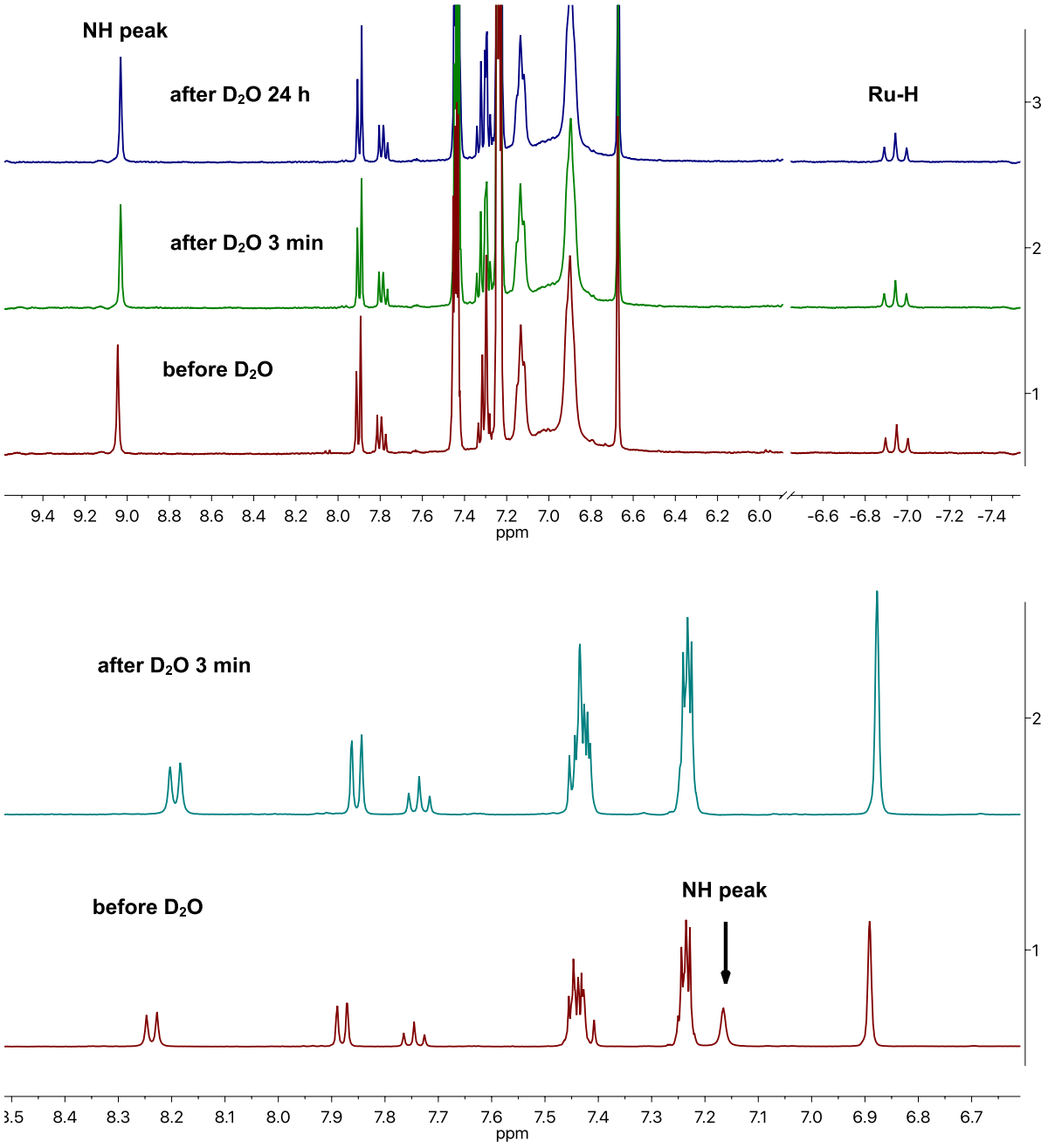

Figure 2-6: H/D exchange ^{1}H NMR spectra of **1-H** (top) and H_2Tpy^{NMes} (bottom) collected at 25°C in THF before and after adding D_2O at the specified times.

2.5 Transfer hydrogenation reactivity

The appended amine donors in **1** dramatically improve both ketone transfer hydrogenation activity and catalyst stability (Figure 2-7). Heating a 500 μL ^{i}PrOH solution containing 0.05 mmol acetophenone, 0.05 mol% **1**, and 1 mol% KO^{t}Bu in an NMR tube under N_2 at 40 °C for 24 h provided 1-phenylethanol in 95% yield (1900 TON). Catalyst stability toward H_2O was also enhanced. When reactions were heated to 80 °C for 12 h with 5% (w/v) exogenous H_2O, a minor drop in yield from 69% (1380 TON) to 56% (1120 TON) 1-phenylethanol was observed for **1**. In contrast, complex **2**, which contains *ortho–OH*, rather than *–NH(Ar)* groups showed a dramatic decrease in yield from 34% (680 TON) to 2% (40 TON) upon addition of H_2O. The transfer hydrogenation studies illustrate that a simple substitution of the pendent groups can have a dramatic effect on catalyst stability. Furthermore, the ability to operate in the presence of H_2O allows access to hydrogen transfer reactions that use H_2O as a reaction component/intermediate.

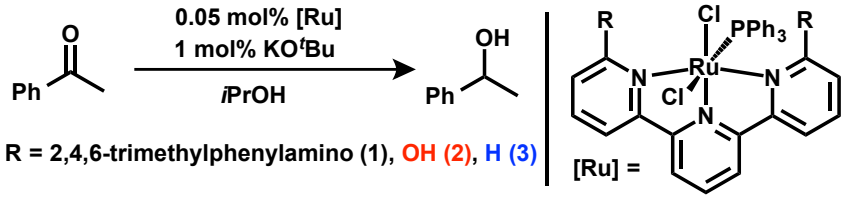

Figure 2-7: Transfer hydrogenation with catalysts **1**, **2**, and **3**.

2.6 Dehydrogenative oxidation reactivity

1 catalyzes the dehydrogenative oxidation of primary alcohols to carboxylates, a reaction that uses H_2O rather than stoichiometric oxidants. Aromatic and aliphatic primary alcohols are oxidized to their corresponding carboxylates in moderate to high yields (Figure 2-8). Standard

reaction conditions employed a 20 mL vial containing 0.5 mmol alcohol, 1.5 mmol KOH, 0.2 mol% **1**, and 2 mL toluene heated to 120°C for 18 hours. Although only one equivalent of KOH is required for the reaction, three equivalents were found to be optimal for the reaction likely due the insolubility of KOH in toluene. After the reaction, the carboxylate product was isolated as the carboxylic acid following an acidic workup. The substrate, cinnamyl alcohol, containing both a primary alcohol and an olefin, was oxidized and hydrogenated to 3-phenylpropionic acid as the major product consistent with hydrogen transfer (hydrogen borrowing) from the alcohol to the internal olefin.[11] Functional group tolerance was evaluated by a substrate robustness screen.[12] We found that **1** tolerates thiophenes (62%), pyrroles (57%), pyridines (51%) and, to a lesser degree, furans (31%). The functional groups tolerated by **1** demonstrate the broader utility of this approach for alcohol oxidation.

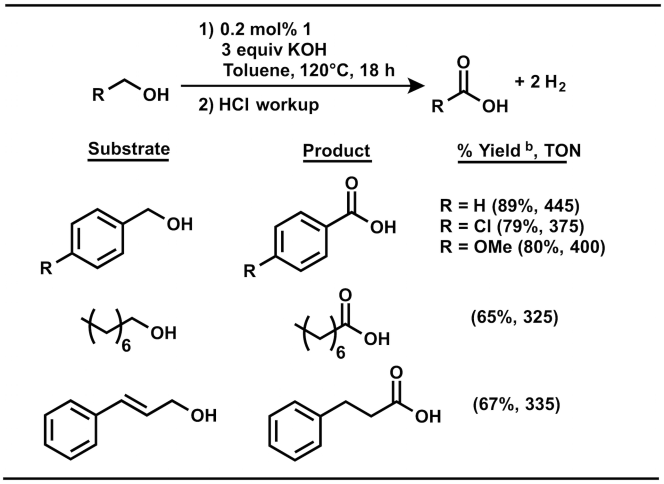

Figure 2-8: Dehydrogenative alcohol oxidation by **1**. [a] Conditions: 0.5 mmol alcohol, 1.5 mmol KOH, 0.001 mmol **1**, 2 mL toluene, 120°C, 18 h. HCl workup affords carboxylic acid. [b] Isolated yield.

2.7 Catalyst recycling

One of the decomposition pathways that hindered hydrogen transfer reactions with **2** (formation of multinuclear aggregates) was overcome using **1** and demonstrated through catalyst recycling experiments. Catalysts **1-3** were subjected to three cycles of dehydrogenative oxidation of benzyl alcohol to assess overall catalyst stability (Figure 2-9). Complexes **1** and **2** show similarly high activity for the first cycle while **3** shows moderate activity. However, **2** and **3** show significant loss in activity over three cycles (total TON = 1120 and 790, cycle three = 9% and 10% yield, respectively). In contrast, the stability provided by the secondary mesityl amino groups in **1** allows for a fully recyclable catalyst (total TON = 2500, cycle three = 85% yield). These data illustrate that catalytic stability across a series of otherwise structurally analogous complexes is dramatically affected by modifications to the metal's secondary coordination sphere environment.

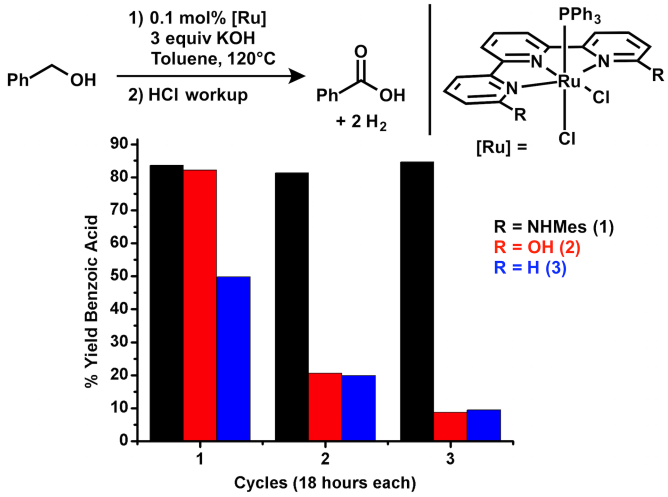

Figure 2-9: Catalyst recycling experiments with 1, 2, and 3. Yields calculated by GC and are the average of two independent runs.

In conclusion, we have demonstrated that the simple substitution from *–H* to *–OH* to *–NH(Ar)* in the secondary sphere of the terpyridine framework can impart dramatic improvements

in catalyst lifetime and activity for Ru-catalyzed hydrogen transfer reactions. This study outlines a design principle to use steric protection around polar secondary groups to stabilize reactive Ru-H intermediates and circumvent catalyst decomposition to impart markedly improved stability and activity for hydrogen transfer reactions. Further efforts will focus on the mechanistic underpinnings that govern these reactivity trends.

The –NHMes groups on H_2Tpy^{NMes} provide an ideal combination of steric protection and secondary H-bonding interactions that produce robust ligands for (de)hydrogenation reactions. In the next chapter, these properties and the meridonal binding of H_2Tpy^{NMes} are used to manipulate the coordination geometry of copper(I) complexes. H-bonding interactions exhibited between the pendent –NH groups and an equatorial Cl ligand in $Ru(H_2Tpy^{NMes})(PPh_3)Cl_2$ are also observed in the complex $Cu(H_2Tpy^{NMes})Cl$ where an unfavorable square planar geometry is forced upon Cu(I). The ability of H_2Tpy^{NMes} to stabilize a Cu(I) geometry more fitting of Cu(II) allows for facile electron transfer reactions that mimic the electron transfer of blue copper proteins.

2.8 Experimental section for chapter 2

General Considerations: All commercially-available reagents were used as received without further purification. All liquid alcohol substrates were distilled from CaH_2 and stored over 3Å molecular sieves prior to use. 6,6"-Bis(2,4,6-trimethylphenylamino)terpyridine (H_2Tpy^{NMes})[7], complex **2**[3a] and complex **3**[8], $Ru(PPh_3)_3Cl_2$[13] were prepared as previously described. KOH, NaOH, and LiOH were dried under vacuum at 150°C overnight and powered using a mortar and pestle or automated grinder before use. All manipulations were carried out under an atmosphere of nitrogen in an Innovative Technologies Pure LabHE GP-1 glovebox or using Schlenk techniques, unless otherwise specified. Degassed, anhydrous solvents were obtained by a SG

Water USA solvent purification system or by drying overnight with CaH_2 followed by distillation. NMR spectra were collected on a Varian MR400, Varian vnmrs 500 or Varian vnmrs 700 and were referenced to residual solvent peaks. ^{31}P NMR spectra were referenced to their respective ^{1}H spectrum. IR spectra were collected on a Nicolet is10 spectrometer using a diamond attenuated total reflectance (ATR) accessory. Elemental analyses were performed by Atlantic Microlabs, Inc., Norcross, Ga.

General Procedure for GC-FID Analysis: Gas chromatography was performed on a Shimadzu GC-2014 equipped with an FID detector and a Shimadzu SH-Rxi-5ms (15 m, 0.25 mm ID, 0.25 μm df) column. H_2 gas was used as the carrier gas. All GC experiments were collected using the following method: 80°C hold for first 2 min, ramp to 300°C at 30°C/min and hold for 2 min. The injector temperature was set to 260°C and the detector was set to 300°C. GC calibration curves were obtained by plotting the response ratios of the areas of $A_{sample}/A_{standard}$ against the known concentrations.

Synthesis of $Ru(H_2Tpy^{NMes})(PPh_3)Cl_2$ (1): To a 100 mL Schlenk flask, 1.0996 g (1.147 mmol) $Ru(PPh_3)_3Cl_2$ and 0.6012 g (1.204 mmol) H_2Tpy^{NMes} was added. The flask was then subjected to multiple vacuum/refill cycles with N_2. 60 mL of bench top toluene (not dry) was then sparged for 6 minutes with N_2 and added to the flask. A reflux condenser was affixed to the flask and the reaction was heated to reflux for 20 hours. Upon cooling to room temperature a purple precipitate formed in the flask. 50 mL of N_2-sparged hexane was added to the flask and the flask was placed in a -25 °C freezer for 16 h. The product was collected on a glass frit in the air, washed with pentane (3 x 10 mL), and dried *in vacuo*. The product was further purified in an N_2-

filled glovebox by dissolution in minimal CH_2Cl_2 followed by precipitation with diethyl ether. The product was isolated by filtration on a glass frit, washed with diethyl ether (2 x 10 mL) and dried *in vacuo* for 16 h to yield 820.8 mg (77% yield) of a purple powder. Purple crystals suitable for X-ray diffraction were grown from a concentrated benzene solution at room temperature. ^{1}H NMR (700 MHz, $CDCl_3$) δ 10.56 (s, 2H), 7.44 (d, *J* = 7.9 Hz, 2H), 7.36 (t, *J* = 7.9 Hz, 1H), 7.20 (dd, *J* = 7.4, 8.5 Hz, 2H), 7.17 (m, 9H), 7.00 (m, 6H), 6.96 (d, *J* = 7.4 Hz, 2H), 6.88 (s, 2H), 6.84 (s, 2H), 5.98 (d, *J* = 8.5 Hz, 2H), 2.29 (s, 6H), 2.26 (s, 6H), 1.96 (s, 6H). ^{31}P NMR (283 MHz, $CDCl_3$) δ 44.2 (s, PPh_3). IR (powder, cm^{-1}): 1614, 1567, 1515, 1467, 1421, 1253, 778. HRMS (ESI-TOF) m/z: [**1** – Cl]$^+$ Calcd for $C_{51}H_{48}ClN_5PRu$: 898.2379; Found: 898.2383.

Synthesis of [Ru(H_2Tpy^{NMes})(PPh_3)$_2$H]PF_6 (1-H): In the air, a 100 mL Schlenk flask was charged with 500.0 mg (0.5354 mmol) **1**, 280.8 mg (1.071 mmol) triphenylphosphine, and 174.6 mg (1.071 mmol) ammonium hexafluorophosphate. The flask was then subjected to multiple vacuum/refill cycles with N_2. 75 mL of N_2-sparged benchtop (not dry) methanol was added to the flask and the solution was allowed to stir at room temperature for 20 hours. The orange product, [Ru(H_2Tpy^{NMes})(PPh_3)$_2$Cl]PF_6, was then converted in one-pot to **1-H** by addition of 202.5 mg (5.354 mmol) sodium borohydride to the reaction flask, causing gas evolution from the dark red reaction solution. After stirring at room temperature for an additional 24 hours the methanol was removed by rotary evaporation to afford a red powder. The solid was brought into a nitrogen-filled glovebox, washed with pentane (3 x 10 mL), dissolved in ~50 mL CH_2Cl_2 and filtered over Celite. The CH_2Cl_2 was concentrated to ~10 mL and ~50 mL diethyl ether was used to precipitate the product as a red solid. The precipitate was filtered, washed with diethyl ether (2

x 10 mL), and dried *in vacuo* overnight affording 456 mg (67 % yield) of **1-H**. Red crystals suitable for X-ray diffraction were grown from toluene. ^{1}H NMR (700 MHz, CD_2Cl_2) δ 8.99 (s, 2H), 7.71 (t, J = 8.0 Hz 1H), 7.64 (d, J = 8.0 Hz, 2H), 7.28 (dd, J = 7.4, 8.3 Hz, 2H), 7.20 (m, 12H), 7.05 (d, J = 7.4 Hz, 2H), 6.95 (m, 16H), 6.73 (s, 4H), 5.68 (d, J = 8.3 Hz, 2H), 2.23 (s, 6H), 1.28 (s, 12H), -6.76 (t, J_{HP} = 21.2 Hz, 1H). ^{31}P NMR (283 MHz, $CDCl_3$) δ 41.5 (s, PPh_3), -144.5 (quint, PF_6). IR (powder, cm^{-1}): 1819 (Ru-H), 1605, 1564, 1497, 1479, 1432, 1418, 1247, 833 (PF_6). HRMS (ESI-TOF) m/z: [**1-H**]$^+$ Anal. calcd for $C_{69}H_{64}F_6N_5P_3Ru$: 1126.3680 Found: 1126.3691.

Details of H–H distance calculation:

The average intramolecular H–H distance between the Ru-hydride and the pendent ligand mesitylamino group in solution was determined by evaluating through-space dipole–dipole induced nuclear spin relaxation contributions.[14] For a detailed example of this analysis from our lab see reference 15. The T_1(min) for **1-H** was estimated by obtaining a T_1 value at variable temperatures (-80°C to 55°C in THF). Although the boiling point of THF limited the maximum temperature that could be reached (and the complete temperature/T_1 profile), we used the temperature T_1 of 10 °C, with a value of 0.1617. The T_1(min) value was then used for the interatomic distance calculation based on the relationship between dipole-dipole relaxation and interatomic distance. Using the crystal structure, the net contribution to the T_1(min) from *all* the atoms, except the pendent mesitylamine protons, was calculated based on distance to the hydride.

The remaining relaxation time contribution was used to calculate the interatomic hydride-NH distance.

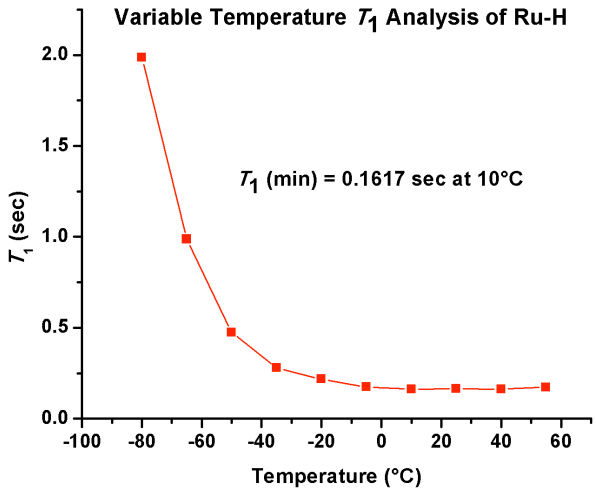

Figure 2-10: VT ^{1}H NMR analysis of Ru-H. Calculated H–H distance: 1.782 Å.

Details of transfer hydrogenation reactions:

Transfer hydrogenation reactions were carried out in NMR tubes using 0.05 mmol acetophenone, 0.0005 mmol KO^{t}Bu, 0.000025 mmol [Ru], and 0.5 mL *i*PrOH. 1.25 mM stock solutions of **1-3** with KO^{t}Bu were prepared and stirred for 10 min to dissolve the catalysts of which 20 µL was added to the respective NMR tube. 5 µL of trimethyl(phenyl)silane (PhTMS) was added to each tube as an internal standard. For each sample, the ^{1}H NMR spectrum was obtained prior to being placed in pre-heated oil bath for the allotted time. Reaction yield was determined by the consumption of the acetophenone resonance against the PhTMS peak. 25µL degassed H_2O (5% w/v) was added to tubes for water stability tests.

Details of H/D exchange experiment:

D_2O was added to NMR samples of **1-H** and H_2Tpy^{NMes} in THF and the progress of H/D exchange was monitored by ^1H NMR spectroscopy against a trimethyl(phenyl)silane internal standard.

General procedure for dehydrogenative oxidation reactions:

In a nitrogen-filled glovebox, a 20 mL glass scintillation vial was charged with KOH (84.1 mg, 1.5 mmol), primary alcohol substrate (0.5 mmol), and a Teflon stir bar. A 2 mL aliquot of a 0.5 mM solution of **1** in toluene was then added to the vial (0.001 mmol, 0.2 mol% **1**). The vial was then sealed with a Teflon-lined cap and placed on a pre-heated aluminum block at 120°C for 18 h while stirring at 1000 rpm. After cooling to room temperature, the vial was removed from the glovebox and H_2O (5 mL) was added to the reaction solution. *Note: the vial may be under positive pressure due to hydrogen gas evolved during acceptorless dehydrogenation.* The organic layer was extracted with ethyl acetate (3 x 5 mL) and discarded. 0.4 mL of a 6 M HCl solution was added to the aqueous layer and the product was extracted with ethyl acetate (3 x 5 mL). The organic fractions were combined, dried over Na_2SO_4, and filtered through a pipette fitted with glass filter paper. The ethyl acetate was removed by rotary evaporation to yield the product carboxylic acid.

Crystallographic Details:

Crystals were mounted on a Rigaku AFC10K Saturn 944+ CCD-based X-ray diffractometer with a low temperature apparatus and Micromax-007HF Cu-target micro-focus rotating anode (λ = 1.54187 A) operated at 1.2 kW power (40 kV, 30 mA). Samples were measured at 85(2)K. The

data were processed with CrystalClear 2.0[16] and corrected for absorption. Structures were solved in Olex2[17] using the XL refinement program[18].

2.9 Notes and references

1 (*a*) S. Werkmeister, J. Neumann, K. Junge and M. Beller, *Chemistry*, 2015, **21**, 12226-12250; (*b*) J. R. Khusnutdinova and D. Milstein, *Angew. Chem. Int. Ed. Engl.*, 2015, **54**, 12236-12273; (*c*) A. S. Borovik, *Acc. Chem. Res.*, 2005, **38**, 54-61; (*d*) M. Rakowski DuBois and D. L. DuBois, *Chem. Soc. Rev.*, 2009, **38**, 62-72; (*e*) M. Zhao, H.-B. Wang, L.-N. Ji and Z.-W. Mao, *Chem. Soc. Rev.*, 2013, **42**, 8360-8375; (*f*) J. Rosenthal and D. G. Nocera, *Acc. Chem. Res.*, 2007, **40**, 543-553.

2 (*a*) W. Lubitz, H. Ogata, O. Rüdiger and E. Reijerse, *Chem. Rev.*, 2014, **114**, 4081-4148; (*b*) C. M. Moore, E. W. Dahl and N. K. Szymczak, *Curr. Opin. Chem. Biol.*, 2015, **25**, 9-17; (*c*) A. Dołęga, *Coord. Chem. Rev.*, 2010, **254**, 916-937.

3 (*a*) C. M. Moore, B. Bark and N. K. Szymczak, *ACS Catalysis*, 2016, **6**, 1981-1990; (*b*) C. M. Moore and N. K. Szymczak, *Chem. Commun.*, 2013, **49**, 400-402; (*c*) J. B. Geri and N. K. Szymczak, *J. Am. Chem. Soc.*, 2015, **137**, 12808-12814; (*d*) K.-N. T. Tseng, J. W. Kampf and N. K. Szymczak, *J. Am. Chem. Soc.*, 2016, **138**, 10378-10381.

4 (*a*) G. Zeng, S. Sakaki, K.-i. Fujita, H. Sano and R. Yamaguchi, *ACS Catalysis*, 2014, **4**, 1010-1020; (*b*) K.-i. Fujita, R. Kawahara, T. Aikawa and R. Yamaguchi, *Angew. Chem. Int. Ed.*, 2015, **54**, 9057-9060; (*c*) K.-i. Fujita, W. Ito and R. Yamaguchi, *ChemCatChem*, 2014, **6**, 109-112; (*d*) K.-i. Fujita, Y. Tanaka, M. Kobayashi and R. Yamaguchi, *J. Am. Chem. Soc.*, 2014, **136**, 4829-4832; (*e*) W.-H. Wang, J. T. Muckerman, E. Fujita and Y. Himeda, *New J. Chem.*, 2013, **37**, 1860-1866; (*f*) S. Chakraborty, P. E. Piszel, W. W.

Brennessel and W. D. Jones, *Organometallics*, 2015, **34**, 5203-5206; (*g*) D. DiMondo, M. E. Thibault, J. Britten and M. Schlaf, *Organometallics*, 2013, **32**, 6541-6554; (*h*) I. Nieto, M. S. Livings, J. B. Sacci, L. E. Reuther, M. Zeller and E. T. Papish, *Organometallics*, 2011, **30**, 6339-6342; (*i*) Y. Suna, M. Z. Ertem, W.-H. Wang, H. Kambayashi, Y. Manaka, J. T. Muckerman, E. Fujita and Y. Himeda, *Organometallics*, 2014, **33**, 6519-6530.

5 (*a*) T. Zweifel, J. V. Naubron and H. Grutzmacher, *Angew. Chem. Int. Ed.*, 2009, **48**, 559-563; (*b*) P. Sponholz, D. Mellmann, C. Cordes, P. G. Alsabeh, B. Li, Y. Li, M. Nielsen, H. Junge, P. Dixneuf and M. Beller, *ChemSusChem*, 2014, **7**, 2419-2422; (*c*) L. Zhang, D. H. Nguyen, G. Raffa, X. Trivelli, F. Capet, S. Desset, S. Paul, F. Dumeignil and R. M. Gauvin, *ChemSusChem*, 2016, **9**, 1413-1423; (*d*) J. H. Choi, L. E. Heim, M. Ahrens and M. H. Prechtl, *Dalton Trans*, 2014, **43**, 17248-17254; (*e*) J. Malineni, H. Keul and M. Moller, *Dalton Trans*, 2015, **44**, 17409-17414; (*f*) H. Li and M. B. Hall, *J. Am. Chem. Soc.*, 2014, **136**, 383-395; (*g*) C. Santilli, I. S. Makarov, P. Fristrup and R. Madsen, *J. Org. Chem.*, 2016, **81**, 9931-9938; (*h*) Z. Dai, Q. Luo, X. Meng, R. Li, J. Zhang and T. Peng, *J. Organomet. Chem.*, 2017, **830**, 11-18; (*i*) E. Balaraman, E. Khaskin, G. Leitus and D. Milstein, *Nat Chem*, 2013, **5**, 122-125.

6 R. H. Crabtree, *Chem. Rev.*, 2015, **115**, 127-150.

7 E. W. Dahl and N. K. Szymczak, *Angew. Chem. Int. Ed.*, 2016, **55**, 3101-3105.

8 B. P. Sullivan, J. M. Calvert and T. J. Meyer, *Inorg. Chem.*, 1980, **19**, 1404-1407.

9 S. Park, R. Ramachandran, A. J. Lough and R. H. Morris, *J. Chem. Soc., Chem. Commun.*, 1994, 2201-2202.

10 P. J. Desrosiers, L. Cai, Z. Lin, R. Richards and J. Halpern, *J. Am. Chem. Soc.*, 1991, **113**, 4173-4184.

11 Although a hydrogen borrowing mechanism is consistent with our data, isomerization of cinnamyl alcohol is an alternative plausible route to 3-phenyl propionic acid.

12 K. D. Collins and F. Glorius, *Nat Chem*, 2013, **5**, 597-601.

13 P. S. Hallman, T. A. Stephenson, G. Wilkinson, *Inorg. Syn*. **1970**, 12, 237.

14 P. J. Desrosiers, L. Cai, Z. Lin, R. Richards, J. Halpern, *J. Am. Chem. Soc.* **1991**, *113*, 4173-4184.

15 J. B. Geri, N. K. Szymczak, *J. Am. Chem. Soc.* **2015**, *137*, 12808-12814

16 CrystalClear Expert 2.0 r12, Rigaku Americas and Rigaku Corporation (2011), Rigaku Americas, 9009, TX, USA 77381-5209, Rigaku Tokyo, 196-8666, Japan.

17 O. V. Dolomanov, L. J. Bourhis, R. J. Gildea, J. A. K. Howard and H. Puschmann. *J. Appl. Cryst.* **2009**, 42, 339-341.

18 G. M Sheldrick, *Acta Cryst. A64***, 2008**, 112-122.

Chapter 3: Hydrogen bonding and the entatic state

Portions of this chapter have been published:

Dahl, E. W.; Szymczak, N. K.; Hydrogen Bonds Dictate the Coordination Geometry of Copper: Characterization of a Square-Planar Copper(I) Complex. *Angew. Chem. Int. Ed.* **2016**, *55*, 3101 – 3105.

3.1 Blue copper proteins and the entatic state

The secondary coordination sphere of blue copper proteins (BCPs) serves a key structural role to regulate the primary geometry of the Type-I copper center.[1] Importantly, the imposed coordination geometry is inextricably tied to rapid electron transfer (ET) processes (10^4-10^6 $M^{-1}s^{-1}$, Figure 3-1), which facilitate electron mobility within the protein.[2] In contrast to the fast ET rates found in copper proteins, synthetic systems generally feature much slower ET rates[3], likely as a result of the large structural differences preferred by Cu(I) and Cu(II) centers. Cu(I) favors tetrahedral coordination while Cu(II) generally adopts distorted octahedral, square planar, or square pyramidal geometries. These differences in the preferred primary coordination geometry naturally impart large barriers for reorganization during ET. To lower the reorganizational barrier and maximize associated ET rates in BCPs, the geometry at copper is regulated by a rich network of non-covalent interactions, which include hydrogen bonds (H-bonds). The surrounding protein scaffold, dubbed the 'rack', stabilizes copper in an intermediate geometry such that structural reorganization is minimized, which allows for fast ET.[4]

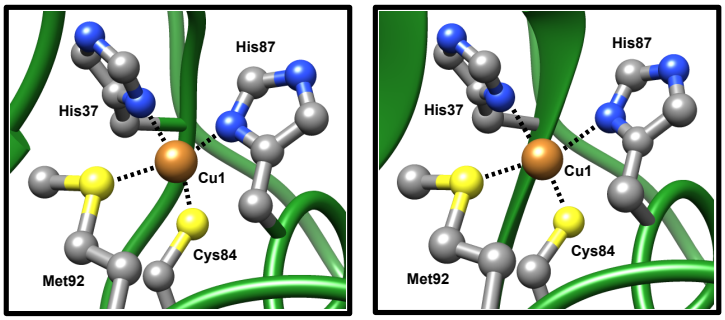

Figure 3-1: Plastocyanin active site with oxidized (left) and reduced (right) copper centers (PDB Files: 1PLC and 4PCY)

This strained geometric state of copper has been referred to as the 'entatic' state, coined by Vallee and Williams,[5] or 'rack-induced' state, coined by Malmström.[4a] The primary coordination sphere electronic environment, as well as noncovalent secondary interactions both contribute to the entatic state.[4b-e] The effects of secondary sphere residues on primary geometry, redox potential, and subsequent ET in BCPs have been examined by numerous research groups.[1b, 6] Concomitant with mutagenesis studies on BCPs, other groups have investigated the entatic state hypothesis by synthesizing small molecule complexes that exhibit minimal structural reorganization upon oxidation and reduction.[3, 7] Typically, the ligand frameworks for these studies exploit steric interactions or a macrocyclic ligand to achieve fast ET rates.[8] In contrast to the covalent coordination strategies most commonly employed by small molecule models, synthetic frameworks incorporating secondary sphere H-bonding interactions as a means to stabilize entatic states are exceedingly rare, yet are critical to the 'rack' in BCPs.[9]

3.2 Motivation for a square planar Cu(I)

Metal-ligand constructs featuring pendent H-bond donors or acceptors are ideal systems in which to probe how H-bonding interactions can impart a given geometric structure in copper complexes. Metal complexes with appended H-bond donors have been used to stabilize reactive intermediates and to enhance reactivity in catalytic reactions.[10] As an alternative, we sought to use H-bonding interactions as the principal design criterion to stabilize an otherwise uncommon square planar Cu(I) geometry (Figure 3-2). By directing H-bonds toward a metal-bound substrate within a rigid pincer framework, herein we demonstrate the stabilization of square planar copper(I) geometries.

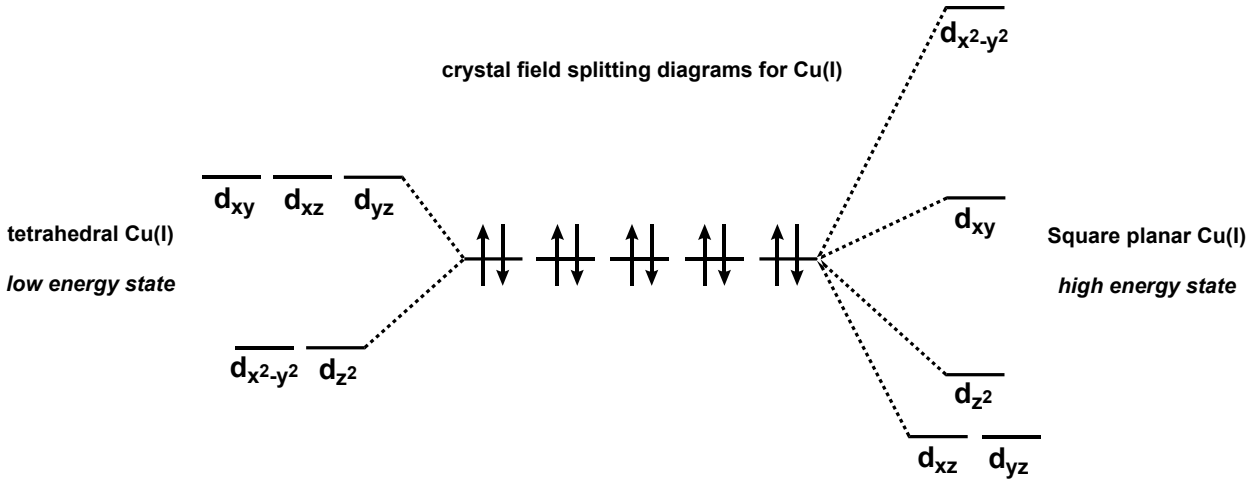

Figure 3-2: Crystal field splitting diagrams for tetrahedral and square planar Cu(I)

The terpyridine framework functionalized in the 6 and 6" positions allows for directed H-bonding interactions with an equatorially-coordinated substrate. Our lab[11] and others[12] have shown that ligands featuring the 2-hydroxypyridine (2-hp) fragment can be employed for cooperative substrate binding, proton-coupled electron transfer, and catalysis.[13] The combination of a metal halide H-bond acceptor[14] with a rigid planar ligand featuring pendent hydroxyl H-bond donors was hypothesized to bind Cu(I) in a square planar geometry. Cu(I) complexes with

the ligand, 6,6”-dihydroxyterpyridine (dhtp),[11a] which incorporates two 2-hp fragments, was initially explored.

Unfortunately, rather than affording the desired square planar compounds, metalations using CuCl with dhtp resulted in the formation of multinuclear clusters (Figure 3-3). To mitigate the challenges associated with limited steric protection, 6,6”-bis(2,4,6-trimethylanilido)terpyridine (H_2Tpy^{NMes}), with pendent secondary anilines, was prepared to provide directed H-bonding interactions within an extended steric environment. Notably, in these systems, both the *–OH* and *–NHAr* groups present potent H-bond donors to a metal-coordinated substrate.[10d, 15]

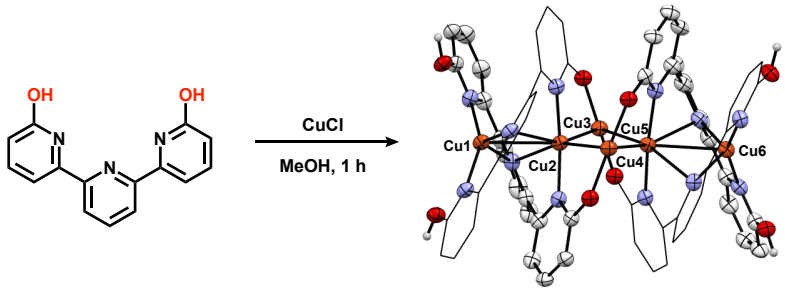

Figure 3-3: Synthesis of $Cu_6(dhtp)_4$ with X-ray crystal structure (30% ellipsoids, H atoms not involved in H-bonding and counterions omitted for clarity)

The H_2Tpy^{NMes} ligand was synthesized in a single step from 6,6”-dibromoterpyridine via nucleophilic substitution with potassium 2,4,6-trimethylanilide. Following an aqueous workup and purification by passage through an alumina plug, the reaction proceeded in 70% yield and can be scaled to gram quantities. Similar 6,6”-substituted terpyridines containing weaker pendent H-bond donor amine groups have been reported previously with R = NH_2, $NH(CH_3)$, $NH(C_2H_5)$.[16] However, their associated coordination chemistry is limited to three reports using Pt and Pd.[16b, 16c, 17]

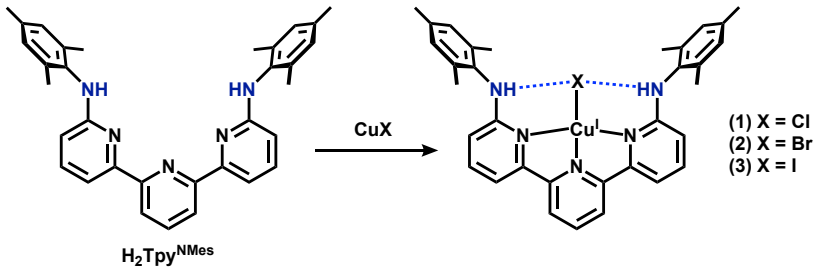

Figure 3-4: Syntheses of complexes **1**, **2**, and **3**.

3.3 Properties of a square planar Cu(I)

3.3.1 Hydrogen bond acceptor dictates geometry

To evaluate the salient structural features imparted by H_2Tpy^{NMes}, Cu(I) complexes were prepared. The synthesis of Cu(H_2Tpy^{NMes})Cl (**1**) occurs over 18 hours by allowing H_2Tpy^{NMes} to react with CuCl in benzene, affording a dark purple precipitate in 83% yield (Figure 3-4). Crystals suitable for an X-ray diffraction experiment were grown from diffusion of pentane into toluene. The solid-state structure of complex **1** revealed a remarkably square planar (SP) geometry, affording a τ_4 value of 0.303 (τ_4=0 for perfectly SP, τ_4=1 for tetrahedral, see following paragraph for calculation)[18] with the pendent anilines engaged in directed H-bonding interactions with the chloride ligand (Avg. Cl–N=3.3 Å). This τ_4 value is highly unusual for a mononuclear Cu(I) complex. We have found only one example that exhibits smaller τ_4 values, and in that case, the geometry is likely enforced by a rigid macrocyclic ligand.[19] To the best of our knowledge, **1** is the most SP mononuclear Cu(I) supported by an acyclic ligand scaffold.[20] The ability of H-bonds to influence the planarity of the N–Cu–X bond angle was evaluated by preparing analogous bromide and iodide complexes, which are weaker H-bond acceptors.[21] Cu(H_2Tpy^{NMes})Br (**2**) and Cu(H_2Tpy^{NMes})I (**3**) were obtained as black and brown crystals respectively from their appropriate copper(I)-halide salts.

The value of τ_4 discussed in this thesis describes the geometry of 4-coordinate metal complexes on a scale from 0 to 1 where $\tau_4 = 0$ describes perfectly square planar complexes and $\tau_4 = 1$ describes perfectly tetrahedral complexes.[18] It is calculated by determining the two largest ligand-metal-ligand bond angles (α and β) in a given 4-coordinate complex and then applying the following equation:

$$\tau_4 = \frac{360° - (\alpha + \beta)}{141°}$$

The solid state structures of **2** and **3** revealed significant deviations from the square planarity observed in **1** (Figure 3-5). For example, the iodide ligand in **3** is distorted away from the terpyridine plane, affording a τ_4 value of 0.548. This structural distortion is consistent with a weakened NH–I H-bond interaction in **3** (Avg. I–N = 3.8 Å) as compared to the NH–Cl interaction in **1**. The H-bond acceptor ability of halide congeners decreases down the group,[22] which parallels the empirical trend noted above and suggests the H-bonding interactions are crucial contributors to the observed geometry in **1**. Non-covalent *inter*molecular interactions may also serve to modify the geometry about copper. We note that several π-π interactions are present in the structures of **1**, **2**, and **3**. Of particular note, **1** and **2** crystallize in the same space group (C2/c), and also feature similar τ_4 values (0.303 and 0.309, for **1** and **2**) in contrast to **3** ($P2_1/c$ space group), which presents a significantly different packing orientation. Thus, we propose that the crystal packing forces (of similar strength to weak/medium H-bonds)[23] can present an alternative, albeit less predictive, driving force for a given geometrical preference, if two limiting structures have similar ground state energies.

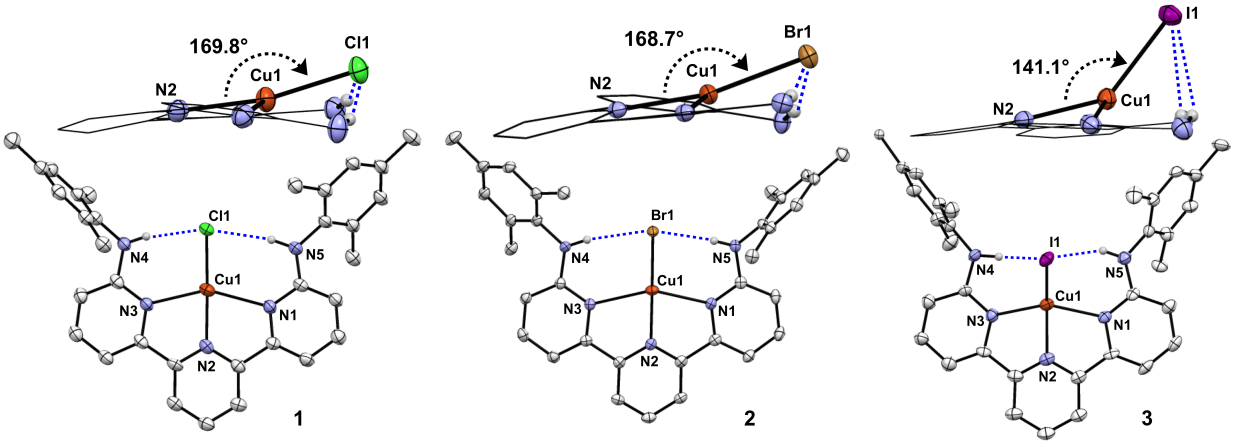

Figure 3-5: X-ray crystal structures of **1**, **2**, and **3** with side-on view to show geometry (30% ellipsoids for **1** and **2**, 50% ellipsoids for **3**, H atoms not involved in H-bonding omitted for clarity, terpyridine backbone shown in wireframe style for side view).

3.3.2 Determining the oxidation state

Due to the unusually dark color of these complexes, as well as solid state geometries that are more reminiscent of Cu(II), we interrogated whether the true oxidation state of complexes **1**-**3** are best described as Cu(I) or Cu(II). Weighardt and co-workers showed that metal-coordinated terpyridines can be redox non-innocent, a situation where an electron resides on the ligand, rather than the metal.[24-25] Importantly, reduction at the terpyridine ligand and oxidation of Cu can be confirmed by careful analysis of the bond distances in the crystal data, X-ray photoelectron spectroscopy (XPS), as well as by the visualization of intraligand π* to π* transitions in the low-energy region of the electronic absorption spectrum.[25] The terpyridine ligand in **1** displays no structural distortions that could be ascribed to ligand-based reduction. For example, the two C_{py}-C'_{py} bonds are equivalent at 1.490(4) Å and 1.483(5) Å, which fall in the reported range of 1.48 ± 0.01 Å for a single bond between two sp^2-hybridized carbon atoms. Furthermore, the average pyridine C-C (1.387(5) Å) and C-N (1.346(4) Å) bond lengths are normal (typical values: 1.38 ± 0.01 Å and 1.35 ± 0.01 Å, respectively). [25]

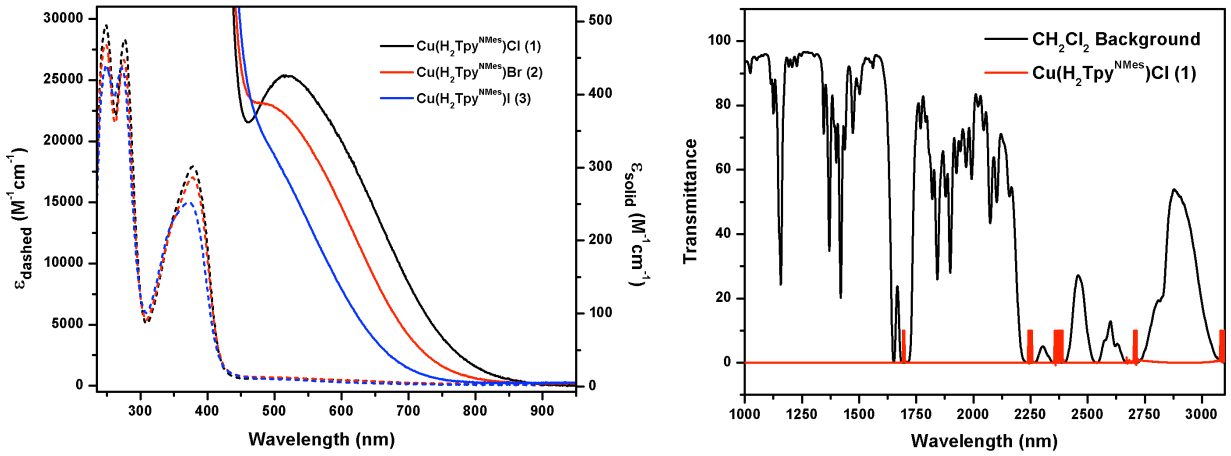

Figure 3-6: UV-Vis spectra overlay of **1**, **2**, and **3** collected in THF. The solid traces correspond to 3.0 mM solutions and the dashed traces to 0.05 mM solution (left). Near-infrared spectrum of **1** in CH_2Cl_2 (2 mM) overlaid with the baseline spectrum to show regions that do not contain relevant data (right).

UV-Vis and near-IR spectroscopy were used to assess the nature of the ground state in **1**. In the visible region (400-1000 nm) one-electron reduced terpyridines contain bands that exhibit $\varepsilon > 2{,}000\ M^{-1}cm^{-1}$.[25] The electronic absorption spectrum of **1**, however, does not exhibit bands with $\varepsilon > 425\ M^{-1}cm^{-1}$ between 400-1000 nm, and thus is inconsistent with a reduced terpyridine unit. Furthermore, the electronic spectrum of **1** in the near-IR region (1000-3000nm) displays no IVCT bands as would be expected for a ligand-reduced terpyridine (Figure 3-6).[25]

To further clarify the oxidation state of the Cu center in **1**, XPS was performed. This technique can distinguish between the binding energies of electrons in Cu 2p orbitals in Cu(I) and Cu(II) complexes, and thus can be used to assign oxidation states.[26] A solid sample of **1** exhibits Cu 2p binding energies (932.2 eV for Cu $2p_{3/2}$) consistent with a Cu(I) oxidation state, which was further confirmed by comparison with an authentic sample of CuCl (Figure 3-7).[26] In contrast to these Cu(I) complexes, the analogous Cu(II) complex **4b** (see below) displays a Cu

$2p_{3/2}$ binding energy of 935.2 eV, in addition to Cu 2p satellite peaks typical for Cu(II) compounds.[26b] Complementary DFT calculations also confirmed that a closed-shell singlet electronic state is the lowest energy state.[27] Collectively, these experimental and theoretical results provide strong evidence for a Cu(I) oxidation state in **1**.

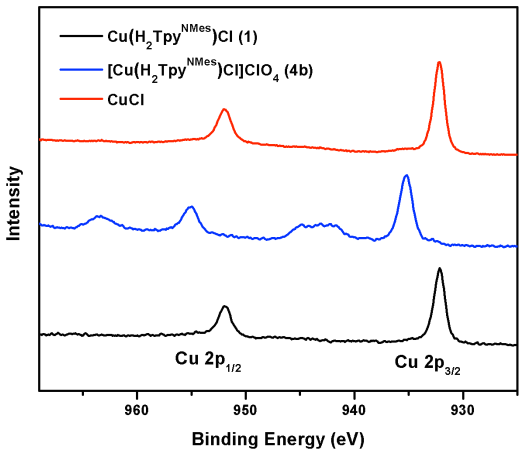

Figure 3-7: Overlay of the Cu 2p region of the XPS spectrum for **1**, **4b**, and CuCl.

3.3.3 ^{1}H NMR evaluation of complexes 1-3

In addition to solid-state and spectrophotometric characterization, both NMR and vibrational spectroscopy provided complementary analyses of the H-bonding in **1-3**. The room temperature ^{1}H NMR spectrum of **1** in CD_2Cl_2 revealed symmetric ligand resonances with a single downfield peak at δ = 8.90, corresponding to two N-H protons (confirmed by H/D exchange in the presence of D_2O) engaged in H-bonding interactions. The terpyridine and mesitylene resonances were unchanged upon halide substitution. In contrast, the NH peak position varied significantly between **1-3** (δ = 8.55 and 7.82 for **2** and **3**, respectively), consistent with persistent H-bonding interactions in solution that weaken with decreasing H-bond accepting ability of the halide (Figure 3-8). Variable temperature NMR experiments revealed static

solution structures of **1** and **2** between -80 to 60°C, while the NMR spectrum of **3** resolved new peaks at -80°C, indicative of a fluxional structure at room temperature. This halide-dependent fluxionality further supports a weakened NH–halide interaction in **3** as compared to **1** and **2**.

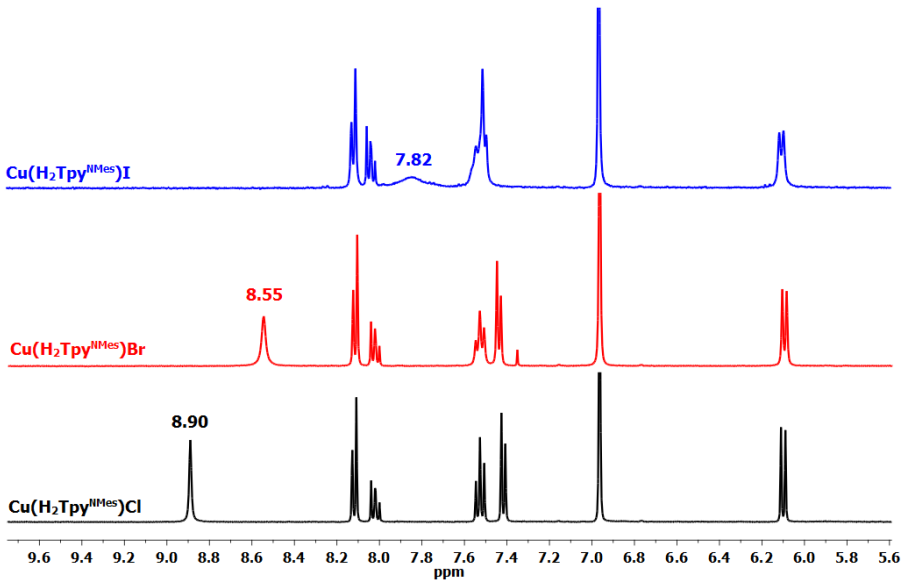

Figure 3-8: ^{1}H NMR (400 MHz) spectra overlay of the aromatic region of **1** (black), **2** (red), and **3** (blue) collected at 25°C in CD_2Cl_2 showing the shift in the N-H proton resonance with varying halide ligands.

3.3.4 IR spectroscopic evaluation of 1-3

IR spectroscopy was used to approximate the NH–halide H-bonding strength in **1-3**. CH_2Cl_2 solutions of **1**, **2**, and **3** feature a single ν_{NH} band at 3234, 3242, and 3256 cm^{-1}, respectively (Figure 3-9). The shift to higher energy is consistent with an increased covalency of the N-H bond and decrease in the H-bond strength, when moving down the halide series. In addition to this qualitative description, the shift of the ν_{NH} bands in the Cu-X complexes, relative to the free ligand (3406 cm^{-1}) in CH_2Cl_2 solvent, was used to evaluate the strength of the H-bonding interactions. The H-bond enthalpy[28] was calculated to be 4.0 kcal/mol for **1**, 3.9

kcal/mol for **2**, and 3.7 kcal/mol for **3** per H-bond. These data clearly delineate the energetic differences in the H-bonding interactions imposed by the varied halide ligands.

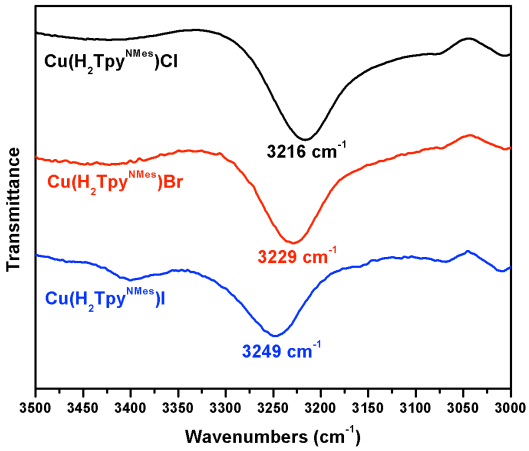

Figure 3-9: Infrared spectrum overlay of **1**, **2** and **3** collected in CH_2Cl_2. The region between 3000 and 3500 cm^{-1} is shown to show shift of N-H stretching frequency.

3.4 Isolation of an entatic state

The square planar geometry of **1** is persistent upon oxidation to Cu(II). Oxidation of **1** with ferrocenium hexafluorophosphate affords $[Cu(H_2Tpy^{NMes})Cl]PF_6$ (**4a**) in 89% yield. Alternatively, treating $CuCl_2$ with H_2Tpy^{NMes} in the presence of $AgClO_4$ similarly afforded $[Cu(H_2Tpy^{NMes})Cl]ClO_4$ (**4b**). An X-ray diffraction experiment using **4b** revealed a square-based pyramidal structure. Other than the presence of an additional axial ClO_4^- ligand in **4**, complexes **1** and **4** are nearly isostructural, as noted by an overlay of the two structures that feature similar τ values (τ_4=0.303 vs τ'=0.358 for complex **1** and **4**, respectively; Figure 3-10). Note that while **4** is five-coordinate, the τ' value was calculated by omitting the ClO_4 ligand and considering the copper as four-coordinate. Much like the active site of BCPs, an interplay of small ligand

distortions coupled with a stabilizing effect from H-bonding interactions allows the Cu(II) geometry to remain relatively unchanged.

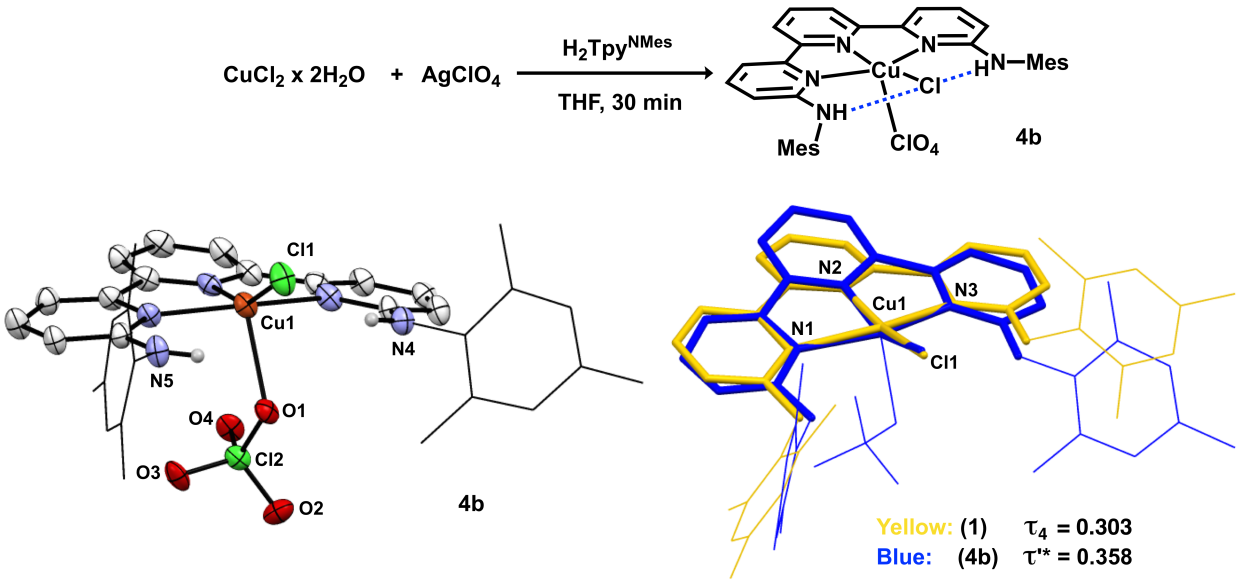

Figure 3-10: Synthesis of **4b** (top). X-ray crystal structure of **4b** (left) and wireframe overlay of **1** and **4b** from the primary sphere atoms (3N, Cu, and Cl) (right).

3.5 Determining the role of H-bonding in entatic state stabilization

The requirement for H-bonding interactions as the main contributor to the square planar geometry in **1** was assessed with a control ligand devoid of H-bond donors. The ligand, 6,6"-bis(2,4,6-trimethylphenoxy)terpyridine, (Tpy^{OMes}), features an isosteric environment to H_2Tpy^{NMes}, without containing H-bond donor groups, and was synthesized via an Ullmann-type coupling. Under the same synthetic conditions as those used to generate **4b**, $[Cu(Tpy^{OMes})Cl]ClO_4$ (**5**) was obtained, and an X-ray quality crystal was grown from diffusion of diethyl ether into a THF solution (Figure 3-11). The absence of H-bonding interactions allows **5** to adopt a geometry that is less square pyramidal (τ_5=0.36) than **4b** (τ_5=0.11). These structural

differences between **5** and **4b** provide clear support that the H-bonding interactions can impart structural distortions in these copper complexes, and allude to H-bonding as the key contributor to the observed geometries in **1-4**.

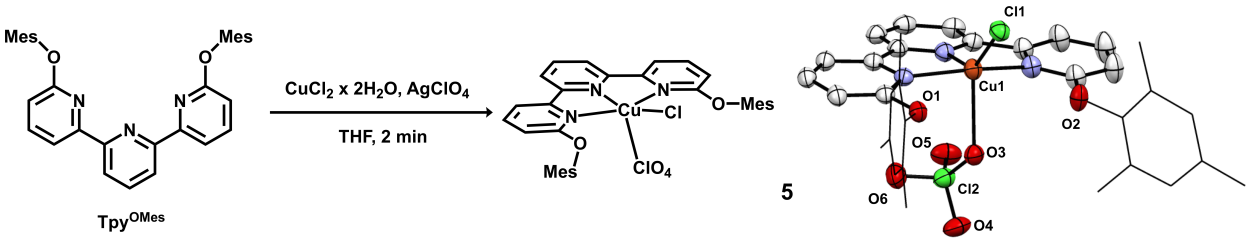

Figure 3-11: Synthesis and X-ray crystal structure of **5** (30% ellipsoids, H atoms omitted for clarity).

In addition to stabilizing a distinct ground state geometry, there are marked differences in the stability between **4** and **5**. In contrast to solutions of **4**, which are stable in THF solution for at least 30 days, **5** is unstable in solution (THF or CH_2Cl_2) and undergoes a disproportionation reaction to afford the homoleptic complex, $[Cu(Tpy^{OMes})_2](ClO_4)$ (**6**), and free $CuCl_2$ in solution. When a THF solution of **5** was subjected to an ESI mass spectrometry experiment, both **5** and **6** were identified (m/z = 599.1 and 532.7). Furthermore, complex **6** was independently synthesized to establish the spectroscopic features contained in solutions of **5**. The difference in solution stability between **4** and **5** was also visualized using cyclic voltammetry. In $[Bu_4N][ClO_4]$ electrolyte, the voltammogram of **5** features an irreversible reduction at +272 mV (vs SCE; Figure 3-12). Additionally, the disproportionation products of **5** were also observed at -223 mV and +790 mV for **6** and $CuCl_2$, respectively. In contrast to this behavior, the voltammogram of either **1** or **4** exhibits a single redox couple at 47 mV (vs SCE, Figure 3-12). This peak is electrochemically reversible, as established by the linear relationship between the peak current

and the square root of the scan rate over three orders of magnitude, the ratio of i_{pa}/i_{pc} = 1, and a peak-to-peak separation similar to that of ferrocene under identical conditions.[29] The differences in solution stabilities, in addition to the irreversible reduction of **5** clearly demonstrates the instability of related Cu(II) and importantly, Cu(I) species without the aid of H-bonding interactions.

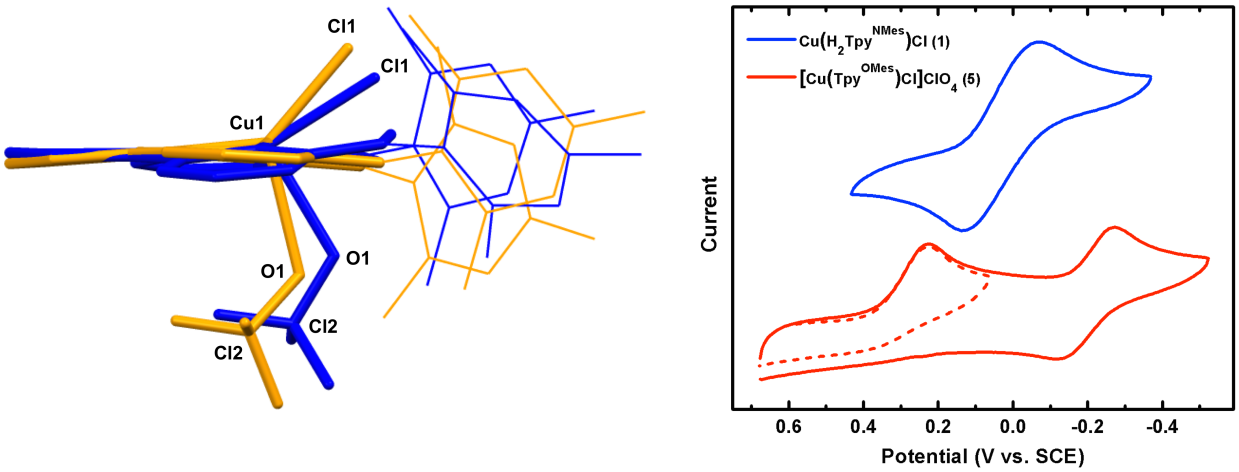

Figure 3-12: Wireframe crystal structure overlay of **4b** and **5** as a side-on view (left) and cyclic voltammetry of **1** and **5** showing reversible $Cu^{I/II}$ event in **1** and irreversible event in **5**.

3.6 Electron transfer self-exchange

We hypothesized that the minimal structural reorganization required for the interconversion between **1** and **4** would allow for extremely facile electron transfer (ET) rates, similar to BCPs. We evaluated the self-exchange ET rate using an NMR line broadening experiment, where the line width of a diamagnetic peak in the ^{1}H NMR spectra of **1** was measured as a function of the concentration of **4**.[3, 30] A plot of [Cu^{II}] vs $\pi\Delta W$ (W=line width in Hz) provided a slope that correlates to an ET self-exchange rate of 2.4 x 10^5 $M^{-1}s^{-1}$ for **1** in THF

at room temperature (Figure 3-13), which is the same order of magnitude as the fasted, reported synthetic systems as well as BCPs (10^4-10^6 $M^{-1}s^{-1}$).[8a, 8b, 31]

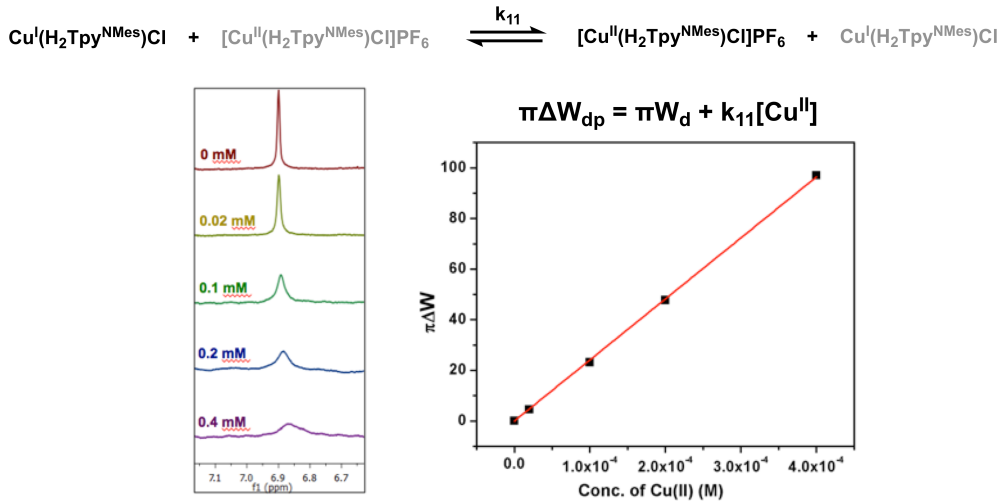

Figure 3-13: Electron transfer self-exchange experiment with **1** and **4a** (top). Broadening of diamagmetic peak on **1** with increased concentration of **4a** (left). Plot of broadening vs. **4a** concentration to extrapolate ET self-exchange rate (k_{11}, right).

In conclusion, we have demonstrated the ability to tune a Cu(I) complex's primary coordination geometry through the use of highly directed, intramolecular H-bonding. The geometry of Cu(I) was reliant on the H-bond strength to the respective metal-bound halides (Cl, Br, and I) with the Cu(I)Cl complex exhibiting a highly unusual square planar geometry. Just as the 'rack' helps stabilize the entatic state in BCPs, oxidation to Cu(II) complexes results in primary geometries at copper that are nearly identical to Cu(I), indicative of an H-bond stabilized entatic state. ET self-exchange reactions between **1** and **4** show extremely fast rates of ET self-exchange (10^5 $M^{-1}s^{-1}$). Although BCPs maintain a pseudo-tetrahedral geometry for both Cu(I) and Cu(II), the fast rates of ET are thought to stem from a minimization of structural reorganization, rather than the specific stabilized geometry. In **1**, the presence of H-bonds are

absolutely critical to the structure and stability, which employ highly directed H-bonds to stabilize a square planar Cu(I) geometry.

In this chapter, we have demonstrated that phenylaminopyridine-based ligands provide the necessary H-bonding and steric interactions to enforce a square planar geometry on copper. In the next chapter, copper complexes bearing a tetradentate 2-phenylaminopyridine-based ligand were synthesized to instead explore H-bonding and electronic perturbations within a trigonal bipyramidal geometry. Substitutions to the *para* position on pendent phenylamino groups allows for electronically tunable ligands of varying H-bond donor strength (pKa). The structural and spectroscopic impacts of adding electronically distinct pendent phenylaminopyridines was explored in the context of H-bonded dicopper and dizinc peroxos derived from oxygen and zinc diazide complexes.

3.7 Experimental section for chapter 3

General Considerations: All commercially-available reagents were used as received without further purification. Benzyl potassium[32] and 6,6"-dihydroxyterpyridine (dhtp)[11a] were prepared according to the literature. All manipulations were carried out under an atmosphere of nitrogen in an Innovative Technologies Pure LabHE GP-1 glovebox or using Shlenk techniques, unless otherwise specified. Degassed, anhydrous solvents were obtained by a SG Water USA solvent purification system or by drying overnight with CaH_2 followed by distillation. NMR spectra were collected on a Varian MR400 and were referenced to residual solvent peaks. IR spectra were collected on a Nicolet is10 spectrometer as KBr pellets, a diamond attenuated total reflectance (ATR) accessory, or as a solution in CH_2Cl_2 between KBr plates. EPR spectra were collected on a Bruker EMX EPR spectrometer. Electronic absorption spectra were collected on a

Varian Cary-50 spectrophotometer. Near-infrared spectroscopic data was obtained on a Varian Cary-5000 spectrophotometer. X-ray photoelectron spectra were recorded on a Kratos Axis Ultra XPS (8 mA, 14 keV, Monochromatic Al) and referenced to C1s at 284.8 eV. Powder samples for XPS were prepared as a thin layer on double-sided carbon tape and mounted a glass slide. Voltammetry experiments were conducted using a Pine WaveNow potentiostat under N_2 in a cell consisting of a glassy carbon working electrode, platinum counter electrode and a silver wire reference electrode. All voltammetry experiments were referenced to SCE via an internal ferrocene reference introduced at the end of the experiment (Fc/Fc^+ = 0.46V vs SCE in CH_2Cl_2)[33] Elemental analyses were performed by Midwest Microlabs, LLC, Indianapolis, IN.

Synthesis of 6,6"-bis(2,4,6-trimethylanilido)terpyridine (H_2Tpy^{NMes}): 10 mL of THF was added to 600.0 mg (4.608 mmol) of benzyl potassium to form a dark red solution. 0.776 mL (5.530 mmol) of 2,4,6-trimethylaniline was then added to the solution causing a loss of color to yield a light red solution. This solution was stirred for 1 min then added to a slurry of 360.4 mg (0.922 mmol) and 6,6"-dibromoterpyridine in 10 mL THF. The solution was stirred at room temperature for 1 hour then quenched with a solution of saturated ammonium chloride. The organic layer was removed and the aqueous phase was washed with CH_2Cl_2. The organic phase was dried over $MgSO_4$, filtered and solvent was removed via rotary evaporation. Methanol was added to the resulting crude oil to precipitate a yellow solid, which was collected on a glass frit and washed with a minimal amount of methanol followed by pentane. The yellow solid was further purified by dissolving in dichloromethane and passage through a plug of basic alumina (4 x 3 cm). The CH_2Cl_2 was removed *in vacuo* to isolate 325 mg (70% yield) of an off-white powder. If desired, a crystalline sample can be obtained by recrystallization from hot toluene.

Elemental analysis was obtained from this sample. ^{1}H NMR (700 MHz, $CDCl_3$) δ: 8.36 (d, *J* = 7.8 Hz, 2H), 7.96 (d, *J* = 7.4 Hz, 2H), 7.91 (t, *J* = 7.8 Hz, H), 7.53 (dd, *J* = 7.4, 8.2 Hz, 2H), 6.98 (s, 4H), 6.08 (s, 2H), 6.05 (d, *J* = 8.2 Hz, 2H), 2.33 (s, 6H), 2.24 (s, 12H). ^{13}C NMR (175 MHz, $CDCl_3$) δ: 157.7, 155.8, 155.3, 138.7, 137.6, 136.8, 136.5, 134.1, 129.4, 120.7, 111.4, 105.9, 21.1, 18.6. IR (CH_2Cl_2, cm^{-1}): 3406 (N-H). Anal. calcd for C33H33N5: C, 79.33; H, 6.66; N, 14.02. Found: C, 79.45; H, 6.85; N, 13.74.

Synthesis of Cu(H_2Tpy^{NMes})Cl (1): 80.8 mg (0.162 mmol) of H_2Tpy^{NMes} in 10 mL of benzene was added to a vial containing 15.2 mg (0.154 mmol) copper(I) chloride. The solution was stirred at room temperature for 18 hrs, then the solvent was removed *in vacuo*. The crude black solid was collected on a sintered glass frit and washed with MeCN (3 x 2 mL) followed by diethyl ether (3 x 2 mL). The solid was washed through the frit with minimal CH_2Cl_2. The CH_2Cl_2 was concentrated and layered with diethyl ether and placed in a -33°C freezer overnight. The product precipitates as microcrystalline purple needles. The supernatant was decanted and the precipitate was dried under vacuum affording a 77.1mg (84%) yield. Crystals suitable for X-ray were grown from pentane diffusion into a concentrated toluene solution of **1** at 3°C. ^{1}H NMR (700 MHz, CD_2Cl_2) δ: 8.90 (s, 2H), 8.11 (d, *J* = 7.8 Hz, 2H), 8.02 (t, *J* = 7.8 Hz, 1H), 7.52 (dd, *J* = 8.3, 7.4 Hz, 2H), 7.41 (d, *J* = 7.4 Hz, 2H), 6.98 (s, 4H), 6.10 (d, *J* = 8.3 Hz, 2H), 2.31 (s, 6H), 2.26 (s, 12H). ^{13}C NMR (175 MHz, CD_2Cl_2) δ: 158.9, 153.3, 150.6, 139.0, 138.5, 136.9, 136.7, 134.2, 129.5, 122.1, 110.6, 108.3, 21.1, 18.7. IR (CH_2Cl_2, cm^{-1}): 3234 (N-H). UV-vis (THF): 519 nm (425 $M^{-1}cm^{-1}$), 378 nm (17900 $M^{-1}cm^{-1}$), 276 nm (28300 $M^{-1}cm^{-1}$), 249 nm (29500 $M^{-1}cm^{-1}$). Anal. calcd for C33H33ClCuN5: C, 66.21; H, 5.56; N, 11.70. Found: C, 66.48; H, 5.45; N, 11.72.

Synthesis of Cu(H_2Tpy^{NMes})Br (2): The preparation and purification is the same as for **1**. From 50.5 mg (0.101 mmol) of H_2Tpy^{NMes} and 13.8 mg (0.096 mmol) of copper(I) bromide, 48.0 mg (78% yield) of **2** can be obtained as a black crystalline powder. Crystals suitable for X-ray were grown from pentane diffusion into a concentrated toluene solution of **2** at 3°C. ^{1}H NMR (700 MHz, CD_2Cl_2) δ: 8.55 (s, 2H), 8.12 (d, *J* = 7.8 Hz, 2H), 8.03 (t, *J* = 7.8 Hz, 1H), 7.53 (dd, *J* = 8.3, 7.3 Hz, 2H), 7.44 (d, *J* = 7.3 Hz, 2H), 6.97 (s, 4H), 6.10 (d, *J* = 8.3 Hz, 2H), 2.31 (s, 6H), 2.27 (s, 12H). ^{13}C NMR (175 MHz, CD_2Cl_2) δ: 158.8, 153.5, 150.8, 139.1, 138.7, 137.1, 136.9, 134.0, 129.5, 122.2, 110.8, 108.5, 21.1, 18.8. IR (CH_2Cl_2, cm^{-1}): 3242 (N-H). UV-vis (λ_{max}, nm (ε, $M^{-1}cm^{-1}$)): 378 nm (17100 $M^{-1}cm^{-1}$), 275 nm (26700 $M^{-1}cm^{-1}$), 248 nm (27900 $M^{-1}cm^{-1}$). Anal. calcd for C33H33BrCuN5: C, 61.63; H, 5.17; N, 10.89. Found: C, 61.09; H, 5.30; N, 10.63.

Synthesis of Cu(H_2Tpy^{NMes})I (3): 63.2mg (0.127 mmol) of H_2Tpy^{NMes} in 5mL of THF was added to a vial containing 22.9mg (0.121 mmol) copper(I) iodide. The solution was stirred at room temperature for 18 hrs then the solvent was removed *in vacuo*. After washing the resulting solid with MeCN and pentane, the product was washed through a sintered glass frit with THF and the solution was concentrated, layered with pentane, and stored in a -33°C freezer overnight. Following removal of the supernatant, the product was dried under vacuum providing 59.2mg (71% yield) of a black powder. X-ray quality crystals were obtained from slow diffusion of diethyl ether into a concentrated CH_2Cl_2 solution at 3°C. ^{1}H NMR (400 MHz, CD_2Cl_2) δ: 8.12 (d, *J* = 7.1 Hz, 2H), 8.03 (t, *J* = 7.1 Hz, 1H), 7.82 (s, 2H), 7.54 (dd, 2H), 7.51 (d, 2H), 6.96 (s, 4H), 6.11 (d, 2H), 2.30 (s, 6H), 2.24 (s, 12H). ^{13}C NMR (175 MHz, CD_2Cl_2) δ: 158.3, 154.2,

151.2, 139.2, 139.0, 137.2, 137.1, 133.5, 129.6, 122.5, 111.5, 108.6, 21.1, 19.1. IR (CH_2Cl_2, cm^{-1}): 3256 (N-H). UV-vis (THF): 371 nm (15000 $M^{-1}cm^{-1}$), 271 nm (26000 $M^{-1}cm^{-1}$), 249 nm (26300 $M^{-1}cm^{-1}$). Anal. calcd for C33H33CuIN5: C, 57.43; H, 4.82; N, 10.15. Found: C, 57.81; H, 4.93; N, 10.04.

Synthesis of [Cu(H_2Tpy^{NMes})Cl]PF_6 (4a): 30.2 mg (0.0505 mmol) of **1** was dissolved in 3mL CH_2Cl_2 and was added to a vial containing a 15.9 mg (0.0480 mmol) ferrocenium hexafluorophosphate in 2 mL CH_2Cl_2. The reaction mixture was stirred for 30 min at room temperature until a dark green solution developed. The CH_2Cl_2 was removed *in vacuo* and the resulting dark green precipitate was transferred to a sintered glass frit with benzene and filtered. The precipitate was then washed with benzene (2 x 2 mL) to remove excess **1** and ferrocene and then pentane. The precipitate was washed through the frit with minimal THF. Diethyl ether was added to precipitate the product over 12 hours in a -33°C freezer. 30.6 mg (89% yield) of a dark brown solid was obtained after decanting the supernatant and drying under vacuum. IR (solid, cm^{-1}): 3251. UV-vis (THF): 765 nm (117 $M^{-1}cm^{-1}$), 407 nm (18500 $M^{-1}cm^{-1}$), 275 nm (19400 $M^{-1}cm^{-1}$), 244 nm (30600 $M^{-1}cm^{-1}$). ESI-MS (m/z) 597.2 $[M\text{-}PF_6]^+$ Anal. calcd for C33H33ClCuF6N5P: C, 53.30; H, 4.47; N, 9.42. Found: C, 53.54; H, 4.63; N, 9.31.

Synthesis of [Cu(H_2Tpy^{NMes})Cl]ClO_4 (4b): *Note that perchlorate salts are potentially explosive and care must be taken when handling dry solids. We used small scale preparations (< 10 mg) to minimize risk associated with this synthesis.*

In the air, 8.2 mg (0.048 mmol) of $CuCl_2 \cdot 2H_2O$ was stirred in 2 mL THF until all dissolved. A solution of 25.1 mg (0.050 mmol) of H_2Tpy^{NMes} in 2 mL THF was then added while stirring at

room temperature. A dark orange solid precipitated from the reaction mixture immediately. After 5 min, a solution of 10.9mg (0.053 mmol) AgClO4 in 1 mL THF was added dropwise over 30 seconds. The reaction mixture immediately turned dark brown as much of the precipitate went back into solution. After stirring 30 min at room temperature, the solvent was removed from the reaction mixture via rotary evaporation. The crude product was then brought into the glovebox for recrystallization. 10 mL CH_2Cl_2 was used to dissolve the product and the yellow solution was filtered using a pipette containing glass filter paper. The CH_2Cl_2 was removed *in vacuo* and 1 mL THF was added followed by 6mL ether to precipitate a yellow powder. The supernatant was decanted and the product dried under vacuum to give 25.2 mg (67%) yield. Crystals suitable for X-ray diffraction were grown from slow diffusion of methyl tert-butyl ether into a saturated THF solution. IR (solid, cm^{-1}): 3246. UV-vis (THF): 769 nm (153 $M^{-1}cm^{-1}$), 406 nm (19300 $M^{-1}cm^{-1}$), 276 nm (21800 $M^{-1}cm^{-1}$), 244 nm (34200 $M^{-1}cm^{-1}$). ESI-MS (m/z) 597.2 $[M\text{-}ClO_4]^+$ Anal. calcd for C33H33Cl2CuN5O4: C, 56.78; H, 4.76; N, 10.03. Found: C, 56.72; H, 4.70; N, 10.00.

Synthesis of 6,6"-bis(2,4,6-trimethylphenoxy)terpyridine (Tpy^{OMes}): Potassium 2,4,6-trimethylphenoxide was prepared prior to the experiment by allowing 937.1 mg (6.88 mmol) 2,4,6-trimethylphenol to react with 746.6 mg (5.73 mmol) of benzyl potassium in THF. The reaction was stirred for 5 min, followed by removal of the solvent *in vacuo* to afford a colorless oil. Benzene (*ca.* 10 mL) was added to precipitate the product as a white solid. The product was washed with benzene (3 x 5 mL) and pentane (3 x 5 mL), dried under vacuum, and used without further purification for the next step. A 20 mL scintillation vial was charged with 150.7 mg (0.385 mmol) 6,6"-dibromoterpyridine, 167 mg (0.963 mmol) potassium 2,4,6-

trimethylphenoxide, 36.6 mg (0.193 mmol) copper(I) iodide, and 10 mL toluene. The vial was capped and the mixture was heated at 80°C for 18 hours. The reaction mixture was then removed from the glovebox and, in the air, the reaction mixture was passed through a plug of neutral alumina (4 x 3 cm) and the alumina was washed with CH_2Cl_2 (20 mL). Solvent was removed from the colorless organic filtrate by rotatory evaporation. The oil was triturated with pentane to afford 165 mg (85% yield) of a white crystalline powder after drying under vacuum. ^{1}H NMR (400 MHz, $CDCl_3$) δ: 8.27 (d, *J* = 7.4 Hz, 2H), 8.11 (d, *J* = 7.8 Hz, 2H), 7.77 (dd, *J* = 8.1, 7.4 Hz, 2H), 7.75 (t, *J* = 7.8 Hz, 1H), 6.93 (s, 4H), 6.70 (d, *J* = 8.1 Hz, 2H), 2.33 (s, 6H), 2.13 (s, 12H). ^{13}C NMR (100 MHz, $CDCl_3$) δ: 162.9, 154.9, 154.8, 148.4, 140.3, 137.9, 134.6, 130.9, 129.4, 121.3, 114.9, 109.0, 21.0, 16.7. Anal. calcd for C33H31N3O2: C, 79.02; H, 6.23; N, 8.38. Found: C, 79.20; H, 6.33; N, 8.30.

Synthesis of [Cu(Tpy^{OMes})Cl]ClO_4 (5): *Note that perchlorate salts are potentially explosive and care must be taken when handling dry solids. We used small scale preparations (< 10 mg) to minimize risk associated with this synthesis.*

In the air, 5.9 mg (0.0347 mmol) $CuCl_2 \cdot 2H_2O$ was stirred in 2 mL THF until complete dissolution. To this mixture was added a solution of 17.4 mg (0.0347 mmol) Tpy^{OMes} in 2 mL THF while stirring at room temperature. A yellow solid precipitated from the reaction mixture immediately. After 5 min, a solution of 7.2 mg (0.0347 mmol) $AgClO_4$ in 1 mL THF was added dropwise over 30 seconds. After stirring for 2 minutes, the reaction mixture was filtered through 545 celite and the solvent was removed via rotary evaporation. A minimal amount of THF (*ca*. 1 mL) was added to the dry reaction mixture and the solution was filtered through 545 celite, and diethyl ether was allowed to diffuse into this solution at 3°C, green crystals suitable for X-ray

were obtained. Note: as noted in the main text, solutions of this compound (from X-ray quality crystals) are not stable, and exist as a mixture of disproportionation products ($CuCl_2$ and **6**). Furthermore, solutions (THF or DCM) of this complex slowly precipitate a light green solid that we have identified as a to **6** and free $CuCl_2$ by cyclic voltammetry, ESI-MS, and EPR spectroscopy. ESI-MS (m/z) 599.1 $[M\text{-}ClO_4]^+$

Synthesis of $[Cu(Tpy^{OMes})_2](ClO_4)_2$ (6): *Note that perchlorate salts are potentially explosive and care must be taken when handling dry solids. We used small scale preparations (< 10 mg) to minimize risk associated with this synthesis.*

In the air, 3.1 mg (0.0183 mmol) $CuCl_2 \cdot 2H_2O$ was dissolved in 2 mL THF in a 20 mL scintillation vial at room temperature. 7.6 mg (0.0366 mmol) of AgClO4 was then dissolved in 1 mL THF and added to the stirring $CuCl_2$ solution. After 5 min, the solution was filtered with a glass pipette fitted with glass filter paper into a new 20 mL scintillation vial. A solution of 18.4 mg (0.0366 mmol) Tpy^{OMes} in 1 mL THF was then added dropwise over 30 seconds, immediately precipitating a light green solid. The reaction mixture was stirred for 30 min at room temperature. The light green precipitate was collected on a sintered glass frit and washed with THF (3 x 3 mL) and pentane (3 x 3 mL) then passed through the frit with CH_2Cl_2. The solvent was removed *in vacuo* providing 22.6mg (97% yield) of a light green powder. UV-vis (CH_2Cl_2): 734 nm (50 $M^{-1}cm^{-1}$), 355 nm (70700 $M^{-1}cm^{-1}$), 341 nm (62700 $M^{-1}cm^{-1}$), ESI-MS (m/z) 532.7 $[M\text{-}2ClO_4]^{2+}$ Anal. calcd for C66H66Cl2CuN6O12: C, 62.63; H, 4.94; N, 6.64. Found: C, 62.73; H, 4.89; N, 6.50.

Synthesis of $[Cu_6(dhtp)_4](CuCl_2)_2$ ($Cu_6(dhtp)_4$): 4.6 mg (0.046 mmol) CuCl and 12.2mg (0.046 mmol) was stirred in 4 mL methanol for 1 hour at room temperature. The solvent was then removed *in vacuo*. A red solid was collected. Red crystals suitable for X-ray diffraction were grown from slow diffusion of diethyl ether into a concentrated DMF solution. ^{1}H NMR (400 MHz, DMSO-d_6) δ: 12.50 (s, 4H), 8.16 (d, 4H), 8.10 (t, 2H), 7.59 (dd, 4H), 7.07 (d, 4H), 6.49 (d, 4H).

Computational Details:

All calculations were performed using Gaussian 09[34] and visualized in GaussView. The atoms C and H were calculated to the double-zeta level of theory with the Pople basis set 6-31G(d,p)[35] and the primary sphere atoms Cu, N, and Cl were calculated to the triple-zeta level of theory with the Ahlrich basis set def2-TZVP.[36] Structure benchmarking was performed with Lee, Yang, and Parr's functional (B3LYP)[37], Truhlar and Zhao's pure (M06L)[38] and hybrid (M06)[39] functional, and Head-Gordon's long range-corrected functional (wB97XD).[40] Spin-unrestricted structures were freely optimized in C_1 symmetry from coordinates generated from the X-ray structure using a polarizable continuum model (PCM) of CH_2Cl_2. Optimized structures were verified to be minima on the potential energy surface (PES) by absence of imaginary frequencies in the calculated vibrational spectra and/or by independent stability calculations.

Structural Benchmarking:

Benchmarking was performed to determine the functional that best predicts the observed geometry of **1**. Hybrid functionals with varying Hartree-Fock contributions (20-27%) were used along with the M06L pure functional. The 6-31G and def2-TZVP basis sets were chosen because of their successful use in a similar system.[41] Results for the optimized geometric parameters are given in Figure 3-14. The M06 and wB97XD functionals gave the best parameters with τ_4 values, angles, and bond lengths closely resembling the crystal structure of **1**. The M06, wB97XD, and B3LYP functionals were used for the singlet ground state analysis.

Functional	B3LYP	wB97xd	M06
Energy Difference (kcal/mol)	29.65	31.95	34.22

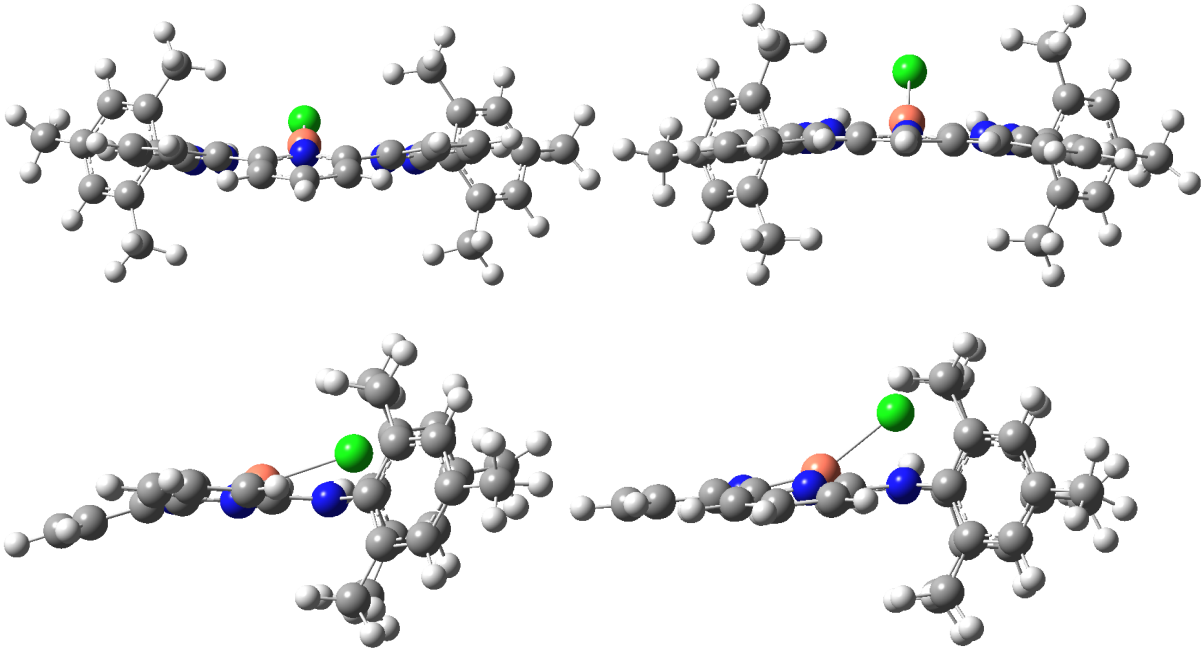

Figure 3-14: Representative optimized structures (wB97XD functional) for the singlet (left) and triplet (right) state showing ligand distortions in the singlet state.

Crystallographic Details:

Crystals were mounted on a Rigaku AFC10K Saturn 944+ CCD-based X-ray diffractometer with a low temperature apparatus and Micromax-007HF Cu-target micro-focus rotating anode (λ = 1.54187 A) operated at 1.2 kW power (40 kV, 30 mA). Samples were measured at 85(2)K. The data were processed with CrystalClear 2.0[42] and corrected for absorption. Structures were solved in Olex2[43] using the XL refinement program[44]. The SQUEEZE[45] function found in PLATON was used to model residual electron density caused by disordered solvent in **5** and $Cu_6(dhtp)_4$.

3.8 Notes and references

1 (a) H. B. Gray, B. G. Malmström, R. J. Williams, *J. Biol. Inorg. Chem.* **2000**, *5*, 551-559; (b) M. C. Machczynski, H. B. Gray, J. H. Richards, *J. Inorg. Biochem.* **2002**, *88*, 375-380; (c) J. J. Warren, K. M. Lancaster, J. H. Richards, H. B. Gray, *J. Inorg. Biochem.* **2012**, *115*, 119-126.

2 C. Dennison, *Coord. Chem. Rev.* **2005**, *249*, 3025-3054.

3 D. B. Rorabacher, *Chem. Rev.* **2004**, *104*, 651-698.

4 (a) B. G. Malmström, *Eur. J. Biochem.* **1994**, *223*, 711-718; (b) E. I. Solomon, M. J. Baldwin, M. D. Lowery, *Chem. Rev.* **1992**, *92*, 521–542; (c) J. A. Guckert, M. D. Lowery, E. I. Solomon, *J. Am. Chem. Soc.* **1995**, *117*, 2817–2844; (d) U. Ryde, M. H. Olsson, K. Pierloot, B. O. Roos, *J. Mol. Biol.* **1996**, *261*, 586–596; (e) P. Comba, *Coord. Chem. Rev.* **2000**, *200*, 217–245.

5 B. L. Vallee, R. J. Williams, *Proc. Natl. Acad. Sci. U.S.A.* **1968**, *59*, 498-505.

6 (a) N. M. Marshall, D. K. Garner, T. D. Wilson, Y.-G. Gao, H. Robinson, M. J. Nilges, Y. Lu, *Nature* **2009**, *461*, 113-116; (b) S. Y. New, N. M. Marshall, T. S. A. Hor, F. Xue,

Y. Lu, *Chem. Commun.* **2012**, *48*, 4217-4219; (c) G. Van Pouderoyen, S. Mazumdar, N. I. Hunt, A. O. Hill, G. W. Canters, *Eur. J. Biochem.* **1994**, *222*, 583-588; (d) C. Libeu, M. Kukimoto, M. Nishiyama, S. Horinouchi, E. T. Adman, *Biochemistry* **1997**, *36*, 13160-13179; (e) C. J. Carrell, D. Sun, S. Jiang, V. L. Davidson, F. S. Mathews, *Biochemistry* **2004**, *43*, 9372-9380.

7 (a) A. Hoffmann, S. Binder, A. Jesser, R. Haase, U. Flörke, M. Gnida, M. Salomone-Stagni, W. Meyer-Klaucke, B. Lebsanft, L. E. Grünig, S. Schneider, M. Hashemi, A. Goos, A. Wetzel, M. Rübhausen, S. Herres-Pawlis, *Angew. Chem. Int. Ed.* **2013**, *53*, 299-304; (b) G. Chaka, J. L. Sonnenberg, H. B. Schlegel, M. J. Heeg, G. Jaeger, T. J. Nelson, L. A. Ochrymowycz, D. B. Rorabacher, *J. Am. Chem. Soc.* **2007**, *129*, 5217-5227; (c) Q. Yu, C. A. Salhi, E. A. Ambundo, M. J. Heeg, L. A. Ochrymowycz, D. B. Rorabacher, *J. Am. Chem. Soc.* **2001**, *123*, 5720-5729.

8 (a) H. Doine, Y. Yano, T. W. Swaddle, *Inorg. Chem.* **1989**, *28*, 2319-2322; (b) K. Krylova, C. P. Kulatilleke, M. J. Heeg, C. A. Salhi, L. A. Ochrymowycz, D. B. Rorabacher, *Inorg. Chem.* **1999**, *38*, 4322-4328; (c) C. P. Kulatilleke, *Polyhedron* **2007**, *26*, 1166-1172; (d) M. A. Augustin, J. K. Yandell, *Inorg. Chem.* **1979**, *18*, 577-583.

9 L. Garcia, F. Cisnetti, N. Gillet, R. Guillot, M. Aumont-Nicaise, J.-P. Piquemal, M. Desmadril, F. Lambert, C. Policar, *J. Am. Chem. Soc.* **2015**, *137*, 1141-1146.

10 (a) M. Zhao, H.-B. Wang, L.-N. Ji, Z.-W. Mao, *Chem. Soc. Rev.* **2013**, *42*, 8360-8375; (b) A. S. Borovik, *Acc. Chem. Res.* **2005**, *38*, 54-61; (c) D. Natale, J. C. Mareque-Rivas, *Chem. Commun.* **2008**, 425-437; (d) Z. Thammavongsy, M. E. LeDoux, A. G. Breuhaus-Alvarez, T. Seda, L. N. Zakharov, J. D. Gilbertson, *Eur. J. Inorg. Chem.* **2013**, *2013*, 4008-4015; (e) E. M. Matson, Y. J. Park, A. R. Fout, *J. Am. Chem. Soc.* **2014**, *136*,

17398-17401; (f) K. J. Tubbs, A. L. Fuller, B. Bennett, A. M. Arif, L. M. Berreau, *Inorg. Chem.* **2003**, *42*, 4790-4791; (g) L. R. Widger, C. G. Davies, T. Yang, M. A. Siegler, O. Troeppner, G. N. L. Jameson, I. Ivanović-Burmazović, D. P. Goldberg, *J. Am. Chem. Soc.* **2014**, *136*, 2699-2702; (h) L. E. Cheruzel, M. R. Cecil, S. E. Edison, M. S. Mashuta, M. J. Baldwin, R. M. Buchanan, *Inorg. Chem.* **2006**, *45*, 3191-3202; (i) G. Feng, J. C. Mareque-Rivas, N. H. Williams, *Chem. Commun.* **2006**, 1845-1847; (j) R. L. Shook, A. S. Borovik, *Chem. Commun.* **2008**, 6095-6107; (k) A. Wada, Y. Honda, S. Yamaguchi, S. Nagatomo, T. Kitagawa, K. Jitsukawa, H. Masuda, *Inorg. Chem.* **2004**, *43*, 5725-5735; (l) L. M. Berreau, *Eur. J. Inorg. Chem.* **2006**, *2006*, 273-283; (m) M. Rakowski DuBois, D. L. DuBois, *Chem. Soc. Rev.* **2009**, *38*, 62-72; (n) J. S. Hart, G. S. Nichol, J. B. Love, *Dalton Trans.* **2012**, *41*, 5785-5788; (o) N. S. Sickerman, Y. J. Park, G. K. Y. Ng, J. E. Bates, M. Hilkert, J. W. Ziller, F. Furche, A. S. Borovik, *Dalton Trans.* **2012**, *41*, 4358-4364; (p) J. Rosenthal, D. G. Nocera, *Acc. Chem. Res.* **2007**, *40*, 543-553.

11 (a) C. M. Moore, N. K. Szymczak, *Chem. Commun.* **2013**, *49*, 400-402; (b) C. M. Moore, N. K. Szymczak, *Chem. Commun.* **2015**, *51*, 5490-5492; (c) C. M. Moore, N. K. Szymczak, *Chem. Sci.* **2015**, *6*, 3373-3377; (d) J. B. Geri, N. K. Szymczak, *J. Am. Chem. Soc.* **2015**, *137*, 12808-12814.

12 (a) I. Nieto, M. S. Livings, J. B. Sacci III, L. E. Reuther, M. Zeller, E. T. Papish, *Organometallics* **2011**, *30*, 6339-6342; (b) K.-i. Fujita, Y. Tanaka, M. Kobayashi, R. Yamaguchi, *J. Am. Chem. Soc.* **2014**, *136*, 4829-4832; (c) J. F. Hull, Y. Himeda, W.-H. Wang, B. Hashiguchi, R. Periana, D. J. Szalda, J. T. Muckerman, E. Fujita, *Nat. Chem.* **2012**, *4*, 383-388.

13 C. M. Moore, E. W. Dahl, N. K. Szymczak, *Curr. Opin. Chem. Biol.* **2015**, *25*, 9-17.

14 G. Aullón, D. Bellamy, A. Guy Orpen, L. Brammer, E. A. Bruton, *Chem. Commun.* **1998**, 653-654.

15 (a) C. M. Moore, D. A. Quist, J. W. Kampf, N. K. Szymczak, *Inorg. Chem.* **2014**, *53*, 3278-3280; (b) J. C. M. Rivas, S. L. Hinchley, L. Metteau, S. Parsons, *Dalton Trans.* **2006**, 2316-2322.

16 (a) J.-D. Cheon, T. Mutai, K. Araki, *Tetrahedron Lett.* **2006**, *47*, 5079-5082; (b) A. R. Petersen, R. A. Taylor, I. Vicente-Hernández, P. R. Mallender, H. Olley, A. J. P. White, G. J. P. Britovsek, *J. Am. Chem. Soc.* **2014**, *136*, 14089-14099; (c) R. A. Taylor, D. J. Law, G. J. Sunley, A. J. P. White, G. J. P. Britovsek, *Angew. Chem. Int. Ed.* **2009**, *48*, 5900-5903.

17 A. R. Petersen, R. A. Taylor, I. Vicente-Hernández, J. Heinzer, A. J. P. White, G. J. P. Britovsek, *Organometallics* **2014**, *33*, 1453-1461.

18 L. Yang, D. R. Powell, R. P. Houser, *Dalton Trans.* **2007**, 955-964.

19 R. R. Gagne, J. L. Allison, G. C. Lisensky, *Inorg. Chem.* **1978**, *17*, 3563-3571.

20 SP geometries about Cu(I) have also been observed in two multinuclear systems: P. L. Arnold, A. C. Scarisbrick, A. J. Blake, C. Wilson, *Chem. Commun.* **2001**, 2340–2341. and M. Shinoura, S. Kita, M. Ohba, H. Ōkawa, H. Furutachi, M. Suzuki, *Inorg. Chem.* **2000**, *39*, 4520–4526. Note that Jacobi has reported a complex that may be viewed as either 4-coordinate SP Cu(I) or as 5-coordinate, with a κ^2-carboxylate ligand (O-Cu = 2.56Å).: É. Balogh-Hergovich, J. Kaizer, G. Speier, G. Huttner, A. Jacobi, *Inorg. Chem.* **2000**, *39*, 4224–4229.

21 L. Brammer, E. A. Bruton, P. Sherwood, *Crystal Growth & Design* **2001**, *1*, 277-290.

22 P. Hobza, K. Müller-Dethlefs, *Non-covalent Interactions*, Royal Society of Chemistry, Cambridge, **2010**.

23 J. W. Steed, J. L. Atwood, *Supramolecular Chemistry*, 2 ed., John Wiley & Sons, Ltd., West Sussex, **2009**.

24 P. J. Chirik, K. Wieghardt, *Science* **2010**, *327*, 794-795.

25 C. C. Scarborough, K. M. Lancaster, S. DeBeer, T. Weyhermüller, S. Sproules, K. Wieghardt, *Inorg. Chem.* **2012**, *51*, 3718-3732.

26 (a) J. F. Moulder, W. F. Stickle, P. E. Sobol, K. D. Bomben in *Handbook of X-Ray Photoelectron Spectroscopy*, (Ed: J. Chastain), Perkin-Elmer Corp., Phys. Electron. Div, Eden Prairie, MN, **1992**, pp. 86-87; (b) D. C. Frost, A. Ishitani, C. A. McDowell, *Mol. Phys.* **1972**, 24, 861-877; (c) A. K. Hui, Y. Losovyj, R. L. Lord, K. G. Caulton, *Inorg. Chem.* **2014**, *53*, 3039-3047.

27 Geometry optimizations performed on the crystal structure of **1** and subsequent stability calculations using spin-unrestricted functionals show the Cu(I) closed-shell singlet state to be an energy minimum. (See SI)

28 A. V. Iogansen, G. A. Kurkchi, V. M. Furman, V. P. Glazunov, S. E. Odinokov, *Zh. Prikl. Spektrosk.* **1980**, *33*, 460.

29 Note that under the identical conditions, ferrocene behaves similar to 1.

30 Due to the nearly diffusion-controlled ligand substitution rates typical of Cu(II) complexes, coordination number invariance is not required to access fast ET rates. For examples, see reference 8. The analogous ET self exchange experiment was not possible with **5**, due to its facile disproportionation at room temperature and irreversible $Cu^{II/I}$ reduction.

31 E. J. Pulliam, D. R. McMillin, *Inorg. Chem.* **1984**, *23*, 1172-1175.

32 L. Lochmann, J. Pospíšil, D. Lím, *Tetrahedron Lett.* **1966**, 257.

33 N. G. Connelly, W. E. Geiger, *Chem. Rev.* **1996**, *96*, 877–910.

34 M. J. Frisch, G. W. Trucks, H. B. Schlegel, G. E. Scuseria, M. A. Robb, J. R. Cheeseman, G. Scalmani, V. Barone, B. Mennucci, G. A. Petersson, H. Nakatsuji, M. Caricato, X. Li, H. P. Hratchian, A. F. Izmaylov, J. Bloino, G. Zheng, J. L. Sonnenberg, M. Hada, M. Ehara, K. Toyota, R. Fukuda, J. Hasegawa, M. Ishida, T. Nakajima, Y. Honda, O. Kitao, H. Nakai, T. Vreven, J. A. Montgomery, Jr., J. E. Peralta, F. Ogliaro, M. Bearpark, J. J. Heyd, E. Brothers, K. N. Kudin, V. N. Staroverov, R. Kobayashi, J. Normand, K. Raghavachari, A. Rendell, J. C. Burant, S. S. Iyengar, J. Tomasi, M. Cossi, N. Rega, J. M. Millam, M. Klene, J. E. Knox, J. B. Cross, V. Bakken, C. Adamo, J. Jaramillo, R. Gomperts, R. E. Stratmann, O. Yazyev, A. J. Austin, R. Cammi, C. Pomelli, J. W. Ochterski, R. L. Martin, K. Morokuma, V. G. Zakrzewski, G. A. Voth, P. Salvador, J. J. Dannenberg, S. Dapprich, A. D. Daniels, Ö. Farkas, J. B. Foresman, J. V. Ortiz, J. Cioslowski, and D. J. Fox, Gaussian 09, Revision D.01; Gaussian, Inc., Wallingford CT, 2009.

35 R. Ditchfield, W. J. Hehre, and J. A. Pople, *J. Chem. Phys.* **1971**, *54*, 724.

36 F. Weigend, R. Ahlrichs, Phys. Chem. Chem. Phys. **2005**, *7*, 3297.

37 C. Lee, W. Yang, and R. G. Parr, *Phys. Rev. B*, **1988**, *37*, 785-789.

38 Y. Zhao and D. G. Truhlar, *J. Chem. Phys.* **2006**, *125*, 194101.

39 Y. Zhao and D. G. Truhlar, *Theor. Chem. Acc.* **2008**, *120*, 215-241.

40 J.-D. Chai, M. Head-Gordon, *Phys. Chem. Chem. Phys.* **2008**, *10*, 6615.

41 A. Jesser, M. Rohrmüller, W. G. Schmidt, S. Herres-Pawlis, *J. Comput. Chem.* **2013**, *35*, 1–17.

42 CrystalClear Expert 2.0 r12, Rigaku Americas and Rigaku Corporation (2011), Rigaku Americas, 9009, TX, USA 77381-5209, Rigaku Tokyo, 196-8666, Japan.

43 O. V. Dolomanov, L. J. Bourhis, R. J. Gildea, J. A. K. Howard and H. Puschmann. *J. Appl. Cryst.* **2009**, 42, 339-341.

44 G. M Sheldrick, *Acta Cryst. A64***, 2008**, 112-122.

45 A. L. Spek, *J. Appl. Cryst.* **2003**, *36*, 7-13.

Chapter 4: Hydrogen bond stabilized Cu and Zn peroxides

Portions of this chapter have been published:

Dahl, E. W.; Dong, H. T.; Szymczak, N. K.; Phenylamino Derivatives of Tris(2-pyridylmethyl)amine: Hydrogen-Bonded Peroxodicopper Complexes. *Chem. Commun.* **2018**. DOI: 10.1039/c7cc08619a.

4.1 Motivation for studying H-bonding to Cu-O_2

Copper-containing oxygenase and oxidase enzymes are an important class of metalloenzymes whose diverse O_2 activation pathways facilitate a wide variety of biological functions.[1] Although challenging to study in the native enzymes, the study of O_2 binding and activation by copper within easily modifiable synthetic systems has greatly expanded our understanding of these metalloenzymes,[2] and the first crystallized Cu-O_2 adduct was the (*trans*-1,2-peroxo)dicopper complex of the tris(2-pyridylmethyl)amine (tpa) ligand (Figure 4-1).[3] In the nearly 30 years since that structure, modifications to tpa and similar ligand frameworks have been targeted to elucidate the key factors responsible for O_2 binding and activation. Although critical to the function of many metalloenzymes,[4] the impact of secondary coordination sphere hydrogen bonding (H-bonding) interactions on copper-oxygen species is not well understood.[5] For example, H-bonding interactions have been demonstrated to either stabilize[6] or destabilize[7] Cu-O_2(H) adducts. For this reason, synthetic systems bearing tunable second sphere H-bonding groups provide a facile means to study their influence on Cu-O_2 binding and activation.

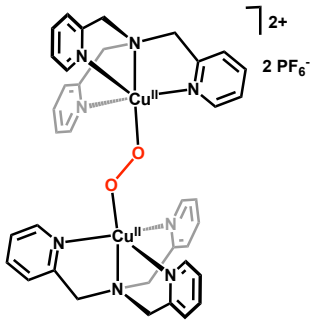

Figure 4-1: Structure of the first crystallographically characterized (*trans*-1,2-peroxo)dicopper complex $[Cu_2(tpa)_2O_2](PF_6)_2$.

4.2 Phenylamino-derived tpa ligands

Szymczak and coworkers recently introduced the tris(6-hydroxyl-2-pyridylmethyl)amine (H_3thpa) ligand that incorporates three –OH groups within the secondary sphere of tpa.[8] The pendent –OH groups are potent H-bond donors to metal-coordinated substrates and facilitate proton and electron transfer reactions.[9] However, these complexes underwent facile formation of dinuclear copper species in the presence of weak bases, which limited investigations of subsequent reactivity. To overcome this limitation, we targeted pendent phenylamino groups as less acidic, sterically protected H-bond donors (Figure 4-2).[10] In contrast to previously reported –NHCO^{t}Bu substituted tpa variants, the phenylamino group provides both steric and electronic flexibility that allows them to act as highly tunable H-bond donors. We present a series of aniline-appended tripodal ligands that feature highly directed H-bonding interactions of varied strength and highlight the design concept by demonstrating H-bond dictated O_2 reactivity.

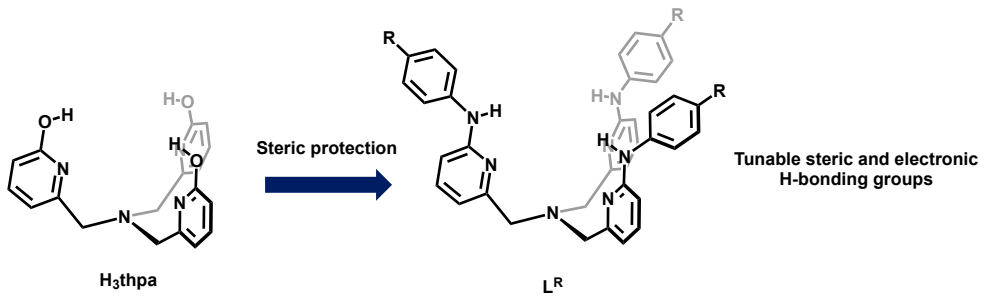

Figure 4-2: Transition from OH-based ligand to NHPh-based ligand for added steric and electronic tunability.

4.3 Characterization of H-bonded copper chloride complexes

The ligand tris(6-phenylamino-2-pyridylmethyl)amine (L^H) was prepared via a Buchwald-Hartwig coupling of tris(6-bromo-2-pyridylmethyl)amine (Br_3tpa) with aniline, $Pd(OAc)_2$, and *rac*-BINAP. The addition of CuCl to L^H in THF afforded the yellow complex Cu(L^H)Cl (**1^H**) in 59% yield after 48 h. A crystal of **1^H** suitable for X-ray diffraction was grown by layering pentane over a concentrated toluene solution at -30°C (Figure 4-3). The solid-state structure revealed C_3-symmetry with directed H-bonds from the pendent –NHPh units to the Cl ligand (N–Cl: 3.311(4) Å). These H-bonds are significantly longer than the previous Cu(H_3thpa)Cl complex bearing pendent –OH groups (N_{avg}–Cl: 3.048 Å) consistent with weaker H-bond interactions.[8] In addition, the Cu–N_{axial} and Cu–Cl bonds in **1^H**, at 2.252(4) Å and 2.3398(14) Å respectively, are shortened compared to Cu(H_3thpa)Cl (2.283(2) Å and 2.5661(6) Å respectively). Overall, the phenylamino groups in **1^H** provide a sterically protected pocket for the Cl ligand while allowing for further electronic tuning by modifying the identity of the aniline.

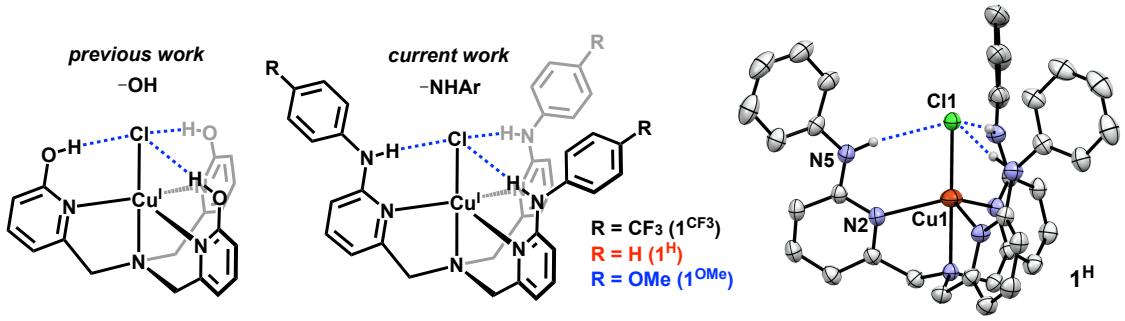

Figure 4-3: Structure of Cu(H_3thpa)Cl and $\mathbf{1}^{\mathbf{R}}$ (R = CF_3, H, or OMe) and X-ray crystal structure of $\mathbf{1}^{\mathbf{H}}$ (30% ellipsoids, H atoms not involved in H-bonding omitted for clarity).

4.4 Tuning the redox potential with para-substitutions

Two ligand derivatives featuring electronically distinct, yet sterically similar H-bond donors were prepared. 4-Trifluoromethylaniline and 4-methoxyaniline afforded ligands L^{CF3} and L^{OMe} respectively, which were metalated with CuCl to provide Cu(L^{CF3})Cl ($\mathbf{1}^{\mathbf{CF3}}$) and Cu($L^{OMe}$)Cl ($\mathbf{1}^{\mathbf{OMe}}$). The electronic influence of each ligand variant was interrogated by analysis of the $Cu^{I/II}$ redox couple (Figure 4-4). Complex $\mathbf{1}^{\mathbf{H}}$ exhibits a reversible $Cu^{I/II}$ redox couple at -470 mV vs Fc (CH_2Cl_2; 0.1 M NBu_4PF_6). This value is shifted to more negative potentials relative to the –OH complex Cu(H_3thpa)Cl (-365 mV vs Fc), consistent with increased electron releasing properties of L^H than H_3thpa. The $Cu^{I/II}$ redox couple in $\mathbf{1}^{\mathbf{OMe}}$ features the most reducing Cu center at -510 mV vs Fc. The electronically deficient $\mathbf{1}^{\mathbf{CF3}}$, however, exhibits a $Cu^{I/II}$ redox couple at -350 mV vs Fc, which highlights the electronic tunability of the L^R ligands with simple substitution on the parent aniline. To contextualize these electrochemically obtained values with a well-defined metric, the potential difference of $\mathbf{1}^{\mathbf{CF3}}$ (120 mV) and $\mathbf{1}^{\mathbf{OMe}}$ (-40 mV) from the parent aniline ($\mathbf{1}^{\mathbf{H}}$) were plotted against Hammett values (*p*-substitution) of 0.54 and -0.27 respectively (Figure 4-4). The electrochemical shifts show a good correlation (R^2 = 0.98)

with these Hammett values, indicating that they may be used to provide a predictive measure ligand field effects within the tpa scaffold.

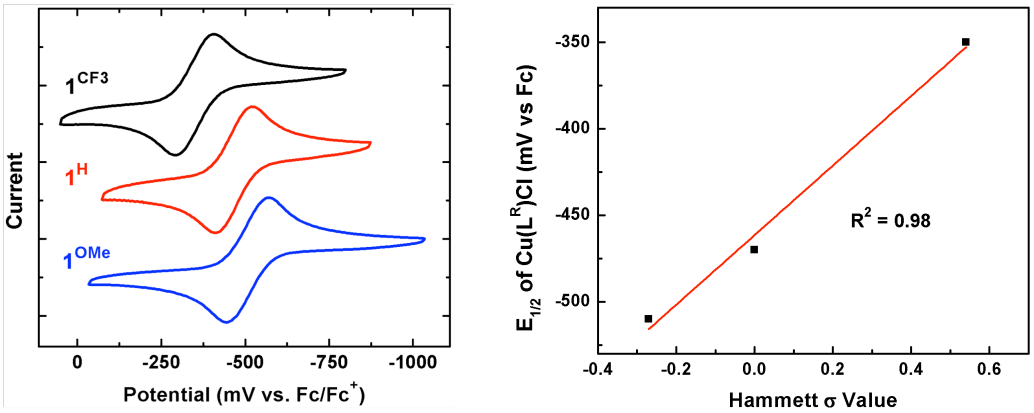

Figure 4-4: Cyclic voltammetry of $\mathbf{1}^{\mathbf{H}}$, $\mathbf{1}^{\mathbf{CF3}}$ and $\mathbf{1}^{\mathbf{OMe}}$ (left, 0.1 M NBu_4PF_6 CH_2Cl_2). Plot of the $E_{1/2}$ compared to the Hammett values of *p*-CF_3, *p*-H, and *p*-OMe (right).

4.5 Spectroscopic characterization of Cu(L^R)Cl complexes

The electronic variability in the L^R ligand series was also evident by ^{1}H NMR and IR spectroscopy. All three complexes are C_3-symmetric by ^{1}H NMR spectroscopy (CD_2Cl_2) and show a significantly downfield shifted –NH resonance consistent with H-bonding interactions between the –NH and the Cl ligand. The –NH peak appears at δ=9.88 in $\mathbf{1}^{\mathbf{H}}$ whereas it shifts downfield (δ=10.17) in $\mathbf{1}^{\mathbf{CF3}}$ and upfield (δ=9.72) in $\mathbf{1}^{\mathbf{OMe}}$. The magnitude of the two shifts, +0.29 and -0.16 respectively, are again consistent with the expected proportion based on Hammett parameters (R^2 = 0.99). The weakening of the –NH bond upon H-bonding is also evident by infrared spectroscopy (CH_2Cl_2) where the –NH stretching frequency shifts from 3431 cm^{-1} for L^H to 3223 cm^{-1} in $\mathbf{1}^{\mathbf{H}}$ (Figure 4-5). However, the value of the –NH stretch for $\mathbf{1}^{\mathbf{CF3}}$ and $\mathbf{1}^{\mathbf{OMe}}$ does correlate directly with the Hammett value. The –NH stretch in $\mathbf{1}^{\mathbf{OMe}}$ shifts to lower energy (3220 cm^{-1}) consistent with a stronger H-bond interaction, while the –NH stretch in $\mathbf{1}^{\mathbf{CF3}}$

falls between $\mathbf{1^H}$ and $\mathbf{1^{OMe}}$ at 3221 cm^{-1}. The IR data demonstrate the difficulty of assigning trends in a complex system where electronic character of the metal and M-X unit is highly coupled to both H-bond donor strength and H-bond acceptor strength.

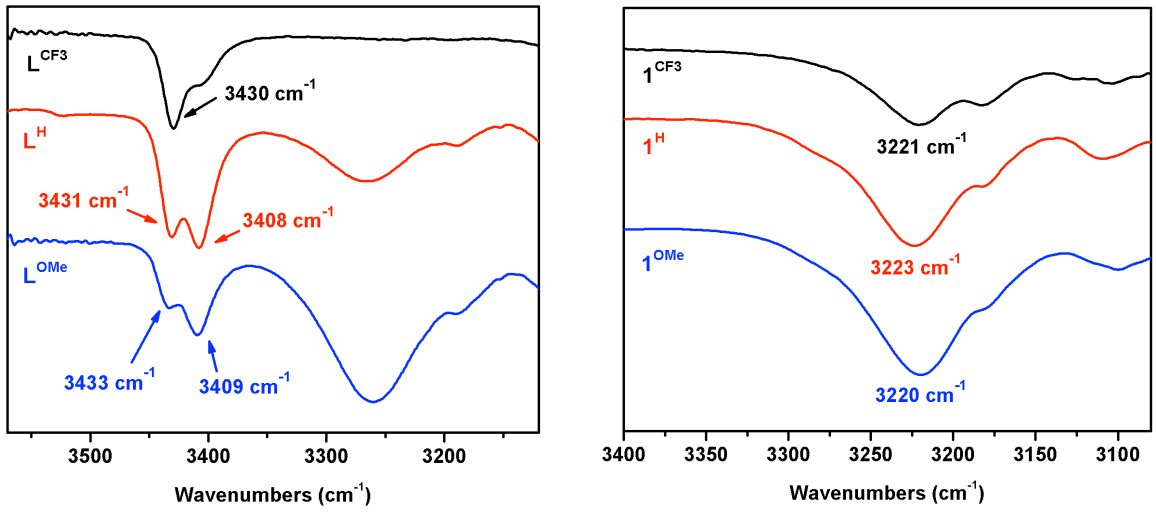

Figure 4-5: IR overlay of L^{CF3}, L^H, and L^{OMe} in CH_2Cl_2 (left). IR overlay of $\mathbf{1^{CF3}}$, $\mathbf{1^H}$, and $\mathbf{1^{OMe}}$ in CH_2Cl_2 (right).

4.6 H-bonded (*trans*-1,2-peroxo)dicopper complexes

4.6.1 Synthesis of $[Cu_2(L^H)_2O_2](BAr')_2$

The –NHPh appended tpa derivatives provide a tunable framework for studying O_2 binding to Cu and the resulting H-bonded (*trans*-1,2-peroxo)dicopper complexes. The complex $[Cu^I(L^H)]BAr'$ (BAr'= $[B(C_6F_5)_4]^-$) was prepared by mixing L^H and $Cu(MeCN)_4BAr'$ in CH_2Cl_2 under an inert atmosphere. ^1H NMR spectroscopy was used to verify formation of a C_3-symmetric Cu(I) complex. Cooling a CH_2Cl_2 solution of $[Cu^I(L^H)]BAr'$ to -70°C and introducing dry O_2 afforded the (*trans*-1,2-peroxo)dicopper complex $[(Cu(L^H))_2(O_2)][BAr']_2$ ($\mathbf{2^H}$, Figure 4-6). The reaction was confirmed by a color change in solution (colorless to brown) and the

appearance of a band at 457 nm (ε= 3000 $M^{-1}cm^{-1}$) in the electronic absorption spectrum, assigned as the oxygen to copper ligand-to-metal charge transfer (LMCT) band. This contrasts with the unsubstituted complex $[(Cu(tpa))_2(O_2)][PF_6]_2$ which exhibits a primary LMCT band at 525 nm (ε= 11500 $M^{-1}cm^{-1}$) and a shoulder at 590 nm (ε= 7600 $M^{-1}cm^{-1}$).[3] In **2^{H}** we propose that the π* orbitals on the peroxide unit that engage the Cu center lose electron density through the directed H-bonding interactions. This effect weakens the Cu–O covalency and results in a hypsochromic shift of the LMCT (*vida infra*). Furthermore, the hypochromic shift and loss of the shoulder band in **2^{H}** was also observed by Masuda and co-workers in a similar H-bonded system and was postulated to be due to decreased rotational freedom of the peroxo unit.[5f] Complex **2^{H}** was subjected to additional spectroscopic characterization.[11] The EPR (X-band) spectrum for **2^{H}** is silent, consistent with other S=1 integer spin (*trans*-1,2-peroxo)dicopper complexes. Upon warming to room temperature, solutions of **2^{H}** convert to a green, EPR active species, suggesting decomposition to monomeric Cu(II) byproducts. The UV-Vis and EPR data were corroborated by solid-state characterization of **2^{H}**.

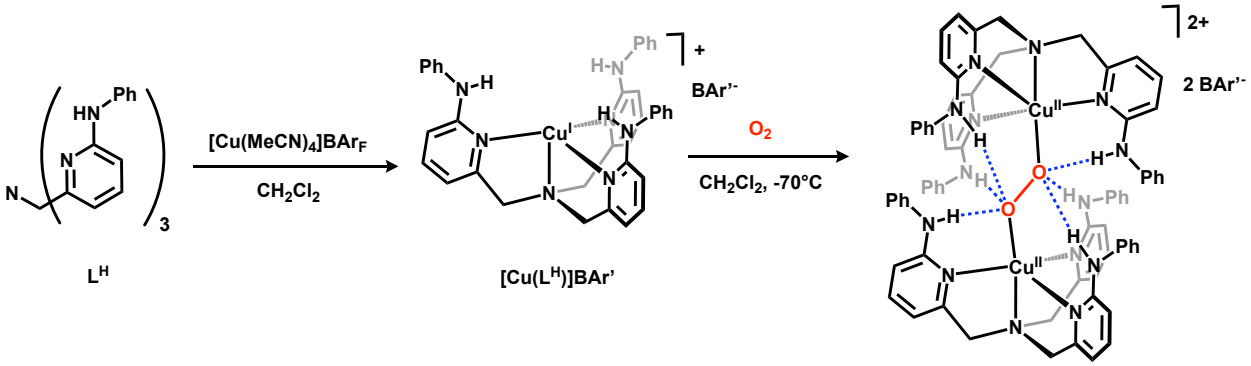

Figure 4-6: Synthesis of [Cu(L^{H})]BAr' and **2^{H}**.

The 68 nm shift of the primary O to Cu LMCT can be rationalized by considering the molecular orbitals involved in peroxo binding to copper (Figure 4-7). Of the two filled π* orbitals on peroxide only one (π_σ*) is capable of directly engaging with the Cu d_{z^2} orbitals. This results in a lower energy bonding orbital with mostly π_σ* character and a higher energy non-bonding orbital with mostly π_v* character. The excitation of an electron from the lower energy orbital to the Cu d_{z^2} LUMO generates the higher energy LMCT with greater molar absorptivity. In the parent $[(Cu(tpa))_2(O_2)][PF_6]_2$ complex this is the transition observed at 525 nm (Figure 4-7, purple arrow). The shoulder band at 590 nm in the UV-Vis spectrum of $[(Cu(tpa))_2(O_2)][PF_6]_2$ is therefore the transition from the non-bonding π_v* orbital and a consequence of peroxide rotation allowing favorable overlap with the LUMO. In $\mathbf{2^H}$, the –NHPh groups directly engage and stabilize the peroxide π* orbitals through H-bonding interactions and lower their relative energy. As a result, the energy required for an O to Cu charge transition increases leading to the 68 nm hypsochromic shift of the LMCT (Figure 4-7, yellow arrow). A lower energy shoulder band is not observed in the $\mathbf{2^H}$ UV-Vis spectrum (Figure 4-7, dotted yellow arrow) most likely due to decreased rotational freedom about the peroxide from the H-bonding interactions.[5f]

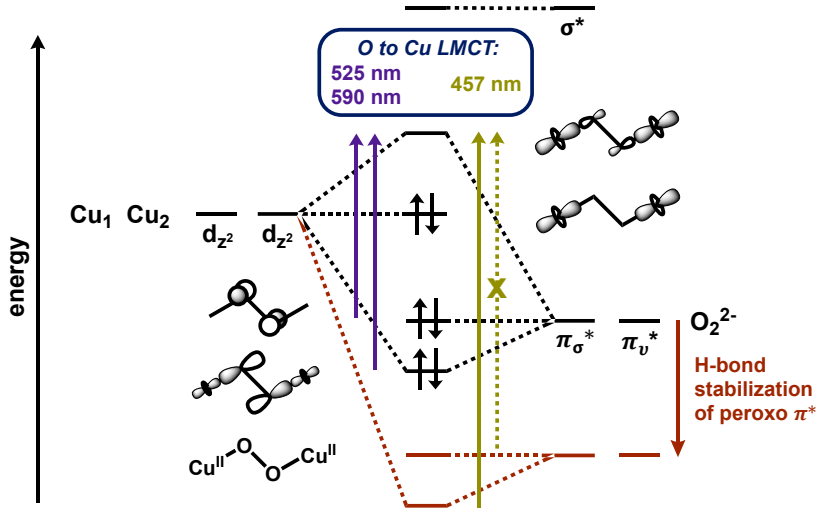

Figure 4-7: Molecular orbital diagram of the Cu–O bonding of (trans-1,2-peroxo)dicopper complexes (shown in black) and the effect of H-bonding interactions to the peroxide (shown in red). Diagram was recreated and modified from reference 2e.

4.6.2 Solid-state structure of $[(Cu(L^H))_2(O_2)][BAr'_]_2$

A crystal of $\mathbf{2^H}$ suitable for X-ray diffraction was grown in CH_2Cl_2 in a -80° freezer under an atmosphere of oxygen over 3 days (Figure 4-8), constituting the first crystallographically characterized H-bonded (*trans*-1,2-peroxo)dicopper complex. For each 'Cu(L^H)' in $\mathbf{2^H}$ only one –NHPh group engages in H-bonding with the proximal oxygen of the peroxo unit (N5–O1: 2.723(7) Å) while the other two –NHPh groups engage the distal oxygen (N6–O2: 2.859(7) Å and N7–O2: 2.851(7) Å). Previous examples of H-bonded Cu-O_2 species have shown that H-bonding to the proximal oxygen generally increases stability of the species while H-bonding to the distal oxygen decreases stability.[5g] $\mathbf{2^H}$ contains both proximal and distal H-bonds and stable in solution at -70°C for at least 8 hours, consistent with a net stabilizing effect to the O–O unit. The weakening of the Cu–O bond covalency in $\mathbf{2^H}$, observed by UV-Vis, was also corroborated by the solid-state data. The Cu–O bond at 1.902(3) Å is elongated compared to the unsubstituted complex $[(Cu(tpa))_2(O_2)][PF_6]_2$ (1.852(4) Å). The O–O bond in $\mathbf{2^H}$ (1.477(5) Å) is also elongated

compared to the parent tpa complex (1.433(9) Å). Although the O–O bond might be expected to shorten as a result of H-bonding interactions with the peroxide π* orbital,[5e, 5f] additional structural factors may be responsible for the bond elongation. The steric profile provided by the –NHPh groups on L^H limit the possible interatomic distance between Cu centers. The Cu···Cu distance in $\mathbf{2^H}$ (4.691(1) Å) is 0.3 Å longer than that observed for $[(Cu(tpa))_2(O_2)][PF_6]_2$ (4.358(3) Å). Despite these steric considerations, stability may also be augmented by π-π interactions between the pendent –NHPh groups and the opposing pyridine rings (π-π distance: 3.4-3.6 Å).

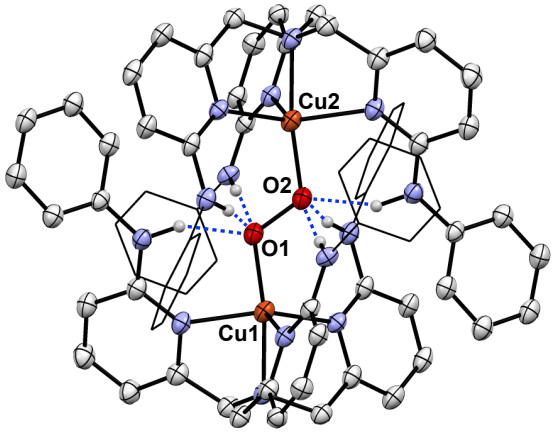

Figure 4-8: X-ray crystal structure of $\mathbf{2^H}$ (30% ellipsoids, H atoms not involved in H-bonding omitted for clarity).

4.6.3 Electronic tuning of H-bonded dicopper peroxos

The electronic tuning provided by L^{CF3} and L^{OMe} regulates the energy of the O to Cu LMCT. $[Cu(L^{CF3})]BAr'$ and $[Cu(L^{OMe})]BAr'$ readily bind O_2 at -70°C to form the analogous (*trans*-1,2-peroxo)dicopper complexes $[(Cu(L^{CF3}))_2(O_2)][BAr']_2$ ($\mathbf{2^{CF3}}$) and $[(Cu(L^{OMe}))_2(O_2)][BAr']_2$ ($\mathbf{2^{OMe}}$). While the series of complexes ($\mathbf{2^R}$) are all brown in solution,

the LMCT band shifts as a function of the electronic character at the metal (Figure 4-9).[12] $\mathbf{2}^{\mathbf{CF3}}$ features a 7 nm hypsochromic shift of the LMCT, while, $\mathbf{2}^{\mathbf{OMe}}$ features a 3 nm bathochromic shift from the parent $\mathbf{2}^{\mathbf{H}}$. The observed shifting of the LMCT contrasts with previously reported substituted tpa ligands, where the addition of 4-OMe groups to the pyridine backbone had *no* effect on the LMCT.[13] In $\mathbf{2}^{\mathbf{R}}$, the shift of the LMCT bands is in accordance with the ligands' respective electronic (Hammett) parameter ($R^2 = 0.99$, Figure 4-8) and may be a product of both the Cu effective charge *and* H-bond donor strength.

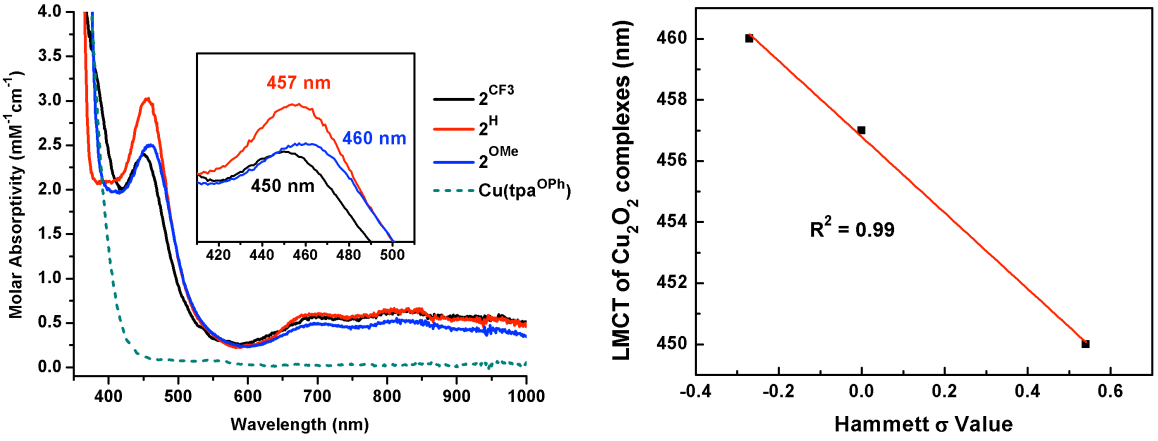

Figure 4-9: UV-Vis overlay of $\mathbf{2}^{\mathbf{R}}$ (1:1 CH_2Cl_2:acetone at -70°C) and the reaction of [Cu(tpa^{OPh})]BAr' with O_2 at -70°C (left). Plot of the O to Cu LMCT band in $\mathbf{2}^{\mathbf{R}}$ compared to the Hammett values of *p*-CF3, *p*-H, and *p*-OMe (right).

For both the previous substituted tpa copper peroxos and the substituted H-bonded $\mathbf{2}^{\mathbf{R}}$ complexes, electron donating substituents decrease the effective charge on copper which would destabilize the copper orbitals. The increased electron density on copper also attenuates the Cu–O bond and concentrates more electron density on the peroxo unit destabilizing the peroxo orbitals as well (Figure 4-10). This explains why the previously reported 4-substituted $[(Cu(tpa^{R}))_2(O_2)]^{2+}$ complexes did not show any change in the O to Cu LMCT energy when

substituted with three 4-OMe groups and only a bathochromic shift of 3 nm when substituted with three 4-NMe_2 groups. The 3 nm bathochromic shift of the LMCT observed for $\mathbf{2}^{\mathbf{OMe}}$ from $\mathbf{2}^{\mathbf{H}}$ must therefore be due to the H-bonding component of the complexes. The –NH groups on L^{OMe} have a higher pKa compared to L^{H} and would serve as weaker H-bond donors. Six weakened H-bonds to peroxide in $\mathbf{2}^{\mathbf{OMe}}$ would result in additional electron density on the peroxo unit and further destabilization of the peroxide orbitals. The net effect of peroxo orbital destabilization from the copper effective charge and H-bond donor strength would be a bathochromic shift of the LMCT. Since both Cu effective charge and H-bond donor pKa are correlated with *p*-substituted Hammett constants, the hypsochromic shift of 7 nm for the $\mathbf{2}^{\mathbf{CF3}}$ LMCT can also be rationalized using the opposite assumptions for electron withdrawing trifluoromethyl groups.

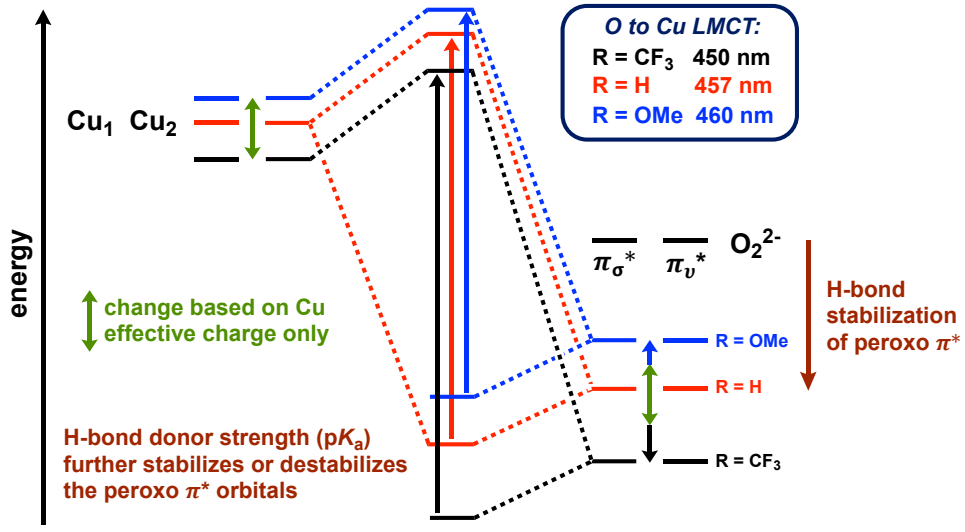

Figure 4-10: Molecular orbital diagrams for $\mathbf{2}^{\mathbf{R}}$ showing how copper effective charge and H-bond donor strength effect the O to Cu LMCT band.

The oxidation potential of the halide-free $[Cu^{I}(L^{R})]BAr'$ complexes, obtained by square-wave voltammetry, provided an additional description of the electronic character at Cu. $[Cu(L^{H})]BAr'$ in MeCN (0.1M NBu_4PF_6) exhibits an irreversible oxidation event at +110 mV vs Fc. The associated L^{CF3} and L^{OMe} Cu(I) complexes feature redox potentials shifted by +90 mV and -20 mV from L^{H}, respectively (Figure 4-11). Importantly, these values are significantly more positive than $[Cu(tpa)]PF_6$ (-400 mV vs Fc). O_2 binding to $[Cu(L^{CF3})]BAr'$ at potentials as high as +200 mV vs Fc contrasts with most known Cu(I)-tpa variants that exhibit diminished O_2 reactivity at more positive potentials.[14] These data indicate that the Cu(I) centers in $[Cu(L^{R})]BAr'$ are only modestly reducing and might be anticipated to engage in very weak binding to O_2. To account for the facile O_2 reactivity, we propose that the H-bonding groups on L^{R} provide additional stabilizing interactions for O_2 binding.

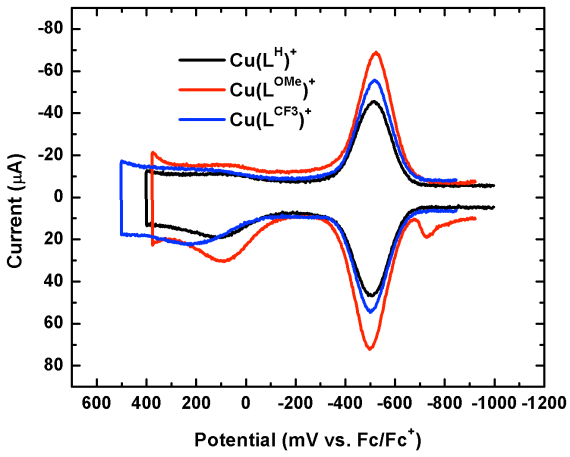

Figure 4-11: Square wave voltammogram of $[Cu(L^{R})]BAr'$ (R=H, CF_3 and OMe) in 0.1M NBu_4PF_6 MeCN with Fc* as internal reference (Fc^*/Fc^{*+} = -510 mV vs Fc/Fc^{+})

4.7 Determining the role of H-bonding

A sterically identical ligand to L^H with no H-bond donors was prepared in order to determine the role of H-bonding on the formation of the (*trans*-1,2-peroxo)dicopper complexes. The ligand tris(6-phenoxy-2-pyridylmethyl)amine (tpa^{OPh}) containing pendent phenylether groups was prepared via an Ullmann coupling of phenol and Br_3tpa. When tpa^{OPh} and $Cu(MeCN)_4BAr'$ were dissolved in CH_2Cl_2 and cooled to -70°C the resulting complex $[Cu(tpa^{OPh})]BAr'$ did not react with O_2 (Figure 4-12). ^1H NMR spectra of $[Cu(L^H)]BAr'$ and $[Cu(tpa^{OPh})]BAr'$ in CD_2Cl_2 revealed an almost identical chemical shift of the methylene protons, at δ=4.07 and 4.05 respectively, consistent with a similar electronic environment at copper.[15] ^1H NMR spectra of $[Cu(L^H)]BAr'$ and $[Cu(tpa^{OPh})]BAr'$ exhibit C_3-symmetry at both 25°C and -80°C, however, at -80°C the methylene proton peak on $[Cu(tpa^{OPh})]BAr'$ broadens by 16.8 Hz, consistent with a fluxional process (Figure 4-13 and 4-14). This observation of dynamic ligand binding may further contribute to the lack of O_2 reactivity with tpa^{OPh}.[16] Although steric and electronic properties of $[Cu(L^R)]BAr'$ would suggest that formation of $\mathbf{2^R}$ is unfavorable, these hindrances were overcome by introducing favorable hydrogen bonding interactions.

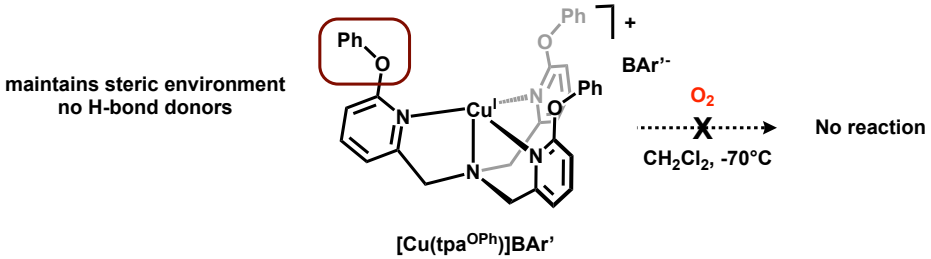

Figure 4-12: Structure of [Cu(tpaOPh)]BAr' and lack of reactivity toward O_2.

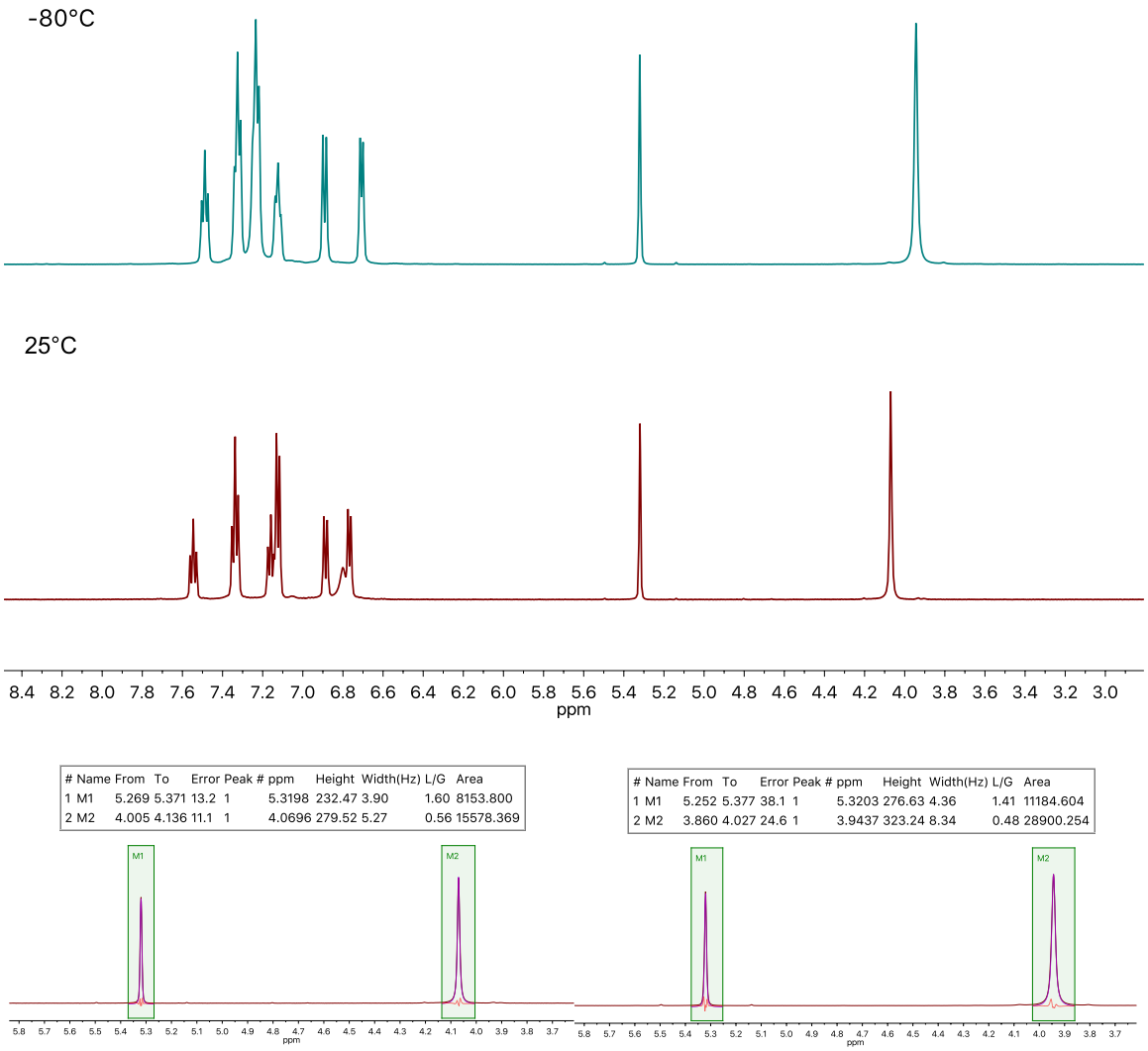

Figure 4-13: Top – Overlay of 500 MHz ^{1}H NMR spectra of [Cu(L^{H})]BAr' at 25°C and -80°C. Bottom – Line fitting for CD_2Cl_2 residual peak and methylene proton peak at 25°C (left) and -80°C (right). Reported peak broadening (Δfwhm) was corrected by subtracting the broadening observed for the residual solvent peak (0.46 Hz).

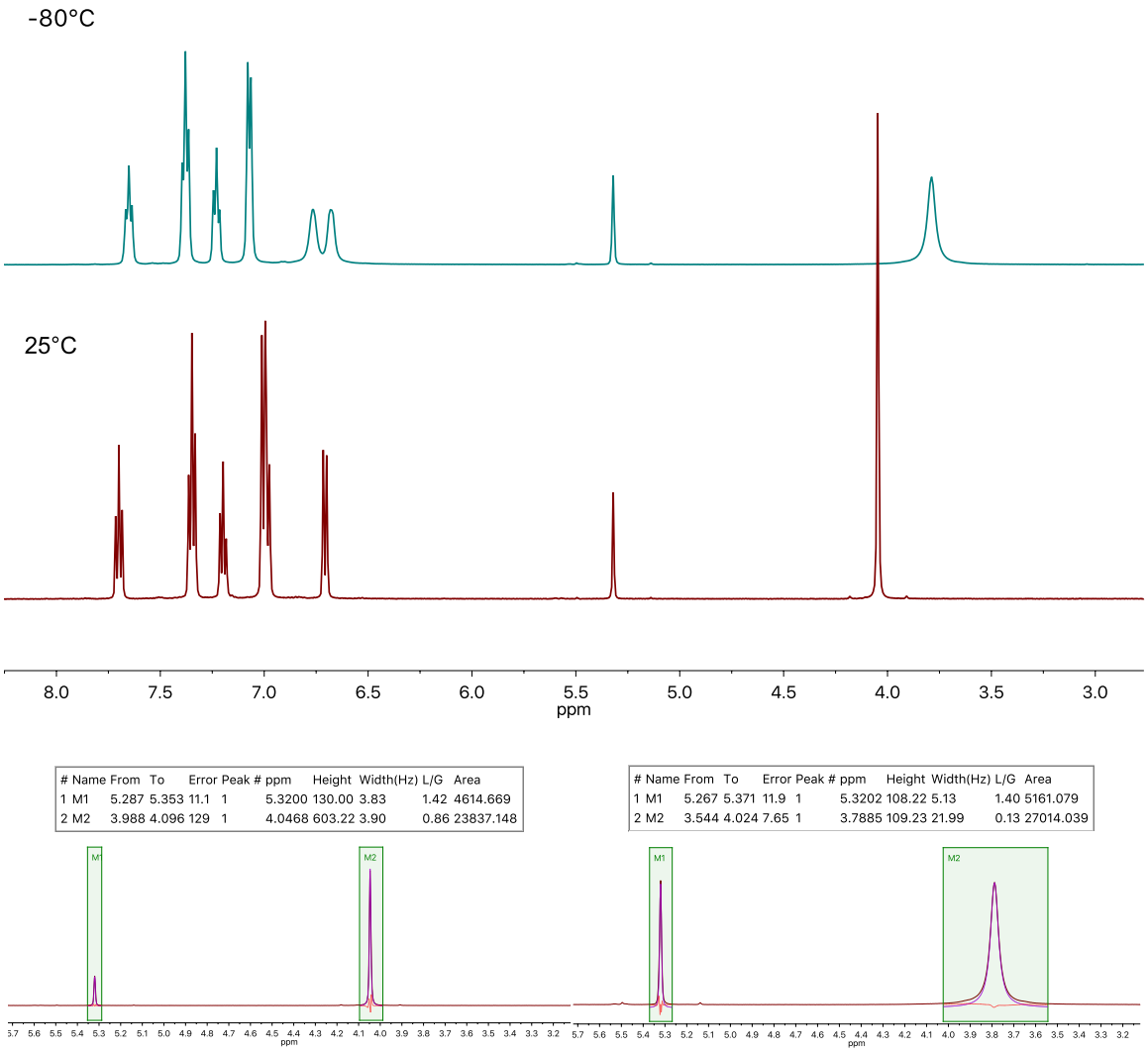

Figure 4-14: Top – Overlay of 500 MHz ^{1}H NMR spectra of [Cu(tpa^{OPh})]BAr' at 25°C and -80°C. Bottom – Line fitting for CD_2Cl_2 residual peak and methylene proton peak at 25°C (left) and -80°C (right). Reported peak broadening (Δfwhm) was corrected by subtracting the broadening observed for the residual solvent peak (1.3 Hz).

In conclusion, we have introduced a new variation on the tpa framework that incorporates highly tunable –NHPh groups in the secondary sphere. These groups act as H-bond donors while providing steric protection that can be used to isolate H-bonded Cu^{I}Cl complexes. Cu(I)

complexes bearing the new ligands react with O_2 to form H-bonded (*trans*-1,2-peroxo)dicopper complexes whose spectroscopic characteristics are dictated by the ligand electronics.

4.8 H-bonded (*trans*-1,2-peroxo)dizinc complexes

4.8.1 Introduction to H-bonded peroxides

The observed weakening of the Cu–O bond in $\mathbf{2^R}$ suggests that its stability is a result of H-bonding interactions between the –NHPh groups and the peroxide unit. In this regard, Nocera, Cummins and co-workers previously demonstrated the stabilization of a peroxide ion using only H-bonding interactions (Figure 4-15, left).[17] They reported that the peroxide ion was captured within a cryptand-type macrocycle by six directed H-bonds and could be obtained through O_2 reduction by cobaltocene. In $\mathbf{2^R}$, the Cu(I) center must first template the tpa ligand in C_3-symmetry and then reduce O_2 to peroxide. We hypothesized that if the six H-bonds to peroxide in $\mathbf{2^R}$ were responsible for a majority of its stability then the templating metal and the reductant could be separated. Zn(II) was chosen as a redox-inactive metal center that closely resembles Cu(II) in both charge and ionic radius; however, peroxides of Zn are exceedingly rare with only one report of alkylperoxo complexes (Figure 4-15, right).[18] Herein we use the H-bond donating $\mathbf{L^R}$ ligand to stabilize the first (*trans*-1,2-peroxo)dizinc complexes.

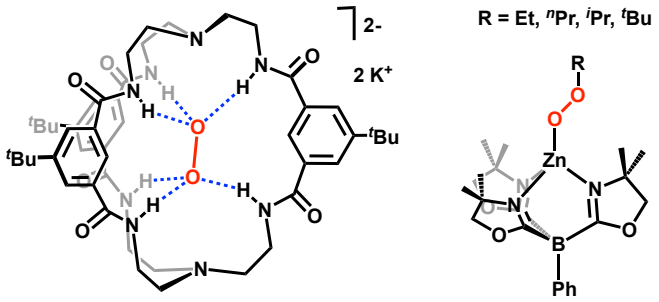

Figure 4-15: Example of a H-bond stabilized peroxide ion by a cryptand-type macrocycle (left) and the only crystallized Zn peroxide complexes (right).

4.8.2 Synthesis and structure of a dizinc peroxide

A room temperature stable dizinc peroxide was obtained from either O_2 and an exogenous reductant or H_2O_2 and base. First, the ligand L^H and $Zn(OTf)_2$ react at room temperature to form the intermediate species $Zn(L^H)(OTf)_2$. Although C_3-symmetric by ^1H NMR, universally broadened peaks suggested the complex rapidly interconverts between trigonal bipyramidal and octahedral geometry. Under a dry O_2 atmosphere, an EtCN solution of $Zn(L^H)(OTf)_2$ reacts with cobaltocene ($CoCp_2$) at -80°C to form the (*trans*-1,2-peroxo)dizinc complex $[(Zn(L^H))_2(O_2)][OTf]_2$ (**3^H**) in 21% yield (Figure 4-16). In order to obtain **3^H** in higher yield an alternative synthesis was developed. Freshly prepared $Zn(L^H)(OTf)_2$ reacted with a solution of H_2O_2 and N^iPr_2Et at 25°C in MeCN to give **3^H** in 68% yield as a white solid. Complex **3^H** is stable at room temperature in MeCN solution allowing for characterization by ^1H NMR spectroscopy. The aromatic peaks are indicative of C_3-symmetry about Zn and a symmetric resonance for the –NH groups was observed at δ = 10.21. This peak is shifted downfield from free L^H at δ = 7.35 consistent with a H-bonding interaction. The methylene protons in **3^H** are split into coupled doublets at δ = 3.96 and 4.11 (J_{HH} = 15.6 Hz). This asymmetry is indicative of an extremely rigid structure where the pyridine arms are constrained

to a single, symmetric orientation. Solid-state characterization further corroborated a rigid structure.

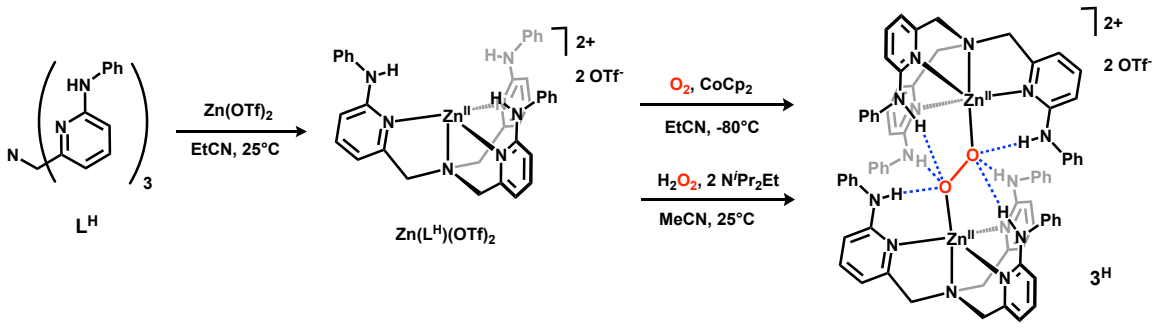

Figure 4-16: Synthesis of $\mathbf{3^H}$ from O_2 and H_2O_2.

A crystal of $\mathbf{3^H}$ suitable for X-ray crystallography was grown from the slow diffusion of diethyl ether into a concentrated solution of $\mathbf{3^H}$ in MeCN at room temperature (Figure 4-17). The geared dimeric structure closely resembles $\mathbf{2^H}$ containing six directed H-bonds to the peroxo unit from the pendent –NHPh groups as well as M–O bonds. While Zn(II) and Cu(II) share similar charge and atomic radius, a closed d-shell prevents Zn(II) from strong ligand binding. The weakened binding in $\mathbf{3^H}$ is expressed in the Zn–N_{axial} and Zn–O bonds at 2.126(5) Å and 1.992(4) Å respectively, which is elongated from $\mathbf{2^H}$ (1.992(3) Å and 1.902(3) Å respectively). The O–O in $\mathbf{3^H}$ (1.499(4) Å) is also elongated from $\mathbf{2^H}$ (1.477(5) Å). We hypothesize that the decrease in π^* donation from peroxide into Zn(II) concentrates electron density in the peroxide antibonding orbitals resulting in O–O bond lengthening. The O–O bond length in $\mathbf{3^H}$ is also consistent with other peroxide ions stabilized only by H-bonding interactions. Similar to the series of complexes with Cu ($\mathbf{2^R}$) we sought to examine how subtle changes to the electronic character of the ligand affected structure and stability.

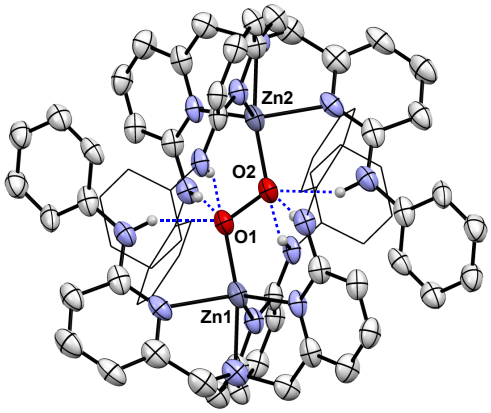

Figure 4-17: X-ray crystal structure of $\mathbf{3^H}$ (30% ellipsoids, H atoms not involved in H-bonding omitted for clarity, some phenyl groups displayed as wireframe).

4.8.3 Synthesis of electron donating –NMe_2 derivative

To increase the number of electronically distinct ligands in the series (L^R), the substituted ligand L^{NMe2} was synthesized (Figure 4-18). Considered one of the most electron donating substituents, *p*-NMe_2 exhibits a Hammett value over three times that of *p*-OMe (-0.83 vs -0.27 respectively). L^{NMe2} was prepared according to our previous Buchwald-Hartwig coupling procedure using Br_3tpa and 4-(dimethylamino)aniline as coupling partners. Although clean formation of the C_3-symmetric complex [Cu(L^{NMe2})]BAr' was observed by ^{1}H NMR, reactions with O_2 at -70°C did not produce an analogous (*trans*-1,2-peroxo)dicopper complex. Instead, the Cu(II) species formed was EPR active and was likely a decomposition product (Figure 4-18). The increased thermal stability of $\mathbf{3^H}$ suggested that the ligand L^{NMe2} may still form productive peroxo complexes with Zn(II).

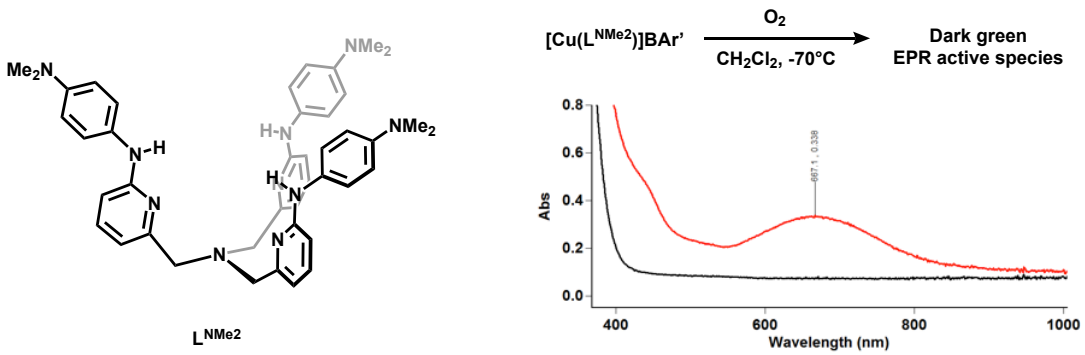

Figure 4-18: Structure of L^{NMe2} and reaction of $[Cu(L^{NMe2})]BAr'$ with O_2.

4.8.4 Characterization of a family of dizinc peroxides

A series of electronically varied (*trans*-1,2-peroxo)dizinc complexes $[(Zn(L^R))_2(O_2)][OTf]_2$ ($\mathbf{3^R}$) was synthesized to assess the impact of H-bonding and ligand electronics on structure. In addition, $\mathbf{3^R}$ also provided a room temperature stable, diamagnetic surrogate for studying the series of thermally-sensitive (*trans*-1,2-peroxo)dicopper complexes ($\mathbf{2^R}$) previously reported. All the $\mathbf{3^R}$ complexes were prepared from the $Zn(L^R)(OTf)_2$ complexes and H_2O_2 described above. ^{1}H NMR spectra for $\mathbf{3^{CF3}}$, $\mathbf{3^{OMe}}$, and $\mathbf{3^{NMe2}}$ showed similar features to $\mathbf{3^H}$ with a single downfield resonance assigned as the –NH peak and methylene protons split into two doublets. The shift of the methylene protons track with the electronic influence of the ligand where the most downfield resonance is displayed by $\mathbf{3^{CF3}}$ (δ = 4.22 and 4.08) and the most upfield resonance by $\mathbf{3^{NMe2}}$ (δ = 4.00 and 3.86). The –NH peaks, however, do not exhibit this trend. $\mathbf{3^H}$ produces the most downfield –NH peak at δ = 10.21 while $\mathbf{3^{OMe}}$ and $\mathbf{3^{NMe2}}$ have the same upfield peak at δ = 10.14 (Figure 4-19). This observation contrasts the $Cu(L^R)Cl$ ($\mathbf{1^R}$) complexes previously reported where the –NH peaks did shift as a function of Hammett value by ^{1}H NMR. Steric congestion in $\mathbf{3^R}$ as well as the interactions of the –NHPh groups with the peroxide ion may be a factor in this discrepancy.

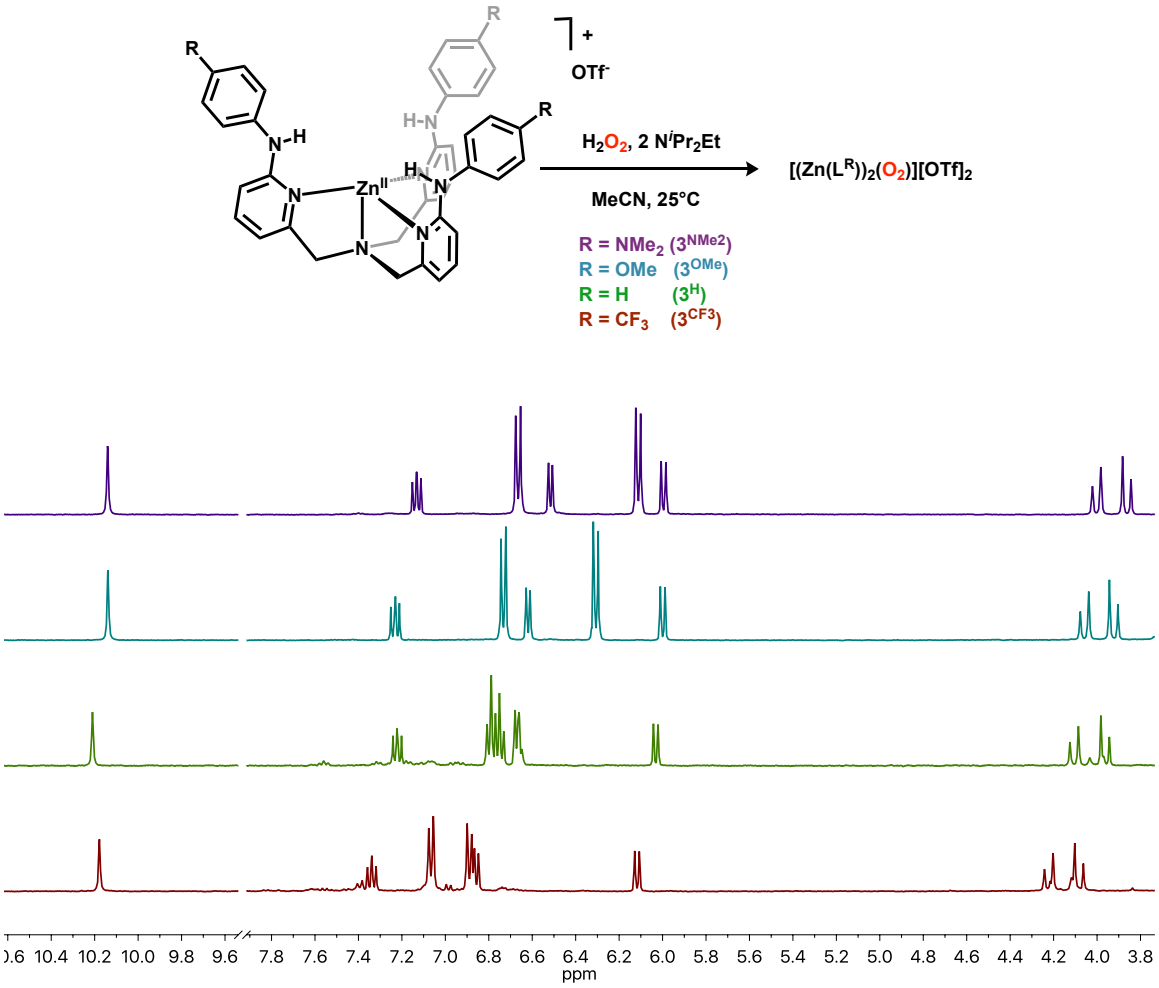

Figure 4-19: Synthesis and overlay of ^{1}H NMR spectra (400 MHz) for **3^R**.

Solid-state characterization of **3^{CF3}**, **3^{OMe}** and **3^{NMe2}** was obtained to structurally compare the dizinc peroxide series (Figure 4-20). The **3^R** complexes were all grown from diethyl ether diffusion into a concentrated MeCN solution and are structurally similar. **3^H**, **3^{OMe}**, and **3^{NMe2}** crystallize in the P-1 space groups while **3^{CF3}** crystallizes in P2$_1$/c. The data quality for **3^{NMe2}** was poor and therefore accurate bond lengths could not be obtained. Even if **3^{NMe2}** is omitted from the comparison, the bond lengths in the other three complexes do not seem to follow a trend based on electronic character. **3^H** displays the shortest O–O bond (1.497(4) Å) and longest Zn–O

bond (1.999(4) Å) while $\mathbf{3}^{\mathbf{CF3}}$ displays the longest O–O bond (1.525(2) Å) and shortest Zn–O bond (1.950(2) Å). The bond metrics for $\mathbf{3}^{\mathbf{OMe}}$ fall between those values. Overall, the $\mathbf{3}^{\mathbf{R}}$ series does consistently exhibit longer metal-ligand bonds and a longer M···M distance (Zn···Zn: 4.72-4.84 Å; Cu···Cu: 4.69 Å) than the $\mathbf{2}^{\mathbf{H}}$ counterpart. Based on the effective charge at Zn due to ligand electronics, the Zn–O and O–O bonds were predicted to elongate going $\mathbf{3}^{\mathbf{CF3}}$ to $\mathbf{3}^{\mathbf{NMe2}}$. The absence of this trend is consistent with the ambiguous ^{1}H NMR data but may also be a result of differences in crystal packing forces. Further spectroscopic data unfortunately did not assist this characterization.

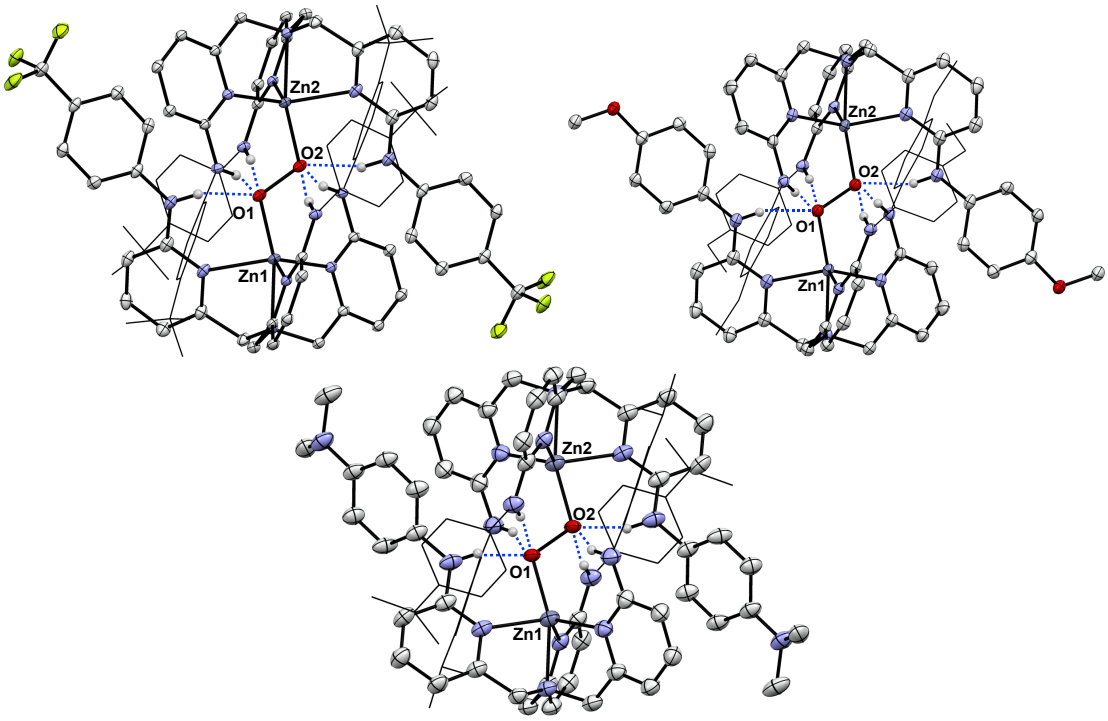

Figure 4-20: X-ray crystal structures of $\mathbf{3}^{\mathbf{CF3}}$ (top left), $\mathbf{3}^{\mathbf{OMe}}$ (top right), and $\mathbf{3}^{\mathbf{NMe2}}$ (bottom) (30% ellipsoids, H atoms not involved in H-bonding omitted for clarity, some phenyl groups displayed as wireframe).

4.8.5 Raman and IR characterization

Raman spectroscopy was used to probe the stretching frequencies for the O–O and Zn–O bonds. Raman spectra of solid samples of $\mathbf{3^R}$ were obtained however no distinct peaks that shifted with electronic character in the regions for a M–O (M = Cu, Zn) or O–O were evident. The synthesis of ^{18}O-enriched $\mathbf{3^H}$ from $H_2{}^{18}O_2$ further supported this observation. Between the region 200 to 1000 cm^{-1}, no peaks exhibited isotopic shifting suggesting that the Zn–O and O–O bond vibrations in $\mathbf{3^H}$ are not observable by Raman spectroscopy (Figure 4-21). Infrared spectroscopy, to investigate changes in the –NH stretching frequency, was also not informative. Strong H-bonds in $\mathbf{3^R}$ shift the –NH stretching frequency to such low energies that they overlap with C-H stretches. For both $\mathbf{2^R}$ and $\mathbf{3^R}$, vibrational spectroscopy was not able to determine the effect of H-bonding and ligand electronics on vibrational modes.

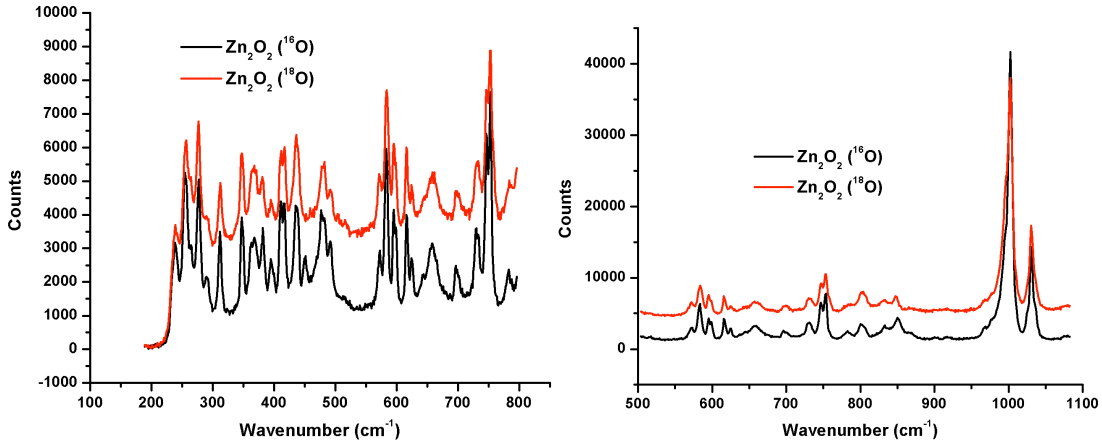

Figure 4-21: Overlay of Raman spectra of $\mathbf{3^H}$ and ^{18}O-enriched $\mathbf{3^H}$ collected at 25°C.

4.9 Zinc diazide complexes

A model system was developed to decouple the electronic and H-bonding impacts on metal-coordinated substrates with the L^R series of ligands. In contrast to peroxides, azide ligands

are weak H-bond acceptors that exhibit strong IR active N–N stretches. The N–N stretch of κ_1-N_3 ligands shifts to higher energies as the ligand is polarized providing a quantitative probe of ligand electronic environment. We hypothesized that octahedral dizinc azide complexes of L^R could decouple H-bonding effects from purely electronic effects since only one azide would be engaged in H-bonding. The series of complexes $Zn(L^R)(N_3)_2$ (**4^R**) were synthesized from the respective $Zn(L^R)(OTf)_2$ complexes by addition of NBu_4N_3 (Figure 4-22). The complexes are C_3-symmetric by ^{1}H NMR; however, the solid-state structure of **4^H** unambiguously shows octahedral coordination. In solution **4^R** is likely rapidly interconverting between trigonal bipyramidal and octahedral. Nevertheless, the ^{1}H NMR spectra for **4^R** show a downfield –NH resonance consistent H-bonding as well as shifts dependent on ligand electronics. The most electron rich diazide complex **4^{NMe2}** displays the furthest upfield –NH and methylene proton resonances (δ = 9.05 and 4.07 respectively), while the electron deficient **4^{CF3}** displays the furthest downfield resonances (δ = 9.41 and 4.14 respectively). In the solid-state structure of **4^H** three –NHPh groups are engaged in H-bonding with the axial N_3 (Figure 4-22). While the Zn–N_{azide} bonds remain similar (Zn–N8: 2.105(2) Å; Zn–N13: 2.104(3) Å), the H-bonding interactions exclusively polarize the axial N_3 unit. The $N_{central}$–$N_{terminal}$ bond shortens on the axial H-bonded N_3 (N9–N10: 1.147(5) Å; N12–N13: 1.217(5) Å) and the $N_{proximal}$–$N_{central}$ bond lengthens (N8–N9: 1.204(4) Å; N11–N12: 1.096(5) Å) compared to the equatorial N_3. The bond lengths in the structure of **4^H** are consistent with N_3 polarization by H-bonding but without structures of the remaining diazide complexes vibrational characterization was required.

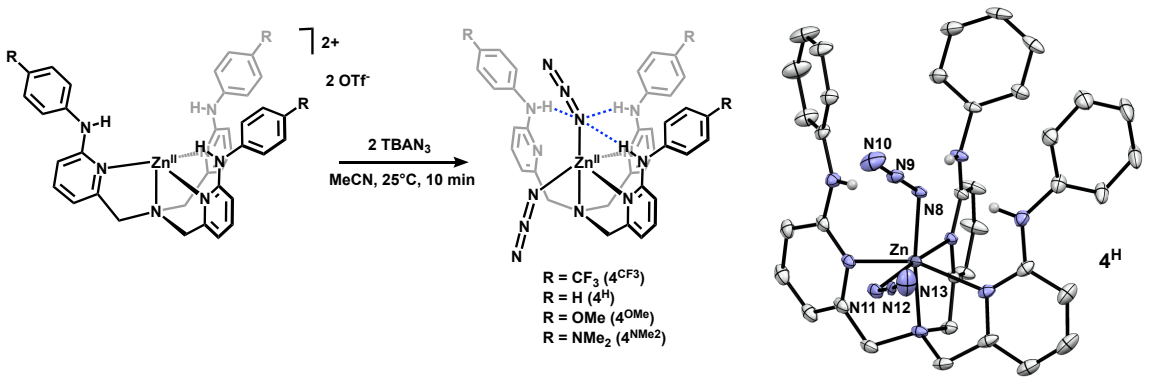

Figure 4-22: Synthesis of $\mathbf{4^R}$ and X-ray crystal structure of $\mathbf{4^H}$ (30% ellipsoids, H atoms not involved in H-bonding omitted for clarity).

The independent impact of H-bonding interactions and electronic character in $\mathbf{4^R}$ was evident by solid-state IR spectroscopy. The equatorial azide ligand – not engaged in H-bonding interactions – exhibits an N–N stretch that shifts as a function of ligand electronics. In $\mathbf{4^H}$, the N–N stretch of the equatorial azide was identified at 2074 cm^{-1}. An electron rich Zn center in $\mathbf{4^{NMe2}}$ produces a weaker N–N stretch at 2069 cm^{-1} while the electron deficient Zn center in $\mathbf{4^{CF3}}$ produces a stronger N–N stretch at 2076 cm^{-1}. This shift in frequency was found to correlate to the Hammett values of *p*-substituted phenyl derivatives (r2 = 0.96, Figure 4-23). The introduction of H-bonding interactions at the axial azide in $\mathbf{4^R}$ had a compound effect on the shift of the N–N stretching frequency. The N–N stretch of the axial azide in $\mathbf{4^H}$ (2051 cm^{-1}) also shifts to lower energy in $\mathbf{4^{NMe2}}$ (2038 cm^{-1}) and higher energy in $\mathbf{4^{CF3}}$ (2057 cm^{-1}); however, the magnitude of the shifts is greater than that of the equatorial azide ($\Delta\nu_{ax}$ = 19 cm^{-1}; $\Delta\nu_{eq}$ = 7 cm^{-1}). The H-bond donor strength (pKa) of the pendent –NHPh groups is likely responsible for the additional polarization changes at the axial azide. Weak H-bond donors like those found in $\mathbf{4^{NMe2}}$ are less able to polarize the azide whereas strong H-bond donors like those in $\mathbf{4^{CF3}}$ will donate heavily into the azide. The H-bond donor strength and ligand electronic character combine to

produce the observed axial azide shifts. Since the pKa of *p*-substituted anilines and Hammett values of *p*-substituted phenyls are closely related, the axial azide shifts also correlate with Hammett value, albeit with a steeper slope (r2 = 0.99).

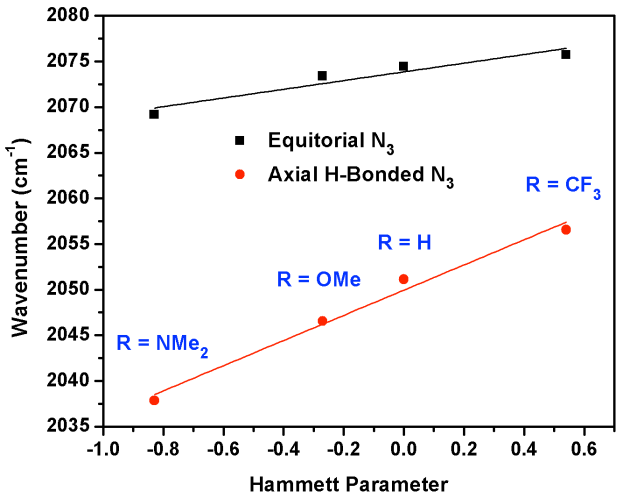

Figure 4-23: Plot of the azide N–N stretches in **4**$^{\mathbf{R}}$ against the associated Hammett values for *p*-substituted phenyl derivatives.

We have demonstrated the stabilization of the first (*trans*-1,2,-peroxo)dizinc complex by using H-bonding interactions and a Lewis acidic Zn(II) center to template the ligand. The L^{R} ligands provide a unique combination of tunable secondary sphere H-bond donors and electronic properties that were used to synthesize a series of dizinc peroxides that exhibit varying structural and spectroscopic characteristics. A series of zinc diazide complexes with L^{R} showed a compound effect on azide polarization helping to decouple the electronic and H-bonding components.

4.10 Experimental Details

General Considerations: All commercially-available reagents were used as received without further purification. Tris(6-bromo-2-pyridylmethyl)amine (Br_3tpa),[19] [Cu(MeCN)$_4$]BAr' (BAr'=B(C_6F_5)$_4$),[20] and benzyl potassium[21] were prepared according to the literature. All manipulations were carried out under an atmosphere of nitrogen in an Innovative Technologies Pure LabHE GP-1 glovebox or using Shlenk techniques, unless otherwise specified. NMR spectra were collected on a Varian MR400, nmrs500, or nmrs700 and were referenced to residual solvent peaks. ^{19}F NMR spectra were referenced to their respective ^{1}H spectra. Flash chromatography was performed on a Biotage Isolera One automated system using self-packed 25g or 50g columns. IR spectra were collected on a Nicolet is10 spectrometer as a solution in CH_2Cl_2. EPR spectra were collected on a Bruker EMX EPR spectrometer. Electronic absorption spectra were collected on a Varian Cary-50 spectrophotometer using a Hellma Analytics 661.200-QX quartz probe. Voltammetry experiments were conducted using a Pine WaveNow potentiostat under N_2 in a cell consisting of a glassy carbon working electrode, platinum counter electrode and a silver wire reference electrode. All voltammetry experiments were referenced to an internal ferrocene (Fc) or decamethylferrocene (Fc*) reference (Fc* = -510 mV vs Fc/Fc^+ in 0.1M NBu_4PF_6 MeCN measured in-house) introduced at the end of the experiment. High-resolution mass spectrometry was collected on an Agilent 6230 TOF HPLC-MS.

Synthesis of tris(6-phenylamino-2-pyridylmethyl)amine (L^H): In the air, a 250 mL Schlenk flask was charged with Br_3tpa (1000.0 mg; 1.897 mmol), $Pd(OAc)_2$ (38.3 mg; 0.171 mmol), BINAP (159.5 mg; 0.256 mmol), Cs_2CO_3 (3709.6 mg; 11.382 mmol), and a Teflon stirbar. The flask was then subjected to multiple evacuation refill cycles with N_2. An N_2-sparged mixture of

80 mL toluene and aniline (1590.0 mg; 17.073 mmol) was added to the Schlenk flask via cannula. The solution was heated at 100°C with vigorous stirring (1200 rpm) for 12 hours. Following heating, the reaction was allowed to cool to room temperature over 1 hour. The reaction mixture was filtered over a celite plug and washed with toluene (2 x 10 mL). The combined filtrates were placed in a -20°C freezer for 8 hours over which time the product crystallized from solution. The red toluene solution was decanted and the crystals were washed with 20 mL cold toluene. The yellow crystalline solid was further purified by recrystallization from 10 mL hot acetonitrile. The off-white crystalline powder precipitates at -20°C and was isolated, washed with 5 mL cold acetonitrile, and dried overnight in vacuo to obtain pure L^H (640.0 mg, 60%). IR (CH_2Cl_2, cm^{-1}): 3431 and 3408 (NH). ^1H NMR (700 MHz, Methylene Chloride-d_2) δ 7.49 (dd, J = 8.2, 7.4 Hz, 3H), 7.42 (d, J = 7.4 Hz, 6H), 7.30 (dd, J = 7.4, 7.3 Hz, 6H), 7.13 (d, J = 7.4 Hz, 3H), 7.00 (t, J = 7.3 Hz, 3H), 6.71 (d, J = 8.2 Hz, 3H), 6.57 (s, 3H), 3.80 (s, 6H). ^{13}C NMR (176 MHz, Methylene Chloride-d_2) δ 159.1, 155.6, 141.4, 138.3, 129.4, 122.4, 119.8, 114.2, 107.1, 60.6. HRMS (ESI-TOF) m/z: $[L^H+H]^+$ Calcd for $C_{36}H_{34}N_7$: 564.2876; Found: 564.2879.

Synthesis of tris(6-(4-trifluoromethylphenyl)amino-2-pyridylmethyl)amine (L^{CF3}): In the air, a 20 mL glass scintillation vial was charged with Br_3tpa (250.0 mg; 0.4743 mmol), $Pd(OAc)_2$ (9.6 mg; 0.0427 mmol), BINAP (39.9mg; 0.0640 mmol), Cs_2CO_3 (927.5 mg; 2.846 mmol), 4-trifluoromethylaniline (687.8 mg; 4.2687 mmol), and a Teflon stirbar. 20 mL of N_2-sparged toluene was added and the vial was quickly sealed with a Teflon-lined cap. The solution was heated at 100°C with vigorous stirring (1300 rpm) for 18 hours. Following heating, the reaction was cooled to room temperature and 20 mL of CH_2Cl_2 was added and stirred for an additional 5

min. The slurry was filtered over a celite plug and washed with CH_2Cl_2 (2 x 10 mL). The filtrate was then dry loaded onto silica gel via rotary evaporation. The dry loaded product was purified by flash chromatography on a Biotage Isolera One using a 25 g self-packed silica gel column. Method: 3 column volumes (CV) of 80% hexane: 20% ethyl acetate, then a gradient of 15 CV to 50% hexane: 50% ethyl acetate. Product elutes between 9-14 CV. Fractions containing product were evaporated to dryness via rotary evaporation. The light yellow solid was dried overnight in vacuo to obtain pure L^{CF3} (275 mg; 76%). IR (CH_2Cl_2, cm^{-1}): 3430 (NH). ^{1}H NMR (700 MHz, Methylene Chloride-d_2) δ 7.64 (d, J = 8.4 Hz, 6H), 7.55 (dd, J = 8.2, 7.4 Hz, 3H), 7.51 (d, J = 8.4 Hz, 6H), 7.20 (d, J = 7.4 Hz, 3H), 6.72 (d, J = 8.2 Hz, 3H), 6.71 (s, 3H), 3.87 (s, 6H). ^{13}C NMR (176 MHz, Methylene Chloride-d_2) δ 158.9, 154.5, 144.7, 138.5, 126.6 (q, J_{CF} = 4 Hz), 125.1 (q, J_{CF} = 271 Hz), 122.9 (q, J_{CF} = 32 Hz), 118.0, 115.4, 108.8, 60.6. ^{19}F NMR (377 MHz, Methylene Chloride-d_2) δ -61.9. HRMS (ESI-TOF) m/z: $[L^{CF3}+H]^+$ Calcd for $C_{39}H_{31}F_9N_7$: 768.2497; Found: 768.2493.

Synthesis of tris(6-(4-methoxyphenyl)amino-2-pyridylmethyl)amine (L^{OMe}): In the air, a 20 mL glass scintillation vial was charged with Br_3tpa (250.0 mg; 0.4743 mmol), $Pd(OAc)_2$ (9.6 mg; 0.0427 mmol), BINAP (39.9mg; 0.0640 mmol), Cs_2CO_3 (927.5 mg; 2.846 mmol), 4-methoxyaniline (525.7 mg; 4.2687 mmol), and a Teflon stirbar. 20 mL of N_2-sparged toluene was added and the vial was quickly sealed with a Teflon-lined cap. The solution was heated at 100°C with vigorous stirring (1300 rpm) for 18 hours. Following heating, the reaction was cooled to room temperature and 20 mL of CH_2Cl_2 was added and stirred for an additional 5 min. The slurry was filtered over a celite plug and washed with CH_2Cl_2 (2 x 10 mL). The filtrate was then dry loaded onto silica gel via rotary evaporation. The dry loaded product was purified by

flash chromatography on a Biotage Isolera One using a 25 g self-packed silica gel column. Method: 3 column volumes (CV) of 60% hexane: 40% ethyl acetate, then a gradient of 20 CV to 100% ethyl acetate. Product elutes between 13-18 CV. Fractions containing product were evaporated to dryness via rotary evaporation. The brown solid was further purified by recrystallization from 4 mL hot toluene. The light brown powder precipitates at room temperature and was isolated and dried overnight in vacuo to obtain pure L^{OMe} (228 mg, 74%). IR (CH_2Cl_2, cm^{-1}): 3433 and 3409 (NH). ^1H NMR (700 MHz, Methylene Chloride-d_2) δ 7.44 (dd, J = 8.2, 7.4 Hz, 3H), 7.30 (d, J = 8.8 Hz, 6H), 7.05 (d, J = 7.4 Hz, 3H), 6.87 (d, J = 8.8 Hz, 6H), 6.55 (d, J = 8.2 Hz, 3H), 6.41 (s, 3H), 3.78 (s, 9H), 3.74 (s, 6H). ^{13}C NMR (176 MHz, Methylene Chloride-d_2) δ 159.1, 156.7, 156.2, 138.2, 134.2, 123.3, 114.7, 113.5, 105.9, 60.6, 55.9. HRMS (ESI-TOF) m/z: $[L^{OMe}+H]^+$ Calcd for $C_{39}H_{40}N_7O_3$: 654.3193; Found: 654.3188.

Synthesis of tris(6-(4-dimethylaminophenyl)amino-2-pyridylmethyl)amine (L^{NMe2}): In the air, a 20 mL glass scintillation vial was charged with Br_3tpa (200.0 mg; 0.3795 mmol), $Pd(OAc)_2$ (7.7 mg; 0.0342 mmol), BINAP (31.9 mg; 0.0512 mmol), Cs_2CO_3 (742.1 mg; 2.277 mmol), 4-dimethylamino-aniline (465.1 mg; 3.4155 mmol), and a Teflon stirbar. 20 mL of N_2-sparged toluene was added and the vial was quickly sealed with a Teflon-lined cap. The solution was heated at 100°C with vigorous stirring (1300 rpm) for 18 hours. Following heating, the reaction was cooled to room temperature and 20 mL of CH_2Cl_2 was added and stirred for an additional 5 min. The slurry was filtered over a celite plug and washed with CH_2Cl_2 (2 x 10 mL). The filtrate was then dry loaded onto silica gel via rotary evaporation. The dry loaded product was purified by flash chromatography on a Biotage Isolera One using a 25 g self-packed silica gel column. Method: 3 column volumes (CV) of 70% hexane: 30% ethyl acetate, then a gradient of 15 CV to

100% ethyl acetate, then 10 CV of 100% ethyl acetate. Product elutes between 20-26 CV. Fractions containing product were evaporated to dryness via rotary evaporation. The brown solid was further purified by recrystallization from 4 mL hot toluene. The light brown powder precipitates at room temperature and was isolated and dried overnight in vacuo to obtain pure L^{NMe2} (127 mg, 48%). ^{1}H NMR (700 MHz, Methylene Chloride-d_2) δ 7.41 (dd, J = 7.3, 8.2 Hz, 3H), 7.20 (d, J = 8.5 Hz, 6H), 7.02 (d, J = 7.3 Hz, 3H), 6.73 (d, J = 8.5 Hz, 6H), 6.49 (d, J = 8.2 Hz, 3H), 6.30 (s, 3H), 3.72 (s, 6H), 2.91 (s, 18H). ^{13}C NMR (176 MHz, Methylene Chloride-d_2) δ 159.2, 157.5, 148.2, 138.2, 130.6, 124.2, 113.8, 113.0, 105.2, 60.6, 41.2. HRMS (ESI-TOF) m/z: $[L^{NMe2}+H]^+$ Calcd for $C_{42}H_{49}N_{10}$: 693.4142; Found: 693.4185.

Synthesis of tris(6-phenoxy-2-pyridylmethyl)amine (tpa^{OPh}): To a freshly prepared 3 mL solution of benzyl potassium (173.0 mg; 1.328 mmol) in THF was added a 3 mL solution of phenol (142.8 mg; 1.518 mmol) in THF. The mixture was let stir for 1 min as KOPh precipitated as a white solid. The THF was then removed in vacuo. To the vial containing KOPh was added CuI (36.1 mg; 0.190 mmol), Br_3tpa (200.0 mg; 0.3795 mmol) and 10 mL toluene. The mixture was stirred at 100°C for 20 hours followed by cooling to room temperature. 20 mL of CH_2Cl_2 was added and stirred for an additional 5 min. The slurry was filtered over a celite plug and washed with CH_2Cl_2 (2 x 10 mL). The filtrate was then dry loaded onto silica gel via rotary evaporation. The dry loaded product was purified by flash chromatography on a Biotage Isolera One using a 25 g self-packed silica gel column. Method: 3 column volumes (CV) of 95% hexane: 5% ethyl acetate, then a gradient of 15 CV to 100% ethyl acetate. Product elutes between 8-9 CV. Fractions containing product were evaporated to dryness via rotary evaporation. The product was further purified by recrystallization from 4 mL hot ethanol and

dried overnight in vacuo to yield pure tpa^{OPh} (81.1 mg, 38%) as a white solid. ^{1}H NMR (700 MHz, Methylene Chloride-d_2) δ 7.56 (dd, J = 8.1, 7.4 Hz, 3H), 7.37 (dd, J = 7.7, 7.4 Hz, 6H), 7.18 (t, J = 7.4 Hz, 3H), 7.15 (d, J = 7.4 Hz, 3H), 7.11 (d, J = 7.7 Hz, 6H), 6.72 (d, J = 8.1 Hz, 3H), 3.60 (s, 6H). ^{13}C NMR (176 MHz, Methylene Chloride-d_2) δ 163.4, 158.6, 155.0, 140.1, 129.9, 124.6, 121.5, 118.0, 109.8, 59.4. HRMS (ESI-TOF) m/z: $[tpa^{OPh}+H]^+$ Calcd for $C_{36}H_{31}N_4O_3$: 567.2396; Found: 567.2465.

Synthesis of Cu(L^H)Cl (1^H): CuCl (5.9 mg; 0.0596 mmol), L^H (35.3 mg ; 0.0626 mmol), 3 mL THF, and a Teflon stir bar were added to a 20 mL glass scintillation vial and stirred for 48 hours at room temperature. The yellow solution was then evaporated to dryness with vacuum. The yellow solid was dissolved in 2 mL CH_2Cl_2, filtered though a glass pipette fitted with glass filter paper, and concentrated to 1 mL CH_2Cl_2. The product was then precipitated by addition of 5 mL diethyl ether. The yellow powder was collected and washed twice with 3 mL diethyl ether and dried overnight under vacuum to obtain pure **1^H** (24.6 mg, 59%). A crystal suitable for X-ray diffraction was grown by layering pentane over a concentrated toluene solution at -30°C. IR (CH_2Cl_2, cm^{-1}): 3223 (NH). ^{1}H NMR (700 MHz, Methylene Chloride-d_2) δ 9.89 (s, 3H), 7.43 (dd, J = 8.4, 7.2 Hz, 3H), 7.32 (m, 12H), 7.03 (t, J = 7.1 Hz, 3H), 7.01 (d, J = 8.4 Hz, 3H), 6.59 (d, J = 7.2 Hz, 3H), 3.69 (s, 6H). ^{13}C NMR (176 MHz, Methylene Chloride-d_2) δ 157.3, 155.3, 140.9, 138.6, 129.6, 123.3, 121.2, 113.8, 107.1, 59.3. HRMS (ESI-TOF) m/z: $[Cu(L^H)Cl]^+$ Calcd for $C_{36}H_{33}ClCuN_7$: 661.1782; Found: 661.1763.

Synthesis of Cu(L^{CF3})Cl (1^{CF3}): CuCl (0.8 mg; 0.0081 mmol), L^{CF3} (6.5 mg ; 0.0085 mmol), 3 mL benzene, and a Teflon stir bar were added to a 20 mL glass scintillation vial and stirred for

12 hours at room temperature. A yellow precipitate formed in solution that was then isolated by filtration over a glass pipette fitted with a glass filter plug. The yellow solid was washed twice with benzene (2 mL) and twice with pentane (2 mL) before dissolving in 5 mL CH_2Cl_2 and passing over the frit. The light yellow solution was pumped down to dryness in vacuo overnight to yield pure $\mathbf{1^{CF3}}$ (2.1 mg, 29%). IR (CH_2Cl_2, cm^{-1}): 3221 (NH). ^{1}H NMR (700 MHz, Methylene Chloride-d_2) δ 10.17 (s, 3H), 7.54 (d, J = 8.3 Hz, 6H), 7.52 (dd, J = 8.3, 7.3 Hz, 3H), 7.42 (d, J = 8.3 Hz, 6H), 7.12 (d, J = 8.3 Hz, 3H), 6.69 (d, J = 7.3 Hz, 3H), 3.73 (s, 6H). ^{13}C NMR (176 MHz, Methylene Chloride-d_2) δ 156.0, 155.5, 144.4, 139.0, 126.8, 126.5 (q, J_{CF} = 271 Hz), 124.1 (q, J_{CF} = 31 Hz), 119.2, 115.1, 108.2, 59.3. (Note: $\mathbf{1^{CF3}}$ is only slightly soluble in CH_2Cl_2 leading to a weak ^{13}C NMR signal). ^{19}F NMR (377 MHz, Methylene Chloride-d_2) δ -62.1. HRMS (ESI-TOF) m/z: $[Cu(L^{CF3})Cl]^+$ Calcd for $C_{39}H_{30}ClCuF_9N_7$: 865.1404; Found: 865.1378.

Synthesis of Cu(L^{OMe})Cl ($\mathbf{1^{OMe}}$): CuCl (2.8 mg; 0.0283 mmol), L^{OMe} (19.4 mg ; 0.0297 mmol), 3 mL THF, and a Teflon stir bar were added to a 20 mL glass scintillation vial and stirred for 48 hours at room temperature. The yellow solution was then evaporated to dryness with vacuum. The yellow solid was dissolved in 2 mL CH_2Cl_2, filtered though a glass pipette fitted with glass filter paper, and concentrated to 1 mL CH_2Cl_2. 5 mL diethyl ether was added to the vial and the product slowly crystallized out of solution as yellow needles over 1 hour. The yellow crystals were washed twice with 3 mL diethyl ether and dried overnight under vacuum to obtain pure $\mathbf{1^{OMe}}$ (19.3 mg, 86%). IR (CH_2Cl_2, cm^{-1}): 3220 (NH). ^{1}H NMR (700 MHz, Methylene Chloride-d_2) δ 9.72 (s, 3H), 7.37 (dd, J = 8.1, 7.7 Hz, 3H), 7.286 (d, J = 8.4 Hz, 6H), 6.88 (d, J = 8.4 Hz, 6H), 6.79 (d, J = 8.1 Hz, 3H), 6.53 (d, J = 7.7 Hz, 3H), 3.78 (s, 9H), 3.65 (s, 6H). ^{13}C NMR (176 MHz, Methylene Chloride-d_2) δ 158.4, 156.6, 155.2, 138.4, 133.7, 124.2, 114.9, 113.0, 106.4,

59.2, 55.8. HRMS (ESI-TOF) m/z: $[Cu(L^{OMe})Cl]^+$ Calcd for $C_{39}H_{39}ClCuN_7O_3$: 751.2099; Found: 751.2082.

Synthesis of $[Cu_2(L^H)_2O_2]BAr'_2$ (2^H): In a nitrogen-filled glovebox, $[Cu(MeCN)_4]BAr'$ (6.9 mg; 0.0076 mmol) and L^H (4.3 mg; 0.0076 mmol) were dissolved in 5.1 mL CH_2Cl_2 in a 25 mL round bottom flask to produce a 1.5 mM solution of $[Cu(L^H)]BAr'$. The round bottom flask was sealed with a rubber septum and cable tie, removed from the glovebox, and transferred via cannula to a dry, N_2-filled vessel containing the UV-Vis dip probe. The dip probe glassware containing $[Cu(L^H)]BAr'$ was placed in a -70°C dry ice/acetone bath and the solution stirred for ~5 min. Dry oxygen was bubbled through the solution while the headspace was allowed to purge resulting in a color change from colorless to brown indicating formation of $\mathbf{2^H}$. Completion of the reaction was assessed by UV-Vis. [Note: due to the insolubility of $\mathbf{2^{CF3}}$ in pure CH_2Cl_2, comparison spectra were taken in 1:1 CH_2Cl_2:acetone by first formation of $\mathbf{2^H}$ in 3 mM $[Cu(L^H)]BAr'$ CH_2Cl_2 followed by slow addition of cold acetone.] A crystal of $\mathbf{2^H}$ suitable for X-ray diffraction was obtained by allowing a concentrated CH_2Cl_2 solution of $[Cu(L^H)]BAr'$ to sit under an atmosphere of dry O_2 in a sealed Schlenk flask for 3 days in a -80°C freezer. λ_{max} (1:1, CH_2Cl_2:acetone)/nm 457 (ε, $M^{-1}cm^{-1}$ 3100), 701 (600), 830 (600).

Synthesis of $[Cu_2(L^{CF3})_2O_2]BAr'_2$ (2^{CF3}): In a nitrogen-filled glovebox, $[Cu(MeCN)_4]BAr'$ (8.2 mg; 0.0090 mmol) and L^{CF3} (6.9 mg; 0.0090 mmol) were dissolved in 3.0 mL CH_2Cl_2 in a 25 mL round bottom flask to produce a 3.0 mM solution of $[Cu(L^{CF3})]BAr'$. The round bottom flask was sealed with a rubber septum and cable tie, removed from the glovebox, and transferred via cannula to a dry, N_2-filled vessel containing the UV-Vis dip probe. The dip probe glassware

containing [Cu(L^{CF3})]BAr' was placed in a -70°C dry ice/acetone bath and the solution stirred for ~5 min. Dry oxygen was bubbled through the solution while the headspace was allowed to purge resulting in a color change from colorless to brown followed by immediate formation of a light brown precipitate. The solid (**2^{CF3}**) could be dissolved by addition of 1 part cold acetone to the solution in order to extract UV-Vis data. Completion of the reaction was assessed by UV-Vis. λ_{max} (1:1, CH_2Cl_2:acetone)/nm 450 (ε, $M^{-1}cm^{-1}$ 2400), 696 (600), 831 (600).

Synthesis of [$Cu_2(L^{OMe})_2O_2$]BAr'$_2$ (2^{OMe}): In a nitrogen-filled glovebox, [Cu(MeCN)$_4$]BAr' (6.1 mg; 0.0067 mmol) and L^{OMe} (4.4 mg; 0.0067 mmol) were dissolved in 4.5 mL CH_2Cl_2 in a 25 mL round bottom flask to produce a 1.5 mM solution of [Cu(L^{OMe})]BAr'. The round bottom flask was sealed with a rubber septum and cable tie, removed from the glovebox, and transferred via cannula to a dry, N_2-filled vessel containing the UV-Vis dip probe. The dip probe glassware containing [Cu(L^{OMe})]BAr' was placed in a -70°C dry ice/acetone bath and the solution stirred for ~5 min. Dry oxygen was bubbled through the solution while the headspace was allowed to purge resulting in a color change from colorless to brown indicating formation of **2^{OMe}**. Completion of the reaction was assessed by UV-Vis. [Note: due to the insolubility of **2^{CF3}** in pure CH_2Cl_2, comparison spectra were taken in 1:1 CH_2Cl_2:acetone by first formation of **2^{OMe}** in 3 mM [Cu(L^{OMe})]BAr' CH_2Cl_2 followed by slow addition of cold acetone.] λ_{max} (1:1, CH_2Cl_2:acetone)/nm 460 (ε, $M^{-1}cm^{-1}$ 2500), 696 (500), 827 (500).

Synthesis of [$Zn_2(L^H)_2O_2$]$(OTf)_2$ (3^H): Method A: Method B: In a 20 mL glass scintillation vial open to air Zn$(OTf)_2$ (32.7 mg; 0.0901 mmol) and L^H (50.8 mg; 0.0901 mmol) was dissolved in 5 mL MeCN and stirred for 5 min. 30% H_2O_2 in H_2O (18.4 μL; 0.1802 mmol) and N^{i}Pr$_2$Et (17.3

μL; 0.0991 mmol) was added to the vial in succession and stirred for 10 min. The solution was evaporated to dryness with vacuum and washed with benzene (3 x 2mL) followed by diethyl ether (3 x 2 mL). The white solid was dried overnight under vacuum to obtain pure $\mathbf{3^H}$ (77.7 mg, 90% yield). ^{1}H NMR (400 MHz, Acetonitrile) δ 10.21 (s, 3H), 7.22 (dd, *J* = 7.2, 8.6 Hz, 3H), 6.77 (m, 12H), 6.67 (d, *J* = 7.3 Hz, 6H), 6.03 (d, *J* = 8.6 Hz, 3H), 4.11 (d, *J* = 15.6 Hz, 3H), 3.96 (d, *J* = 15.6 Hz, 3H).

Synthesis of $[Zn_2(L^{CF3})_2O_2](OTf)_2$ ($\mathbf{3^{CF3}}$): In a 20 mL glass scintillation vial open to air $Zn(OTf)_2$ (34.7 mg; 0.0941 mmol) and L^{CF3} (72.2 mg; 0.0941 mmol) was dissolved in 2 mL MeCN and stirred for 5 min. 30% H_2O_2 in H_2O (19.2 μL; 0.1882 mmol) and N^iPr_2Et (16.4 μL; 0.0941 mmol) was added to the vial in succession and stirred for 10 min. The reaction solution was then evaporated to dryness under vacuum. A minimal amount of MeCN (~1 mL) was added followed by 4 mL diethyl ether to crash out the product as a white precipitate. Product was collected on a frit, washed with diethyl ether (2 x 2mL) and dried overnight under vacuum to obtain pure $\mathbf{3^{CF3}}$ (54.6 mg, 29% yield). ^{1}H NMR (40 MHz, Acetonitrile) δ 10.18 (s, 3H), 7.34 (dd, *J* = 7.2, 8.5 Hz, 3H), 7.07 (d, *J* = 8.4 Hz, 6H), 6.89 (d, *J* = 8.4 Hz, 6H), 6.86 (d, *J* = 7.2 Hz, 3H), 6.12 (d, *J* = 8.5 Hz, 3H) 4.22 (d, *J* = 15.9 Hz, 3H), 4.08 (d, *J* = 15.9 Hz, 3H).

Synthesis of $[Zn_2(L^{OMe})_2O_2](OTf)_2$ ($\mathbf{3^{OMe}}$): In a 20 mL glass scintillation vial open to air $Zn(OTf)_2$ (34.4 mg; 0.0946 mmol) and L^{OMe} (61.9 mg; 0.0946 mmol) was dissolved in 2 mL MeCN and stirred for 5 min. 30% H_2O_2 in H_2O (19.3 μL; 0.1892 mmol) and N^iPr_2Et (16.5 μL; 0.0946 mmol) was added to the vial in succession and stirred for 10 min. The product began to precipitate as a white solid over the 10 min and 2 mL diethyl ether was added to facilitate

precipitation. The precipitate was collected on a glass frit, washed with diethyl ether (2 x 2 mL), and dried overnight under vacuum to obtain pure $\mathbf{3^{OMe}}$ (70.0 mg, 42% yield). ^{1}H NMR (400 MHz, Acetonitrile) δ 10.14 (s, 3H), 7.23 (dd, *J* = 7.1, 8.6 Hz, 3H), 6.73 (d, *J* = 8.9 Hz, 6H), 6.62 (d, *J* = 7.1 Hz, 3H), 6.31 (d, *J* = 8.9 Hz, 6H), 6.00 (d, *J* = 8.6 Hz, 3H), 4.06 (d, *J* = 15.6 Hz, 3H), 3.92 (d, *J* = 15.6 Hz, 3H), 3.51 (s, 9H).

Synthesis of $[Zn_2(L^{NMe2})_2O_2](OTf)_2$ ($\mathbf{3^{NMe2}}$): In a 20 mL glass scintillation vial open to air $Zn(OTf)_2$ (28.0 mg; 0.0771 mmol) and L^{NMe2} (53.4 mg; 0.0771 mmol) was dissolved in 2 mL MeCN and stirred for 5 min. 30% H_2O_2 in H_2O (15.7 µL; 0.1542 mmol) and N^iPr_2Et (13.4 µL; 0.0771 mmol) was added to the vial in succession and stirred for 10 min. 5 mL diethyl ether was added to crash out the product as an off-white precipitate. Product was collected on a frit, washed with diethyl ether (2 x 2mL) and dried overnight under vacuum to obtain pure $\mathbf{3^{NMe2}}$ (52.7 mg, 37% yield). ^{1}H NMR (400 MHz, Acetonitrile) δ 10.14 (s, 3H), 7.13 (dd, *J* = 7.1, 8.6 Hz, 1H), 6.66 (d, *J* = 9.0 Hz, 6H), 6.52 (d, *J* = 7.1 Hz, 3H), 6.11 (d, *J* = 9.0 Hz, 6H), 6.00 (d, *J* = 8.6 Hz, 3H), 4.00 (d, *J* = 15.5 Hz, 3H), 3.86 (d, *J* = 15.5 Hz, 3H), 2.66 (2, 18H).

Synthesis of $Zn(L^H)(N_3)_2$ ($\mathbf{4^H}$): In a 20 mL glass scintillation vial open to air $Zn(ClO_4)_2$ x $6H_2O$ (1.5 mg; 0.0041 mmol) and L^H (2.3 mg; 0.0041 mmol) were dissolved in 1 mL MeCN and stirred for 5 min. A solution of NBu_4N_3 (2.6 mg; 0.0090 mmol) in 1 mL MeCN was added to the vial and stirred for 30 min. The reaction solution was evaporated to dryness under vacuum to obtain solid $\mathbf{4^H}$. Product formation was confirmed by ^{1}H NMR and solid-state IR. A crystal suitable for X-ray diffraction was grown from vapor diffusion of diethyl ether into a concentrated MeCN solution of $\mathbf{4^H}$ at room temperature. ^{1}H NMR (400 MHz, Acetonitrile) δ 9.28 (s, 3H), 7.45

(dd, *J* = 7.2, 7.6 Hz, 3H), 7.20 (dd, *J* = 7.6, 8.5 Hz, 6H), 7.02 (t, *J* = 7.6 Hz, 3H), 6.98 (d, *J* = 7.6 Hz, 6H), 6.83 (d, *J* = 8.5 Hz, 3H), 6.56 (d, *J* = 7.2 Hz, 3H), 4.11 (s, 6H).

Synthesis of $Zn(L^{CF3})(N_3)_2$ (4^{CF3}): In a 20 mL glass scintillation vial open to air $Zn(ClO_4)_2$ x $6H_2O$ (1.5 mg; 0.0041 mmol) and L^{CF3} (3.1 mg; 0.0041 mmol) were dissolved in 1 mL MeCN and stirred for 5 min. A solution of NBu_4N_3 (2.6 mg; 0.0090 mmol) in 1 mL MeCN was added to the vial and stirred for 30 min. The reaction solution was evaporated to dryness under vacuum to obtain solid $\mathbf{4^{CF3}}$. Product formation was confirmed by ^{1}H NMR and solid-state IR. ^{1}H NMR (400 MHz, Acetonitrile) δ 9.42 (s, 3H), 7.54 (dd, *J* = 7.2, 8.6 Hz, 3H), 7.39 (d, *J* = 8.3 Hz, 6H), 7.05 (d, *J* = 8.3 Hz, 6H), 6.98 (d, *J* = 8.6 Hz, 6H), 6.70 (d, *J* = 7.2 Hz, 3H), 4.14 (s, 6H).

Synthesis of $Zn(L^{OMe})(N_3)_2$ (4^{OMe}): In a 20 mL glass scintillation vial open to air $Zn(ClO_4)_2$ x $6H_2O$ (1.5 mg; 0.0041 mmol) and L^{OMe} (2.7 mg; 0.0041 mmol) were dissolved in 1 mL MeCN and stirred for 5 min. A solution of NBu_4N_3 (2.6 mg; 0.0090 mmol) in 1 mL MeCN was added to the vial and stirred for 30 min. The reaction solution was evaporated to dryness under vacuum to obtain solid $\mathbf{4^{OMe}}$. Product formation was confirmed by ^{1}H NMR and solid-state IR. ^{1}H NMR (400 MHz, Acetonitrile) δ 9.11 (s, 3H), 7.39 (dd, *J* = 7.1, 8.5 Hz, 3H), 6.91 (d, *J* = 8.8 Hz, 6H), 6.77 (d, *J* = 8.8 Hz, 6H), 6.60 (d, *J* = 8.5 Hz, 6H), 6.49 (d, *J* = 7.1 Hz, 3H), 4.08 (s, 6H), 3.72 (s, 9H).

Synthesis of $Zn(L^{NMe2})(N_3)_2$ (4^{NMe2}): In a 20 mL glass scintillation vial open to air $Zn(ClO_4)_2$ x $6H_2O$ (1.5 mg; 0.0041 mmol) and L^{NMe2} (2.8 mg; 0.0041 mmol) were dissolved in 1 mL MeCN and stirred for 5 min. A solution of NBu_4N_3 (2.6 mg; 0.0090 mmol) in 1 mL MeCN was added to

the vial and stirred for 30 min. The reaction solution was evaporated to dryness under vacuum to obtain solid $\mathbf{4}^{\mathbf{NMe2}}$. Product formation was confirmed by ^{1}H NMR and solid-state IR. ^{1}H NMR (400 MHz, Acetonitrile) δ 9.04 (s, 3H), 7.35 (dd, J = 7.0, 8.6 Hz, 3H), 6.83 (d, J = 8.7 Hz, 6H), 6.61 (d, J = 8.9 Hz, 6H), 6.52 (d, J = 8.6 Hz, 3H), 6.44 (d, J = 7.0 Hz, 3H), 4.06 (s, 6H).

Crystallography Details:

Crystals were mounted on a Rigaku AFC10K Saturn 944+ CCD-based X-ray diffractometer with a low temperature apparatus and Micromax-007HF Cu-target micro-focus rotating anode (λ = 1.54187 A) operated at 1.2 kW power (40 kV, 30 mA). Samples were measured at 85(2)K. The data were processed with CrystalClear 2.0[22] and corrected for absorption. Structures were solved in Olex2[23] using the XL refinement program[24].

4.11 Notes and references

1 (a) J. P. Klinman, *Chem. Rev.*, 1996, **96**, 2541-2562; (b) E. I. Solomon, D. E. Heppner, E. M. Johnston, J. W. Ginsbach, J. Cirera, M. Qayyum, M. T. Kieber-Emmons, C. H. Kjaergaard, R. G. Hadt and L. Tian, *Chem. Rev.*, 2014, **114**, 3659-3853; (c) E. I. Solomon, U. M. Sundaram and T. E. Machonkin, *Chem. Rev.*, 1996, **96**, 2563-2606.

2 (a) M. Suzuki, *Acc. Chem. Res.*, 2007, **40**, 609-617; (b) L. Q. Hatcher and K. D. Karlin, in *Adv. Inorg. Chem.*, eds. R. van Eldik and J. Reedijk, Academic Press, 2006, vol. 58, pp. 131-184; (c) C. E. Elwell, N. L. Gagnon, B. D. Neisen, D. Dhar, A. D. Spaeth, G. M. Yee and W. B. Tolman, *Chem. Rev.*, 2017, **117**, 2059-2107; (d) E. A. Lewis and W. B. Tolman, *Chem. Rev.*, 2004, **104**, 1047-1076; (e) L. M. Mirica, X. Ottenwaelder and T. D. P. Stack, *Chem. Rev.*, 2004, **104**, 1013-1046; (f) D. A. Quist, D. E. Diaz, J. J. Liu and K.

D. Karlin, *J. Biol. Inorg. Chem.*, 2017, **22**, 253-288; (g) N. Kitajima and Y. Moro-oka, *Chem. Rev.*, 1994, **94**, 737-757.

3 R. R. Jacobson, Z. Tyeklar, A. Farooq, K. D. Karlin, S. Liu and J. Zubieta, *J. Am. Chem. Soc.*, 1988, **110**, 3690-3692.

4 A. S. Borovik, *Acc. Chem. Res.*, 2005, **38**, 54-61.

5 (a) T. Fujii, S. Yamaguchi, Y. Funahashi, T. Ozawa, T. Tosha, T. Kitagawa and H. Masuda, *Chem. Commun.*, 2006, 4428-4430; (b) T. Fujii, S. Yamaguchi, S. Hirota and H. Masuda, *Dalton Trans.*, 2008, 164-170; (c) S. Yamaguchi, A. Wada, Y. Funahashi, S. Nagatomo, T. Kitagawa, K. Jitsukawa and H. Masuda, *Eur. J. Inorg. Chem.*, 2003, **2003**, 4378-4386; (d) S. Kim, C. Saracini, M. A. Siegler, N. Drichko and K. D. Karlin, *Inorg. Chem.*, 2012, **51**, 12603-12605; (e) D. Maiti, J. S. Woertink, A. A. Narducci Sarjeant, E. I. Solomon and K. D. Karlin, *Inorg. Chem.*, 2008, **47**, 3787-3800; (f) A. Wada, Y. Honda, S. Yamaguchi, S. Nagatomo, T. Kitagawa, K. Jitsukawa and H. Masuda, *Inorg. Chem.*, 2004, **43**, 5725-5735; (g) R. L. Peterson, J. W. Ginsbach, R. E. Cowley, M. F. Qayyum, R. A. Himes, M. A. Siegler, C. D. Moore, B. Hedman, K. O. Hodgson, S. Fukuzumi, E. I. Solomon and K. D. Karlin, *J. Am. Chem. Soc.*, 2013, **135**, 16454-16467.

6 A. Wada, M. Harata, K. Hasegawa, K. Jitsukawa, H. Masuda, M. Mukai, T. Kitagawa and H. Einaga, *Angew. Chem. Int. Ed.*, 1998, **37**, 798-799.

7 S. Yamaguchi, S. Nagatomo, T. Kitagawa, Y. Funahashi, T. Ozawa, K. Jitsukawa and H. Masuda, *Inorg. Chem.*, 2003, **42**, 6968-6970.

8 C. M. Moore, D. A. Quist, J. W. Kampf and N. K. Szymczak, *Inorg. Chem.*, 2014, **53**, 3278-3280.

9 (a) C. M. Moore and N. K. Szymczak, *Chem. Commun.*, 2015, **51**, 5490-5492; (b) C. M. Moore and N. K. Szymczak, *Chem. Sci.*, 2015, **6**, 3373-3377.

10 (a) E. W. Dahl, T. Louis-Goff and N. K. Szymczak, *Chem. Commun.*, 2017, **53**, 2287-2289; (b) E. W. Dahl and N. K. Szymczak, *Angew. Chem. Int. Ed.*, 2016, **55**, 3101-3105.

11 Resonance Raman spectroscopy was also used to interrogate the O–O and Cu–O stretching frequencies in $\mathbf{2^{H}}$; however no ^{18}O active modes were defined.

12 Complex $\mathbf{2^{CF3}}$ precipitates from CH_2Cl_2 at -70°C over 30 sec. Therefore UV-Vis spectra of $\mathbf{2^{R}}$ were collected in a 1:1 CH_2Cl_2:acetone solution by first forming the complexes in pure CH_2Cl_2 followed by addition of cold acetone.

13 C. X. Zhang, S. Kaderli, M. Costas, E.-i. Kim, Y.-M. Neuhold, K. D. Karlin and A. D. Zuberbühler, *Inorg. Chem.*, 2003, **42**, 1807-1824.

14 (a) C.-l. Chuang, K. Lim, Q. Chen, J. Zubieta and J. W. Canary, *Inorg. Chem.*, 1995, **34**, 2562-2568; (b) M. Schatz, M. Becker, F. Thaler, F. Hampel, S. Schindler, R. R. Jacobson, Z. Tyeklár, N. N. Murthy, P. Ghosh, Q. Chen, J. Zubieta and K. D. Karlin, *Inorg. Chem.*, 2001, **40**, 2312-2322; (c) K. D. Karlin, N. Wei, B. Jung, S. Kaderli, P. Niklaus and A. D. Zuberbuehler, *J. Am. Chem. Soc.*, 1993, **115**, 9506-9514.

15 The chemical shift of the methylene protons is highly sensitive to the electronic environment. For instance, the methylene protons shift from +0.04 ppm in $\mathbf{1^{CF3}}$ to -0.04 ppm in $\mathbf{1^{OMe}}$ compared to $\mathbf{1^{H}}$. Voltammetry was uninformative (see ref 16).

16 No discernable redox events could be obtained for [Cu(tpa^{OPh})]BAr'. We propose that a fluxional ligand dissociation process (shown from VT NMR studies) is responsible for the observed poor voltammetry response on the timescale of the electrochemical measurements.

17 Lopez, N.; Graham, D. J.; McGuire, R.; Alliger, G. E.; Shao-Horn, Y.; Cummins, C. C.; Nocera, D. G. *Science* **2012**, *335*, 450.

18 Mukherjee, D.; Ellern, A.; Sadow, A. D. *J. Am. Chem. Soc.* **2012**, *134*, 13018.

19 C.-L. Chuang, O. dos Santos, X. Xu, J. W. Canary. *Inorg. Chem.* **1997**, *36*, 1967-1972.

20 H.-C. Liang, E. Kim, C. D. Incarvito, A. L. Rheingold, K. D. Karlin. *Inorg. Chem.* **2002**. *41*, 2209-2212.

21 L. Lochmann, J. Pospíšil, D. Lím, *Tetrahedron Lett.* **1966**, 257.

22 CrystalClear Expert 2.0 r12, Rigaku Americas and Rigaku Corporation (2011), Rigaku Americas, 9009, TX, USA 77381-5209, Rigaku Tokyo, 196-8666, Japan.

23 O. V. Dolomanov, L. J. Bourhis, R. J. Gildea, J. A. K. Howard and H. Puschmann. *J. Appl. Cryst.* **2009**, *42*, 339-341.

24 G. M Sheldrick, *Acta Cryst. A64***, 2008**, 112-122.

Chapter 5: Summary and Outlook

These chapters represent very different applications of a fundamental phenomenon. Hydrogen bonding interactions are ubiquitous in Nature but their use as a tool to direct metal complex structure and reactivity remain underexplored. As inorganic chemists develop complexes for new reactions, metalloenzymes provide a blueprint, optimized over thousands of years, for how to approach ligand design. The ligands prepared in this thesis were inspired by the secondary sphere hydrogen bonding interactions found in metalloenzymes but ultimately found use in a variety of applications that extended beyond the initial systems in which they were based.

In chapter 2, ruthenium complexes that incorporated sterically bulky mesitylamino groups in the secondary sphere were used as catalysts for transfer hydrogenation and dehydrogenative oxidation reactions. The introduction of sterically protected H-bond donors was shown to enhance catalyst activity and stability. In chapter 3, an unusual square planar copper(I) complex was stabilized by secondary H-bonding interactions. The strained geometric state allowed for fast electron transfer self-exchange rates between the structurally similar Cu(I) and Cu(II) states. In chapter 4, the stabilization of peroxo complexes of copper and zinc using secondary sphere H-bonds was described. Electronic perturbations of the pendent phenylamino groups allowed for spectroscopic and structural tuning of the peroxo complexes and zinc diazide complexes. In many cases the critical role of H-bonding interactions was underscored by the synthesis, or attempted synthesis, of analogous species containing sterically similar ligands that

lacked H-bond donor groups. This approach should be considered standard practice moving forward in the field as it helps decouple the steric and H-bond influence on reactivity.

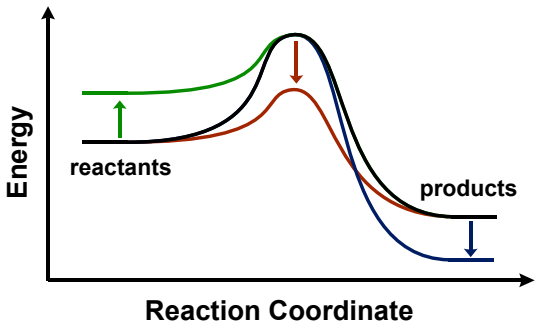

Figure 5-1: Three ways secondary sphere H-bonds can influence a reaction coordinate.

The chapters outline three distinct approaches to modifying the reaction coordinate of a given reaction. Chapter 2 demonstrates the ability of secondary H-bonds to lower the activation barrier for catalytic reactions (Figure 5-1, red trace). Chapter 3 demonstrates that enhanced reactivity can be obtained through the destabilization of a ground-state by H-bonding (Figure 5-1, green trace). Finally, chapter 4 demonstrates that H-bonds can be used to stabilize the products of a reaction (Figure 5-1, blue trace). Collectively, the data highlight the importance of considering secondary interactions in the design of new ligands. As we continue work on ligands based on phenylaminopyridines other research directions and potential limitations should be considered.

It is peculiar that the literature has been dominated by ligands bearing –NHCO^{t}Bu and –NHCH$_2$^{t}Bu functionality in the secondary sphere when phenylamino groups are easily installed and provide more steric and electronic tuning. The pivalamido groups are, however, less susceptible to –NH homolytic bond dissociation making them more suited for the stabilization of high oxidation state metal-oxos species. In contrast, the homolytic bond dissociation energy of

an –NHPh group could be tuned to either prevent or enhance H-atom abstraction. Ligands substituted with electron withdrawing –NH(*p*-CF_3-C_6H_5) groups would have a lower pKa but a higher bond dissociation free energy (BDFE) making them less susceptible to H-atom abstraction, while electron donating –NH(*p*-NMe_2-C_6H_5) groups have a higher pKa but a lower BDFE making them ideal ligands if H-atom abstraction is desired. This tunability may provide a useful framework to study proton-coupled electron transfer (PCET) reactions. While the bioinorganic chemistry of this thesis has been limited to copper and zinc, H-bonded complexes of cobalt and iron have been traditionally used to study reactive metal-oxo species. Ligands bearing 2-phenylaminopyridines could contribute to this area by tuning the –NHPh groups to allow PCET and probe the electronic requirements of a ligand's secondary sphere to stabilize metal-oxo intermediates.

Another potential area for expansion is the construction of 2-phenylaminopyridine-based ligands with new coordination numbers or binding modes. Metals that favor octahedral coordination like Fe(III) and Co(III) would be stabilized by a tetrapodal H-bonding ligands. In this pursuit, the tpa ligand could be modified with an additional 2-phenylaminopyridine arm allowing for pentadentate binding and octahedral coordination. The remaining open coordination site would contain four H-bond donors to stabilize reactive species. Alternatively, tetrahedral complexes with H-bonding interactions could be obtained by the synthesis of phenylamino derivatives of trispyridylmethane. In these ligand types, the directionality and length of the potential H-bonding interactions suffers due to the binding mode but the rarity of H-bonding tetrahedral complexes makes these ligands a worthwhile pursuit. Overall, the development of ligands with secondary H-bonding interactions will continue to provide access to new metal complexes with interesting reactivity.